Formation and characterization of novel nanostructured un-doped and Ga-doped ZnO transparent conducting thin films for photoelectrode

by

Jatani Ungula (M.Sc.)

A thesis submitted in accordance with the requirements for the degree

PHILOSOPHIAE DOCTOR

in the

Department of Physics

Faculty of Natural and Agricultural Sciences

at the

University of the Free State

Republic of South Africa

Promoter: Prof F. B. Dejene

Co-Promoter: Prof H. C. Swart

March 2018

Declaration

I, **Jatani Ungula**-student number **2012033243,** declare that the thesis hereby submitted by me for the Doctorate degree at the University of the Free State has not previously been presented for any degree and is not being currently considered for any other degree at any other university. I declare that this thesis contains my own research work except where specifically acknowledged. I, furthermore, cede copyright of the thesis in favour of the University of the Free State.

Signature:  Date: **20th March 2018**

Dedication

This thesis is dedicated to my:

Lovely family*- Ms. Sharon Kiprotich (wife) and Jayden J. Halakhe (son);*
dear parents*- Adhi Ungula (Aayo) and Ungula Halakhe (Aabbo) and*
dear brothers and sisters*- Wario, Abdub, Darmi and Tiya.*

Acknowledgements

Praise be to God forever for His everlasting love and compassion and for granting me the strength, determination and passion to pursue this course for the service of mankind and glory of His name. I am most humbled and obliged to give lots of appreciation to individuals and institutions that the Lord provided for the attainment of this noble goal.

My foremost gratitude goes to my supervisor Prof. F.B Dejene and co-supervisor Prof H. C. Swart. I am eternally grateful for their enormous support of different kinds and unlimited encouragement during the course of my study. I recall and treasure the discussions that we shared with regards to my project and general matters. I appreciate the constructive criticisms, valuable comments and suggestions which were indispensable for the completion of my project.

I am also thankful to all Physics department QwaQwa campus members of academic staff and my research colleagues (not in any order) Dr. K.G Tshabalala, Dr. L.F Koao, Mr. R.O Ocaya, Mr. S. J Motloung, Ms. Meiki Lebeko, Ms. S. Kiprotich, Ms M. A. Lephoto, Mr T. D. Malevu and many others for their continuous support during my period of study.

It is my pleasure to remember members of the Physics fraternity of Bloemfontein campus for their cordial welcome and hospitality, guidance and positive interactions during my frequent research visits to their Laboratory and facilities. Just to mention but a few; I appreciate enormous support from Prof K. Terblans, Prof Ted Kroon, Dr M. M. Duvenhage, Dr P. Mokoena, Ms. K. Cronje, Mr. H. Emad, Mr. A. Fourie, Mrs. L. Yolandie and Mr. Cronje Shaun.

My appreciation goes to Ms. Palesa, Mr. Tyson, Dr P. Mofokeng, Ms. De Clerk and Ms. T. Gumede of Chemistry Department QwaQwa campus for allowing me to use their SEM, FTIR and DTA/DSC systems and also for being good Samaritans and neighbours especially for their help with chemicals and apparatus on a number of occasions.

I gratefully acknowledge the financial support for my project from the South African Research Chair Initiative (SARChI – Grant 84415) bursary, the National Research Foundation (NRF) and the University of the Free State.

Finally, I would like to express my indebtedness to my family-beloved wife Sharon Kiprotich, our son Jayden J. Halakhe, parents, brothers and sisters for their love, encouragement and support.

Abstract

In the present work, Ga-doped ZnO (GZO) thin films and ZnO nanorods (ZNRs) were fabricated for possible use as a transparent conducting oxide (TCO) film and a semiconductor oxide (SC) material, respectively, for photoelectrode component of the dye-sensitized solar cells (DSSCs). The GZO nanoparticles (NPs) were synthesized using the reflux-precipitation method, while ZNRs were grown on glass substrates seeded with an optimized GZO layer by the chemical bath deposition (CBD) method. The material properties of the samples were studied using various techniques.

The X-ray diffraction patterns for all the GZO NPs and ZNRs exhibited a highly crystalline and hexagonal wurtzite structure of ZnO with no impurity phases. The values of the crystallite sizes range from 11 - 28 and 21 - 31 nm for the NPs and ZNRs samples, respectively. Peak shifts to lower diffraction angles from 47.45 - 47.35° with the increase in Ga/Zn solution pH was observed. A similar trend was observed also for other growth and deposition parameters studied. The studies on effects of annealing temperature and Ga-doping levels showed that the average lattice constants ‘a′ and ‘c′ were calculated as a = 3.263 and c = 5.208 Å, showing an increase in trend with the increase in Ga doping levels and annealing temperature. These values are in close range to the bulk ZnO lattice constants shown in the JCPDS card, No. 79-0205 (a = 3.264 and c = 5.219 Å). The XRD analysis revealed that the as-grown ZNRs were preferentially oriented along the c-axis in most cases with relative texture co-efficient values for (002) plane ranging from 0.309 - 0.418 and 0.37 - 0.56 with the increase in CBD growth concentration and growth time, respectively.

The scanning electron microscopy (SEM), images revealed that, at the lower growth pH, the micrographs showed agglomerated tiny GZO NPs that formed on big slabs of nanorods, but fine and enlarged particles on nano-spherical bases formed at the higher pH values. The tiny hexagonal particles for un-annealed samples turned into bigger rods with increasing annealing temperatures. Similarly, the SEM micrographs and atomic force microscopy images of the ZNRs showed an increase in lengths and particle sizes as the growth concentration and time increased. It is important to note that, more regular and orderly nanorods with enhanced morphology and uniformity could be observed with the increase of the growth concentration to 0.05 M and time to 90 min.

The PL results of the samples showed sharp and dominant UV-emission peaks which varied in position between 380 and 390 nm; and relatively smaller and broader deep level peak intensities (centred around 550 nm). The highest intensities of the UV-emission peaks

were observed for GZO NPs prepared at 2 mol% Ga doping, annealing temperature of 300 ºC and 5 pH of growth solution, as well as ZNRs prepared at 0.05 M concentration and 90 min growth time. Interestingly, minor peaks located around 440 nm could also be seen in few samples. It was observed that the emission peaks of ZNRs and GZO NPs generally shifted towards higher wavelengths with the increase in the growth and deposition parameters.

The UV-Vis analysis also demonstrated that the optical properties of the GZO NPs and ZNRs improved with the increase in growth and deposition parameters, as shown by the blue shift of the absorption edge of the reflectance spectra. The band gap energies of the GZO NPs were tuned from around 3.15 to 3.31 eV with the increase in the pH to 5 and Ga doping levels to 2 mol%. However, the band gaps of ZNRs varied between 3.1 and 2.0 eV with the increase in growth concentration and deposition time.

It was observed that the GZO NPs' sample prepared at 2 mol% Ga doping, 5 pH growth medium and annealed at 300 ºC presented an optimum crystallinity, minimum lattice stress, enhanced luminescence intensity and good optical properties and as such, was deposited on glass substrates to form the seed layer to produce GZO TCO film upon which ZNRs were grown. On the other hand, the sample that was deposited at the CBD growth concentration of 0.05 M and 90 min time presented good crystallization, good optical and luminescence properties with homogenous and well-aligned ZNRs. This could be used as a possible photoanode component of the dye-sensitized solar cell.

Key words

GZO NPs; dopant concentrations; luminescence properties; optical properties; temperature; transparent conducting oxide (TCO); pH; Ga and Al co-doped zinc oxide nanoparticles; semiconductor, GZO thin films, ZnO nanorods, DSSCs; crystal structure, CBD.

Acronyms

- **1D** - One dimensional
- **AFM** - Atomic force microscope
- **CBD** - Chemical bath deposition
- **CBM** - Conduction band minimum
- **DI water** - De-ionized water
- **DLE** - Deep level emission
- **EDS/EDX** - Energy dispersive x-ray spectroscopy
- **EL** - Electroluminescence
- **FWHM** - Full width at half maximum Electroluminescence
- **HCP** - Hexagonal close packed
- **NBE** - Near band edge emission
- **PL** - Photoluminescence
- **PLD** - Pulsed laser deposition
- **PVP** - Polyvinylpyrrolidone
- **RT** - Room temperature
- **UV** - Ultraviolet
- **VBM** - Valance band maximum
- **XRD** - X-ray diffraction
- **ZnO** - Zinc oxide

Table of Contents

List of Figures and Tables

Chapter 1

Introduction

1.1 Solar cells

In the words of Michael Grätzel, "Perhaps the largest challenge for our global society is to find ways to replace the slowly but inevitably vanishing fossil fuel supplies by renewable resources and, at the same time, avoid negative effects from the current energy system on climate, environment and health."

The worldwide demand for energy has been increasing constantly to support the economic growth. Actually, it is projected that the world energy consumption will increase by about 28% between 2015 and 2040 [1]. Yet, the energy economy is still highly dependent on the limited fossil fuels resources in the form of - oil, natural gases and coal - which cover more than 85% of the total energy production [2]. There is a serious cause for worry because the energy reserves of fossil fuels throughout the whole world are facing rapid resource depletion and soon the world demand for it will exceed annual production and shortages of fossil fuels may cause international economic and political crises and conflicts. Furthermore, overdependence on fossil fuels is leaving us vulnerable to air pollutants such as CO, CO_2 and SO_2 and related health risks and global warming due to the increased green-house gas. This unabated demand for energy, combined with the depletion of fossil resources, global warming and climate change, call for an urgent need for realization of new and sustainable technologies that power the world efficiently and cleanly. The answer to these energy and environmental challenges lies on the rapid development of alternative sources of energy that will lead to the reduction of fossil fuel consumption and decrease in the emission of harmful substances.

Special attention is paid currently to the development of new technologies allowing for the utilization of so-called renewable energy sources which are derived from natural processes that are replenished constantly [3] such as sunlight, wind, flowing water, the earth's internal heat, biomass such as energy crops, agricultural and industrial waste, and

municipal waste. Tapping into these energy sources is desirable both from an ecological and an economic point of view and as anticipated, the renewable share of worldwide electricity generation is expected to grow from 24% in 2016 to 30% in 2022 according to the IEA (International Energy Agency) [3]. In fact, IEA projects, the growth in renewable generation will be twice as large as that of gas and coal combined by 2022. The optimization of the existing processes for power generation and the development of new technologies are, therefore, a matter of scientific, technological, economic and public concern.

Between all the available technologies producing renewable energy, photovoltaic energy is a hot topic in current research. The main reason is because the Earth receives 1.2×10^{17} W insolation or 3×10^{24} Joule of energy per year from the Sun and this means covering only 0.13% of the Earth's surface with solar panels with an efficiency of 10% would satisfy our present needs [4]. Besides, photovoltaic cells have also other competitive advantages such as little need for maintenance, off-grid operation and silence, which are ideal for usage in remote sites or mobile applications. Simply put, the photovoltaics are efficient, inexpensive and environmentally friendly. Consequently, it is understandable that the electricity generated from photovoltaics has been increasing exponentially over the past two decades as shown in Fig. 1.1.

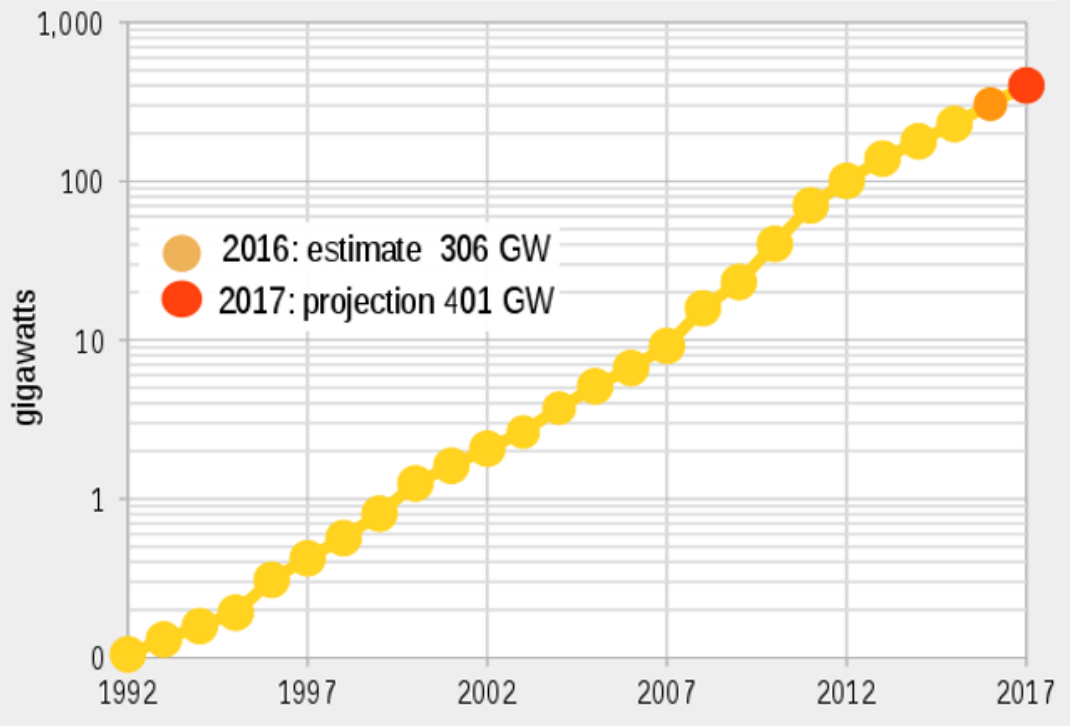

Figure 1.1: Exponential Growth of Global Solar PV (in GW) [5].

The solar cells as one type of photovoltaic devices have drawn great interest as an indigenous, clean, sustainable energy with huge and inexhaustible resources. The solar energy at the surface of the earth is mainly distributed at visible and near-infrared (near-IR) wavelengths, with a small proportion of energy falling in the Ultra-Violet (UV) spectrum [6]. Since the creation of first practical solar cell in Bell Laboratory in 1954 [7], different types of solar cells have been developed and established with the main objective of lowering the price of the solar cells and increasing their lifetime. Therefore, all the approaches for the development of solar cells has been based mainly on the use of abundant and low cost materials, simplification of the preparation processes, minimization of the required materials and the maximization of the cell efficiencies [8].

1.2 Materials for 1st, 2nd and 3rd generation solar cells

The history of solar cells can be classified into three generations. The 1st generation solar cells have very high manufacturing and installation costs, which commonly involve mono-crystalline materials such as mono-crystalline Si solar cell and mono-crystalline GaAs solar cell. Silicone supply can be easily available since it is the second most abundant raw material that can be found on earth [9] and manufactured mono-crystalline Si solar cells achieved up to 17% of efficiency. However, due to its indirect band gap, a thick layer (few hundred micrometres of material) is required for efficient light absorption. This, together with costly purification and crystallization processes of silicon, make the production of silicon cells very expensive. On the other hand, possessing high efficiency, high heat resistance and with a light weight, GaAs solar cells are usually used for space applications [10]. However, the expensive single-crystal GaAs substrate makes it difficult for terrestrial use [11]. In addition, the GaAs compound can potentially threaten humanity's health due to toxic fabrication process [12]. Binary II-IV and II-V semiconductors such as GaAlAs, GaInAsP, InAs, InSb and InP also fall into this group. Two different approaches have been considered to face the problems associated with first generation photovoltaics: (a) to work on reducing the manufacturing costs and (b) to increase the energy conversion efficiency beyond the Shockley-Queisser limits [13]. The photovoltaic cells belonging to the 2nd generation generally use polycrystalline semiconductor materials and are known as thin film solar cells because here, the basic structure of the device is no more the p-n junction, but a multilayer structure in which carriers are exchanged. The most efficient examples are solar cells made up of cadmium telluride (CdTe) and copper indium gallium diselenide (CIGS).

They employ the use of a simpler preparation process that reduces the cost, nonetheless, their efficiencies are typically lower than that of 1st generation cells. The main issues associated with this kind of technology are the use of toxic materials as, e.g., cadmium and rare elements as telluride and indium. The 1st and 2nd generation cells, presently, constitute about 80% of the solar cell market in 2017. Currently, the goal of photovoltaic technology is geared toward the making of 3rd generation solar cells that offer both high efficiencies and incur low production costs [14]. Generally, the term 3rd generation is used to describe systems which do not fall into the first or second generation and/or which try to circumvent the 31% Shockley-Queisser limit and they include various technologies. The most active research fields comprise organic heterojunctions [15] extremely thin absorber (ETA) cells [16, 17], hybrid solar cells [18] and dye-sensitized solar cells [19].

1.3 The Dye-sensitized solar cells

Among the 3rd generation cells, the DSSCs based on nanostructured wide band gap semiconductor films photosensitized with a dye serve as one of the best approaches to provide alternative to the conventional p-n junction based solar cells or rather the first and second generation cells. This is due to their fascinating features such as low fabrication cost, relatively high efficiency, transparency and the possibility of being fabricated in different colors [20]. The DSSCs represent a cheap and clean technology that harnesses solar energy efficiently and have been intensively studied since their birth in 1991, when M. Grätzel and B. O'Regan reported on a device made of sensitized nanoporous TiO_2 with a conversion efficiency of 11% in diffuse daylight [19]. This discovery opened a new field of scientific research and since then DSSCs have been intensively studied and are currently undergoing rapid development for practical use with the aim of improving their efficiency and stability. However, the solution-based DSSC device performance has made little improvement since then. At the time of writing, the breakthrough came in 2011 with the report [21] of a zinc porphyrin-based dye which broke the Grätzel world record, affording 12.3% under 1 sun illumination, when coupled with a cobalt-based electrolyte in a Grätzel cell. How to further decrease the production cost and meanwhile enhance device performance becomes the bottleneck for large-scale application and commercialization of DSSCs.

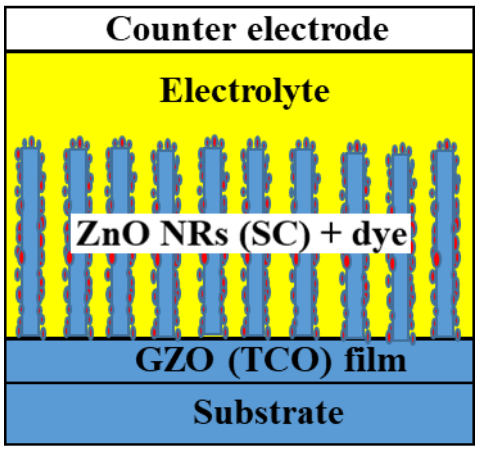

Figure 1.2: Device structure of the nanostructured ZnO based Dye-sensitized Solar Cell.

A typical DSSC consists of a dye-sensitized photoelectrode, electrolyte, and a counter electrode as shown in Fig. 1.2. The photoelectrode is composed of a semiconductor oxide (SC) film and a transparent conducting oxide (TCO) film. The TCO serves as an optical window, which determines the amount of light entering the device, and as the electrode, which extracts photocurrent [22]. The electrolyte is usually composed of a sensitizer (dye) and a redox mediator such as I^{3-}/I^{-1}. The dye molecules are responsible for harvesting the light. For instance, Grätzel and O´Regan found a successful combination of a nanostructured semiconductor electrode with an efficient and stable dye. In their configuration, the main components are a layer of titanium dioxide nanoparticles sensitized by a ruthenium-complex dye with the I^-/I^{3-} redox couple in an organic solvent, which acts as the redox mediator and a platinized FTO glass as a counter electrode.

The working of the DSSCs typically involves few steps. Whereby, light is absorbed by a dye attached to the surface of a mesoporous large band gap semiconductor and the solar energy transformed into electricity via the photoinduced injection of an electron from the excited dye into the conduction band of the semiconductor. The electrons move through the semiconductor to a current collector and external circuit. A redox mediator in the pores ensures that oxidized dye species are continuously regenerated and that the process is cyclic [4]. Since these components interact directly with one another in an operating DSSC, the researches on each of the component will be useful to develop the performance of the DSSCs. In this regard, the selection of semiconductor oxide and the corresponding TCO for the photoelectrode component of DSSCs is critical to achieving efficient light harvesting, charge separation and extraction. As such, major efforts have been placed on the development of new photoelectrode material.

1.3.1 Transparent Conducting Oxide and Semiconductor oxide films

The conventional TCO materials used in DSSCs include the Indium-doped tin oxide (ITO), fluorinated tin oxide (FTO) and the ZnO-based TCOs. The ITO and FTO are the most widely used TCO materials [23, 24]. However, the scarcity and high cost of indium and toxicity of tin oxide have limited their large-scale use in these devices. On the other hand, ZnO-based TCO material has stimulated growing research interest in recent years [25, 26] due to its multi-functionalities and easy synthesis of various low dimensional structures. One-dimensional (1D) ZnO nanostructures, such as rods, wires, belts and tubes, have attracted much attention due to their unique physical, electrical and optical properties [27]. Moreover, the crystalline quality of ZnO oxide films is also reported to have a significant impact on the charge transport while n-type semiconductor ZnO nanorods provide a large surface area for dye anchoring in conjunction with direct conduction pathways for charge transport.

To this end, Ga-doped ZnO (GZO) is one of the most interesting ZnO based TCO film in focus within the research community due to a number of reasons. GZO satisfies two fundamental and most important features of the transparent conducting substrates for use as TCO which are its high transmittance which allows maximum natural sunlight to pass through and eventually reach the active material and low electrical resistivity to facilitate electron transfer and reduce internal energy loss. Furthermore, while the electrical and optical properties of GZO are comparable to those of ITO, the performance of DSSCs with GZO as the TCO were also found to be superior to DSSCs based on FTO TCO, under the same growing condition. Being a member of Group III elements, Ga is used as a cation dopant to improve the electrical properties of ZnO such as charge carries concentrations and charge mobility. When Ga dopant occupies the position of Zn^{2+} or in the position of ZnO lattice, electronegativity and ionic radius change. Between the ZnO: Ga and ZnO: Al, although the cost is in favour of ZnO: Al, ZnO: Ga is more stable when exposed to moisture and oxidation. The bond length of Ga-O (1.92 Å) is very close to the value of Zn-O (1.97 Å), which permits larger doping range as compared to Al-O (1.7 Å). Importantly, the GZO TCO is sought after for its abundant source material, low cost and non-toxicity.

To increase the surface area with adsorbed dye molecules, the DSSCs usually incorporate TiO_2 or ZnO semiconductor component as the photosensitized anode, due to their wide-band gap, porous structured film, high stability against photo-corrosion on optical excitation

in the band gap and novel optical and electronic properties [2]. TiO_2 had registered a remarkable performance in the field of DSSCs. However, attempts made to increase conversion efficiency and improve the performances of DSSCs of TiO_2-based DSSCs are limited by electron recombination during the charge transport process, which is mainly due to the lack of a depletion layer on the TiO_2 nanocrystallite surface [28]. TiO_2 has a lower electron mobility than ZnO (115–155 $cm^2\ V^{-1}\ s^{-1}$). Slow electron mobility results in a high recombination loss and slow electron transport in TiO_2. Accordingly, ZnO semiconductor oxide is regarded as a promising alternative to TiO_2 for photoanode application in DSSCs. In addition to a wide band gap (energy gap 3.37 eV), with a conduction band edge positioned approximately at the same level as for TiO_2, ZnO allows the visible light to pass through in order to harvest the solar energy in the broad spectrum. ZnO possesses physical properties similar to those of TiO_2. Moreover, ZnO presents a cheaper fabrication process owing to its ability to grow easily in a wide variety of nanostructures and its stability in the electrolyte used.

1.4 Basis and scope of this work

1.4.1 Motivation

The main motivation of this research is that; ZnO nanostructures having unique chemical and physical properties offer the possibility and flexibility of controlling various growth and post growth parameters for the synthesis of GZO NPs and ZnO NRs used in fabrication of the photoelectrode component of DSSCs. Moreover, since the components of the DSSCs interact directly with one another during operation of the panel, the researches on each of the component will be useful for the development and optimization of the performance of the DSSCs. The research is also spirited by the fact that, the combination of the optimized ZNRs semiconductor and GZO films would provide a promising photoelectrode for the DSSCs application where the improvement of conductivity and the decrease of resistivity is the main issue. The reflux precipitation and the CBD techniques used in this study allow synthesis at low temperatures, use simple equipment and they are low-cost methods unlike some which use complex processes to obtain the samples or demand very high power synthesis conditions in temperature or pressure that makes sizing up of the product difficult.

1.4.2 Definition of research problem

ZnO nanostructures are attractive entities to be used for photoelectrode component of DSSCs applications because of their versatile properties. However, there are still significant challenges that have to be overcome in order to produce efficient ZnO based photoelectrode for the DSSCs. It is widely acknowledged that the morphology of ZnO nanostructures is highly sensitive to the growth environment (i.e. temperature, pressure, substrates, precursors and their concentrations, the VI/II ratio or pH, etc.). This sensitivity makes it very difficult to control the growth process for the reproducible formation of the desired morphology over large areas. Another main challenge is controlling native defects and possible compensation processes. Again, some of the basic properties of ZnO are not well understood [29, 30] and are still debatable owing to the different intrinsic defects such as oxygen interstitials (O_i), zinc interstitials (Zn_i), oxygen vacancies (V_o), zinc vacancies (V_{Zn}). Furthermore, it is understood that the defects in ZnO are dependent on the growth techniques. Interestingly, the coexistence of electrical conductivity and optical transparency in ZnO materials also depend on various factors such as the nature, number and atomic arrangements of metal cations in crystalline or amorphous ZnO structures; on the resident morphology and on the presence of intrinsic or intentionally introduced defects. Consequently, the thesis seeks to address how to explore and control the growth process of un-doped and Ga-doped ZnO nanostructures for the reproducible formation of desired properties amid highly sensitive growth environment and to control native defects and advance possible compensation process.

As far as the fabrication and optimization of a nanostructured ZnO-based photoelectrode component of DSSCs are concerned, one of the main challenges is the lattice mismatch between the TCO film and the ZnO semiconductor layer. Additionally, despite the efforts devoted to the development of ordered nanostructures, their efficiencies lie well below the ones obtained with mesoporous nanoparticle electrodes. This fact is usually attributed to low light harvesting properties due to the lower surface area of one-dimensional nanostructures [3]. The reports in the literature [3,25,31] point out that recombination rather than low surface area is the main limitation of these one-dimensional nanowires. Fortunately, a significant blocking of the recombination in the solar cell is reported to be achieved by use of well-aligned ZnO nanorods semiconductor along with a suitable TCO film. The ZnO nanorods based DSSCs can provide a direct pathway along the 1D crystalline nanostructure to reduce the possibility of charge recombination during interparticle percolation [1].

Moreover, since the GZO film substrate and ZnO nanorods have good lattice match there is no risk of stress that may be induced in the bottom of the ZnO nanorods and no defects generated in the initial ZnO layer, which may result in the green band emission. Therefore, it is expected that the homogeneous GZO TCO / ZnO SC interface may largely enhance the electron transfer property, and hence improve the cell performance.

1.4.3 Objectives of the research

The specific objectives of this research were:

1. To synthesize the seeding with fairly good material properties to make TCO thin films using a novel reflux precipitation method. The following investigations were carried out:
    - the study of the effects of un-doped, Ga/Al-doped and co-doped ZnO NPs,
    - optimization of the Ga doping levels in GZO NPs,
    - the effect of annealing temperatures and the nature of Ga/Zn sol. pH on the structural, morphological, luminescence and optical properties of the GZO NPs prepared
2. To achieve controllable growth of ZnO nanorods on Ga-doped ZnO seed layer thin films using the CBD method. The investigations include the study on:
    - the influence of precursor concentration and the molar ratios of the reactants,
    - the effect of growth time on the structural, morphological, luminescence and optical properties of ZnO nanorods.
3. To investigate the structural, morphological and elemental properties of the GZO NPs and ZnO NRs using the x-ray diffraction (XRD), scanning electron microscopy (SEM), energy dispersive x-ray spectroscopy (EDS) and the atomic force microscopy (AFM) techniques.
4. To study the optical and luminescence properties of GZO NPs and ZnO NRs using the photoluminescence spectroscopy (PL), catholuminescence spectroscopy (CL) and UV-Vis spectrophotometer.

1.4.4 Thesis Layout

The thesis consists of ten chapters.

The 1st Chapter begins with the introduction that is comprised of the summary of the research background, statement of the problem and aims of the study. Chapter 2 provides literature review; the underlying theories and overview of ZnO material properties. The

different applications of ZnO are also briefly discussed in this chapter. Chapter 3 gives a brief description of the experimental equipment, environmental and/or atmospheric requirements, techniques used to design, synthesize and characterize un-doped and Ga-doped ZnO nanoparticles and ZnO nanorods thin films. A summary of different characterization techniques along with the description of their operation is presented in this chapter.

Chapters 4-9 provide the experimental outcome of this study. In Chapter 4, the study on band gap engineering, enhanced morphology and photoluminescence of Ga and/or Al-doped ZnO by reflux precipitation method is reported. In Chapter 5, the effects of different Ga doping concentration on structural and optical properties of Ga–doped ZnO nanoparticles by precipitation reflux method are discussed. While in Chapter 6, the effect of annealing on the structural, morphological and optical properties of Ga-doped ZnO nanoparticles by reflux precipitation method is presented. Similarly, Chapter 7 reports on the effect of pH on the structural, optical and morphological properties of Ga-doped ZnO nanoparticles by reflux precipitation method. Chapter 8 presents the effects of precursor concentration on structural and optical properties of ZnO nanorods grown on GZO seeded thin film layer from aqueous solution. In Chapter 9, the effects of deposition growth time on structural and optical properties of ZnO nanorods grown on GZO seeded thin film layer from aqueous solution is discussed in detail.

Finally, Chapter 10 gives a brief summary of the obtained results and presents suggestions for the future work. The lists of the publications and the presentations at conferences are also outlined in this chapter.

References

[1] U.S. Energy Information Administration https://www.eia.gov/ieo [accessed online on 29/12/2017]

[2] http://port.polite.it [Accessed online on 17/07/2016 from the permalink]

[3] http://www.renewableenergyworld.com [Accessed online on 17/07/2017]

[4] M. Grätzel, Nature 414, (2001) 338-344.

[5] https://en.wikipedia.org/wiki/Growth_of_photovoltaics [Accessed online 20/12/2017].

[6] R. E. Bird, C. Riordan, Journal of climate and applied meteorology 25, (1986) 87-97.

[7] D. M. Chapin, C. S. Fuller, G. L. Pearson, G. L. Journal of Applied Physics *25*(5), (1954) 676-677.

[8] http://www.nrel.gov/ncpv/ [Accessed on 13/07/2016].

[9] http://www.epia.org/news/publications/global-market-outlook-for-photovoltaics-2013-2017/ [Accessed on 02/07/2016].

[10] P. A. Iles, Solar Energy Materials and Solar Cells 68(1), (2001) 1-13.

[11] Fong, Chun Hui, Study of the Tandem Solar Cell. Diss. UTAR, 2011.

[12] M. Omura, A. Tanaka, M. Hirata, M. Zhao, Y. Makita, N. Inoue, N. Ishinishi, Fundamental and Applied Toxicology 32(1), (1996) 72-78.

[13] K. Lobato, Charge Transport and Recombination in Dye-Sensitized Nanocrystalline Solar Cells, University of Bath 2007.

[14] N. Asim, K. Sopian, S. Ahmadi, K. Saeedfar, M. A. Alghoul, O. Saadatian, S. H. Zaidi, Renewable and Sustainable Energy Reviews 16(8), (2012) 5834-5847.

[15] T. L. Benanti, D. Venkataraman, Photosynthesis research 87(1), (2006) 73-81.

[16] A. Belaidi, T. Dittrich, D. Kieven, J. Tornow, K. Schwarzburg, M. Lux- Steiner, Physica status solidi (RRL)-Rapid Research Letters *2*(4), (2008) 172-174.

[17] Y. Itzhaik, O. Niitsoo, M. Page, G. Hodes, Journal of Physical Chemistry C *113*(11), (2009) 4254-4256.

[18] M. Lira-Cantu, F. C. Krebs, Solar energy materials and solar cells 90(14), (2006) 2076-2086.

[19] B. O'regan, M. Grätzel, Nature *353*(6346), (1991) 737-740.

[20] http://kutarr.lib.kochi-tech.ac.jp [Accessed online on 10/05/2016].

[21] A. Yella, H. W. Lee, H. N. Tsao, C. Yi, A. K. Chandiran, M. K. Nazeeruddin, M. Grätzel, Science 334(6056), (2011) 629-634.

[22] http://search.proquest.com [Accessed on 20/12/2017].

[23] T. Minami, Semiconductor Science and Technology 20(4), (2005) S35.

[24] J. W. Bae, S. W. Lee, G. Y. Yeom, Electrochem. Soc. 154, (2007) 34.

[25] Z. L. Wang, Journal of Physics: Condensed Matter 16(25), (2004) R829.

[26] W. I. Park, G. C. Yi, M. Kim, S. J. Pennycook, Advanced Materials 14(24), (2002) 1841-1843.

[27] S. P. Anthony, J. I. Lee, J. K. Kim, Applied Physics Letters 90(10), (2007) 103107.

[28] M. K. Wu, T. Ling, Y. Xie, X. G. Huang, X. W. Du, Semiconductor Science and Technology 26(10), (2011) 105001.

[29] M. D. McCluskey, S. J. Jokela, Journal of Applied Physics 106(7), (2009) 10.

[30] L. Schmidt-Mende, J. L. MacManus-Driscoll, Materials today 10(5), (2007) 40-48.

[31] H. Chen, A. Du Pasquier, G. Saraf, J. Zhong, Y. Lu, Semiconductor Science and Technology 23(4), (2008) 045004.

Chapter 2

Overview of ZnO material properties

2.1 Introduction

ZnO nanostructures have become a focus of research activities, in the recent times, because of their broad application related to their semiconducting, optical and piezoelectric properties. The main impetus of research on ZnO as a semiconductor material is the potential use of its wide direct band gap (3.37 eV), UV emission and a large exciton binding energy (60 meV) that allows sufficient excitonic emission within the UV range at 298K [1]. A large band gap means the material will not absorb photons with less energy than the band gap and leads to transparency for wavelength > ~370 nm, which makes ZnO one of the most important materials for transparent electrodes as an alternative to ITO. Moreover, as explained in the previous chapter, ZnO TCO materials are cheaper than their ITO counterparts because of the scarcity and high cost of indium and toxicity of tin oxide that limit the large-scale use of ITO in semiconductor devices. Due to its wide band gap, ZnO has the ability to be effective during processes at high temperature and power, and also with operations applying large electric fields [2]. Other desirable properties of ZnO include its visible light transparency, transparent conductivity and piezoelectricity, biocompatibility, structure and property controllability, and simplicity of synthesis process [3, 4]. ZnO material has, therefore, been under investigation for fabrication of nanodevices such as light emitting device arrays [5] electrochemical sensors/transducers [6], ultra-violet (UV) detectors [7], field-effect transistors [8], p-n junction diodes [9], Schottky diodes [10], dye-sensitized solar cells [11], biomedical sciences [12, 13], solar cell electrodes [14], spintronics [15] and as templates used to grow other nanostructures [16]. Besides, the non-toxicity, chemically stability and biocompatibility of ZnO make it useful for cosmetics, ointment and even for the food additive. Clearly, novel devices with improved performance, repeatability, and durability can be engineered by controlling ZnO nanostructures shape, their distribution and their material properties. The literature material on ZnO discussed concisely in this section are: luminescence phenomenon in ZnO and optical properties;

intrinsic (native) point defects in ZnO; crystal structure and lattice parameters of ZnO; the electronic band structure of ZnO; physical and mechanical properties of ZnO and the applications of ZnO nanostructures

2.2 Luminescence phenomenon in ZnO and optical properties

Light emission through any process other than blackbody radiation is called luminescence and requires external excitation as it is a non-equilibrium process. The luminescence properties of ZnO have been extensively studied at below and at room temperature owing to its wide band gap, large exciton binding energy and efficient radiative recombination [10]. Based on the excitation source, luminescence techniques such as photoluminescence (PL), electroluminescence (EL) and cathodoluminescence (CL) have been utilized to investigate the optical and luminescence properties of ZnO in different forms (bulk, nanostructures, and thin films).

PL is a powerful tool to study point defects in wide-band gap semiconductors. Most of the experimental results on point defects in ZnO have been obtained from the analysis of mainly the PL data [17]. The optical properties of ZnO contain a lot of information, such as optical absorption, transmission, reflection, Photoluminescence and so on. Fig. 2.1(a) shows a simplified band structure of a typical semiconductor near the centre of the first Brillouin zone, where a material with band gap energy Eg is irradiated by a laser with energy above the band gap ($h\nu$>Eg), resulting in the excitation of an electron into the conduction band (arrow 1) and leaving a hole behind in the valence band. An electron-hole (e-h) pair, usually called a free exciton (FX), is generated. Its energy is slightly smaller than the bang gap energy. The electrons and holes thermalize to the lowest energy state of their respective bands via phonon emission (shown by the red-wavy arrows) before recombining (arrow 2) across the fundamental band gap or the defect levels within the band gap and emitting photons of the corresponding energies. The defects levels in the band gap will result in various recombination of the carriers as shown in Fig. 2.1(b). A neutral donor (acceptor) will give rise to an attractive potential, a free exciton might be captured at the acceptor (donor) resulting to the formation of a bound exciton (DX). Whereas, an electron bound to a donor can recombine directly with a free hole from a valence band. This kind of recombination is called free-to-bound transition (AX). The recombination energy for such a transition corresponds to the band gap energy reduced with the binding energy of donor.

Another possibility is that a hole bound to an acceptor recombines with an electron bound to a donor in donor-acceptor pair (DAP) transition.

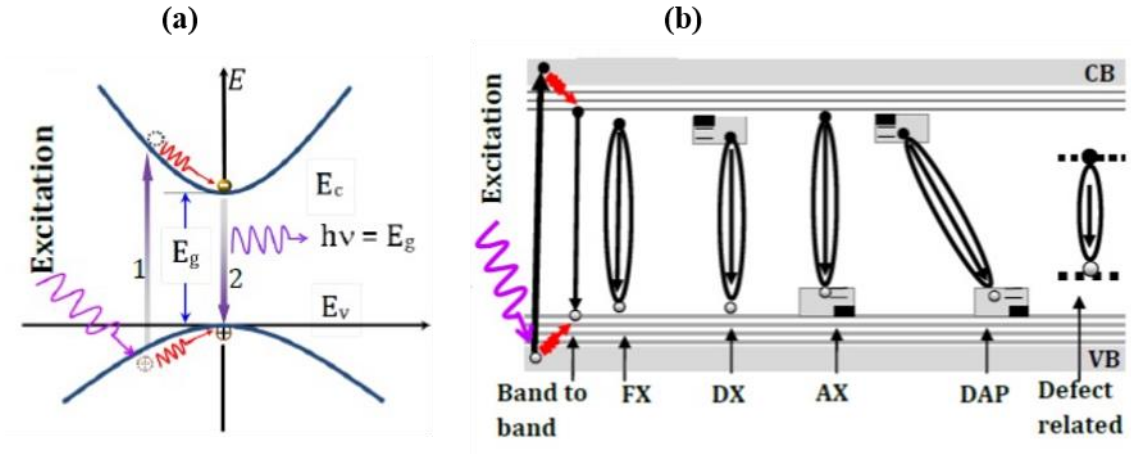

Figure 2.1: Band diagram illustration of the different processes that make up the photoluminescence spectra: (a) excitation, relaxation and recombination in *k*-space, and (b) possible mechanisms of e-h recombination [18].

Clearly, the luminescence phenomena involve different processes, starting from absorption and excitation, radiationless relaxation, and radiative emission of light [6]. When the electron–hole recombination results in photon emission, the process is called radiative recombination. However, a recombination process that does not produce photons is known as nonradiative recombination in which the energy is exchanged with the lattice as heat through phonon emissions within defect states in semiconductor or transferred its energy to other carriers.

Radiative transition

The common types of radiative emissions are fluorescence and phosphorescence. The fluorescence occurs when the excited electron returns to its ground state through the internal conversion process in the same singlet excited state (Fig. 2.2 the green downward arrows). The material stops emission immediately the excitation source has ceased. The estimated time for this process is of the order of 10^{-9} seconds [19]. However, the phosphorescence refers to the persistent radiation emission after the excitation source has ceased. This process takes place through the inter-system crossing process, where the returned electron experiences spin flip to create triplet state (unpaired) electrons. Spin-flip can occur during the absorption process. Consequently, the electron will spend a while until it flips back to its initial state, then it will return to the ground state. Due to the long lifetime of the triplet state, the molecules exhibit a high tolerance to photochemical reactions [20]. The schematic explanations of these processes are shown in a Jablonski diagram (Fig. 2.2)

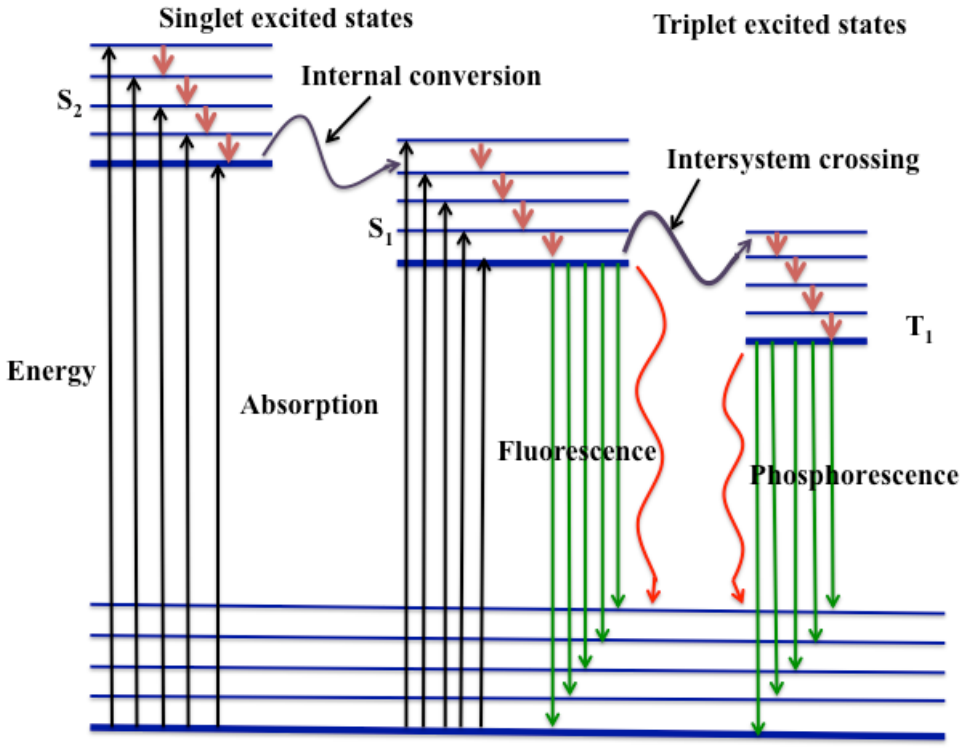

Figure 2.2: The Jablonski diagram demonstrates the possible mechanisms taking place in the luminescence phenomenon, upward-black arrows represent the absorption process, small-downward red arrows represent the vibrational relaxation (non-radiative transitions), green-downward arrows represent the emissive transition (fluorescence and phosphorescence) and the wiggly-red arrows represent internal and external conversion [21].

In ZnO, the room temperature PL spectrum usually contains two emission bands commonly known as the ultra-violet (UV) emission band and a broad visible emission or deep level emission (DLE) band. The UV emission is generally ascribed to the transition recombination of free excitons (F.E) in the near band-edge of ZnO with energy in the range of 3.375 ~3.378 eV, while the DLE is attributed to the presence of deep level defects in the crystal structures of ZnO. These defects can be introduced during the fabrication process or by applying other techniques like the post-annealing or ion implantation. The details of these defects, both intrinsic and extrinsic, in ZnO will be discussed in section 2.3.

Non-radiative transition

Non-radiative recombination occurs mainly through three physical mechanisms, but cannot be detected by PL. These are Auger recombination, recombination at defects in the bulk, and surface recombination. During Auger recombination, the e-h pair energy is transferred to a third free carrier that will move to a higher energy in the conduction band (in the case of an electron) or to a lower energy in the valence band (in the case of a hole). The e-h pair

thus recombines without photon emission. This is a three-body process because an electron and two holes or a hole and two electrons are involved. Since this is a three-particle interaction, it is normally only significant in non-equilibrium conditions when the carrier density is very high. For this reason, it only occurs under very high injection levels or for materials with high equilibrium carrier concentrations. Based on the wide band gap and non-degeneracy of the valence band it is suggested that Auger recombination is not important in ZnO. Recombination at defects in the bulk and surface regions of ZnO are expected to be the major non-radiative recombination processes.

2.3 Intrinsic (native) point defects in ZnO

As mentioned earlier, it is understood that the deep level emission or emission of whole visible range (400-750 nm) in ZnO has been majorly attributed to the presence of various native defects in the crystal structure. These native defects are also known as intrinsic defects [22]. The native point defects can be defined as the crystal lattice imperfections, where the constituent atoms are missing (vacancy), extra atoms occupying interstice sites (interstitial) or atoms occupying their alternative atom sites (antisite), they do not extend in the regular space in any dimension of the crystal. The defects can further, be classified as donor defects; which include oxygen vacancy (V_O) [23, 24], zinc interstitial (Zn_i) [25] and zinc anti-site (Zn_O), while acceptor defects are oxygen interstitial (O_i) [26], oxygen anti-site (O_{Zn}) and zinc vacancy (V_{Zn}) [27, 28].

The understanding of the intrinsic defects within the crystal structures is crucial because the defects play a major role in influencing the luminescence and optical properties of ZnO nanomaterials. Thus, it suffices to provide a brief discussion on these defects and their associated emissions in this section. Fig. 2.3 provides the details on the band diagram of the DLE in a diagrammatic form based on the full potential linear muffin-tin orbital method and other reported data.

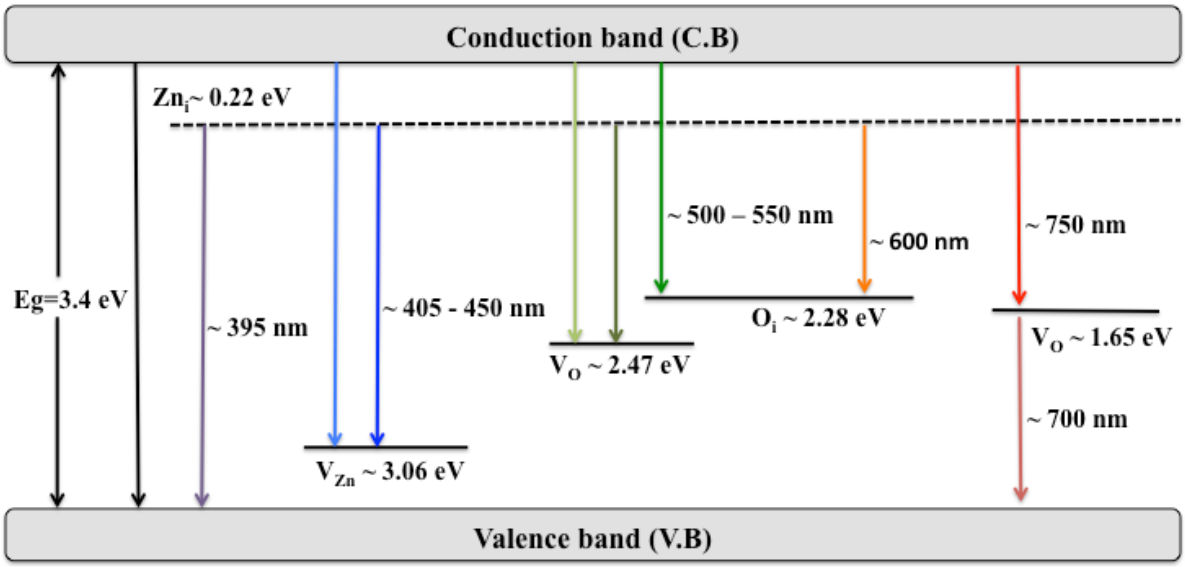

Figure 2.3: Schematic band diagram of ZnO deep level emissions (DLE), based on the full potential linear muffin-tin orbital method and other reported data [29, 30].

Oxygen vacancy (V_O)

This is the most prominent and controversial defect in ZnO. It occurs in three chemical states namely: neutral state (V_O^0), single ionized state (V_O^+), and double ionized state (V_O^{2+}). In the neutral state, the four Zn nearest neighbours contract toward each other by 12% relative to the ZnO in its equilibrium state. In the single ionized state, the four Zn atoms neighbours diverge about 3% and for the double ionized state, four Zn neighbours diverge about 23% relative to the equilibrium state of ZnO. V_O^{2+} in the neutral state is very stable in n-type. The single ionized oxygen vacancy has been proposed, by some researchers, to be the luminescence centre for the green emission around 500 nm that has been observed in ZnO [31]. On the other hand, the doubly ionized oxygen vacancies are reported to be responsible for the red emission from ZnO [32]. Density functional theory revealed that the oxygen vacancies are deep donors rather than being shallow donors. Therefore, they are not expected to play a role in the unintentional n-type ZnO. In case of zinc rich growth, Fig. 2.4, V_O has lower formation energy than the zinc interstitial and therefore the formation of oxygen vacancies is favourable in this environment.

Zinc vacancy (V_{Zn})

The zinc vacancy is formed as a result of the removal of a Zn atom from the ZnO lattice structure leaving four oxygen dangling bonds with six electrons. V_{Zn} were well studied and reported in the literature by some groups to be another source of the green emission positioned at 2.4-2.6 eV below the CB in ZnO [33, 34], besides the V_O defects. Moreover,

the recombination process between the zinc interstitial (Zn_i) energy level to V_{Zn} energy level is also reported to be responsible for the blue emission located at ~ 2.84 eV (436 nm). This occurrence can be well described by use of the full potential linear muffin-tin orbital method, which defines the position of the V_{Zn} level that is placed at ~ 3.06 eV below the CB, while the position of the Zn_i level is theoretically calculated at a position at ~ 0.22 eV below the CB [35]. The formation enthalpy of VZn decreases with increasing the Fermi level, and therefore it can occur in modest concentration in n-type ZnO.

Zinc interstitial (Zn_i)

Zni can be formed when an extra zinc atom occupies a tetrahedral or octahedral coordinates of the ZnO wurtzite structure. It is suggested to be stable and relaxes spontaneously in the octahedral site. Zn_i is a shallow donor with two electrons stabilizing in the +2 charge state (Zn^{2+}) above the conduction band maxima (CBM). Usually, the Zn_i defects are positioned at ~ 0.22 eV below the CB and they play important part for the visible emissions in ZnO due to the recombination process among Zn_i and different defects that exists in the deep levels like oxygen and zinc vacancies, oxygen interstitials which are the main source for the different colour emission such as blue, red and green emissions in ZnO [35]. Zn_i has a very high formation enthalpy, which decreases with the decrease in Fermi level towards the VBM (Fig. 2.4) and as such, occurs in low concentrations even at Zn-rich conditions.

Zinc and oxygen antisites

The zinc and oxygen antisites are native defects which are generated in the ZnO structure due to the occupying of wrong lattice position. These happen when an extra Zn atom fills the position of oxygen in the lattice or oxygen fills zinc position in the lattice resulting to the formation of Zn antisite (Zno) or oxygen antisite (O_{Zn}) respectively. The Zn_O is a double donor defect in n-type ZnO while O_{Zn} is a deep acceptor-type defect. They both have a high formation enthalpy, and therefore are not expected to form under near-equilibrium conditions even in a Zn-rich or O-rich environment [36]. The favourable conditions for these defects are non-equilibrium conditions and are mostly observed in electron-irradiated samples. They can be formed when they are subjected to an ion implantation or irradiation processing to merge them into ZnO.

Oxygen interstitial (O_i)

Oxygen interstitial (O_i) is a double acceptor defect which occurs when an oxygen atom wrongly occupies the tetrahedral site, octahedral site or a split interstitial position. They are

normally positioned at 2.28 eV below the CB and are responsible for orange-red emissions in ZnO [37]. The oxygen interstitials defects are also responsible for yellow emission as reported in some literature [38, 39]. Density functional theory calculation revealed that O_i in a tetrahedral site spontaneously relaxes into an interstitial split where more oxygen atoms share a lattice site; this is due to its instability in the tetrahedral site. In the octahedral site, the oxygen interstitial is electrically active and creates energy levels above the valence band at 0.7 and 1.52 eV that can accept two electrons. The formation enthalpy for the O_i in both cases (split and octahedral sites) is high, therefore, the favourable conditions to form is in O-rich environment. The formation enthalpies of the O_i(split) and O_i(oct) are 0.9 and 1.1 eV respectively.

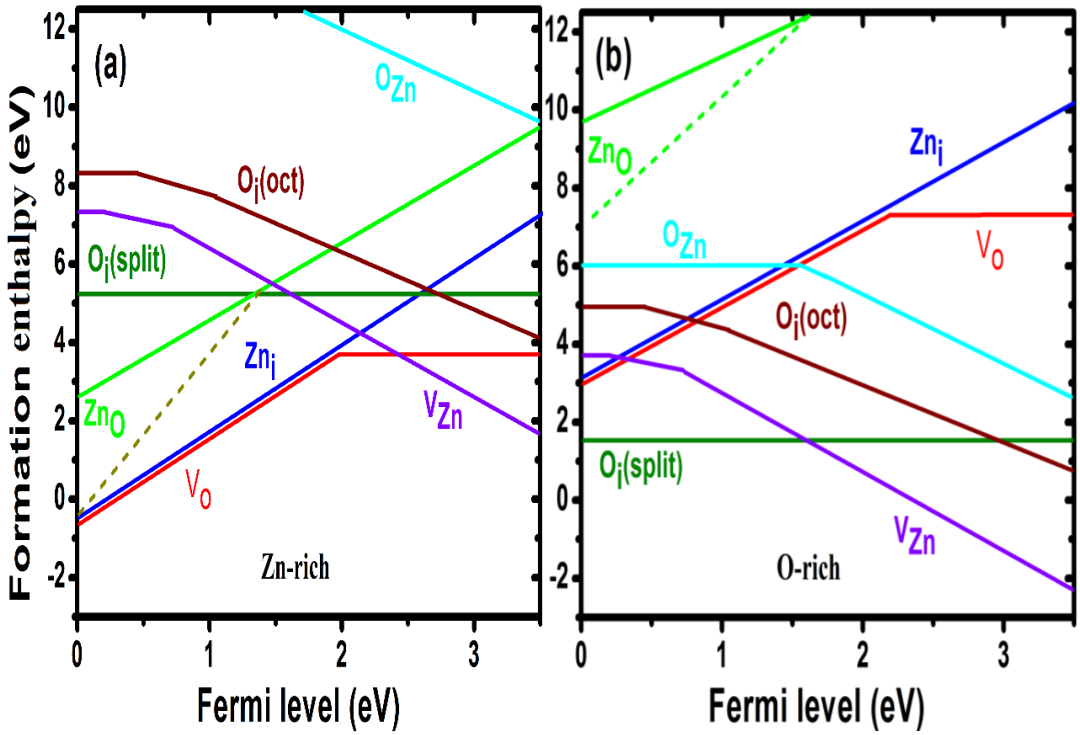

Figure 2.4: Formation enthalpies as a function of Fermi-level position for the ZnO native point defects in (a) Zn-rich and (b) O-rich conditions. The zero Fermi level corresponds to the valence-band maximum. The slope of these segments indicates the charge state. Kinks in the curves indicate transitions between different charge states [40].

Extrinsic defects

Whereas the intrinsic point defects comprise only the host atoms, the extrinsic point defects are generated when impurities/foreign atoms were incorporated in the structure of the semiconductor. The extrinsic defects are also suggested to be involved in deep level emissions. For instance, the emission due to the incorporation of copper impurities in ZnO is placed at 2.85 eV [41]. Similarly, after the doping of Li in ZnO thin film a yellow emission was observed at positioned 2.2 eV below the CB [42, 43] with the Li related defects. There

are some more extrinsic defects associated with Cu, Li, Fe, Mn and OH which are also responsible for luminescence from ZnO. It has been also reported that the defects having different energies can also produce the same colour emission such as the combinations of ZnO:Cu and ZnO:Co have different energies but they emit the same (green) colour [44] Additionally, there are reports that ZnO UV emissions positioned at 3.35 eV could be observed due to the excitons bound to the extrinsic defects like Li and Na accepters present in ZnO structures [45].

2.4 Crystal structure and lattice parameters of ZnO

ZnO has three types of crystal structures: hexagonal wurtzite, zinc-blende and rock salt, as shown in Fig. 2.5. The hexagonal wurtzite is the preferred structure and thermodynamically stable at room temperature and normal atmospheric pressure, therefore, is the most common amongst the structures [46]. In hexagonal wurtzite, each O^{2-} ion is surrounded by four Zn^{2+} ions at the corners of a tetrahedron, and vice versa. The tetrahedral coordination is typical of *sp*3 covalent bonding, but because of the difference in electronegativity between Zn and O (Oxygen = 3.44 and Zinc = 1.65), it also has a substantial ionic character [47]. Moreover, the tetrahedral coordination in ZnO is responsible for the non-central symmetric structure and consequently the piezoelectricity and pyroelectricity in ZnO material.

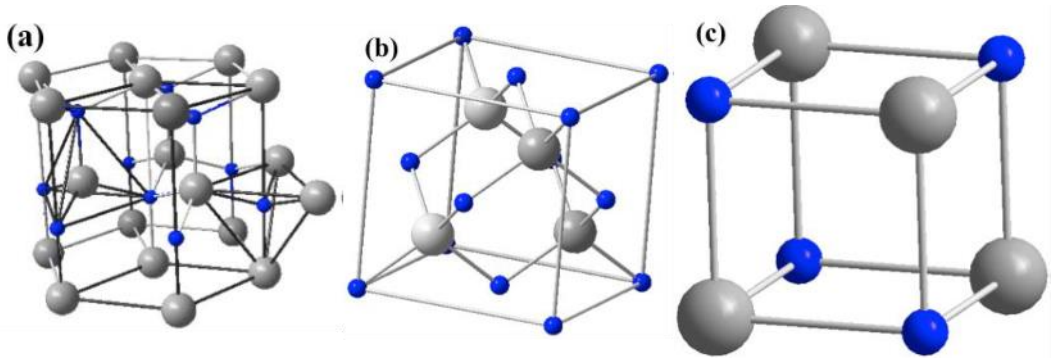

Figure 2.5: Crystal structure of ZnO (a) hexagonal wurtzite, (b) zinc-blende and (c) rock salt in stick and ball representation. The oxygen atoms are shown as blue spheres, zinc atoms as white spheres. Only one-unit cell is illustrated for clarity [Reprinted with permission from Ref. [49], Copyright 2006 by Elsevier Limited].

In zinc-blende structure, each Zn or O atom is surrounded by four nearest neighbours. Zinc blende ZnO has a lower carrier scattering and high doping efficiency due to its lower ionicity compared to the wurtzite structure. Nevertheless, the growth of ZnO in the zinc-blende structure is an experimental challenge because zinc-blende ZnO structure can be stabilized only by growth on cubic substrates. In the rock salt structures, each Zn or O atom

is surrounded by its alternative six nearest neighbours in an octahedral site, it can exist only at the higher pressure (< 10 GPa) [48]. This structure is not epitaxially stable.

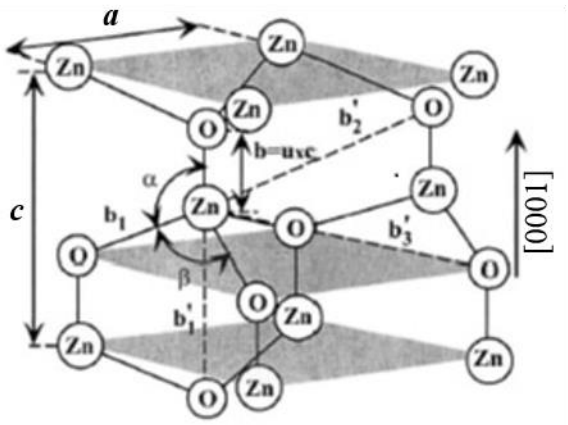

Figure 2.6: Schematic of the detailed structure of the wurtzite lattice of ZnO. Second-nearest-neighbour distances, u, and bond angles α and β = 109.47˚, are also shown [50].

Fig. 2.6 shows more details of the wurtzite lattice. As mentioned earlier, the wurtzite lattice is the preferred structure of ZnO crystal and is composed of two interpenetrating hexagonal close-packed (hcp) sub-lattices, each of which consists of one type of atom displaced with respect to each other along the threefold c-axis, by the amount u = 3/8 = 0.375 (in an ideal wurtzite structure) [17]. This unique structure plays a crucial role in piezoelectrical properties in ZnO, as well as the generation of defects, etching, and crystal growth. The lattice parameters *a, b* and *c*, and the internal parameter *u* are shown in the figure. The internal parameter *u* is defined as the length of the bond parallel to the c-axis (anion-cation bond length or the nearest-neighbour distance) divided by the lattice parameter *c*. The lattice constants of the ZnO unit cell are $a = b$ =3.2495 Å and c = 5.20628 Å, yielding a *c/a* ratio of 1.602, which is close to the ideal value of 1.633 expected for the *hcp* unit cell [51]. The Zn-O bond length is 1.992 Å in the direction parallel to the *c*-axis of the hexagonal unit cell and 1.973 Å in the other three directions of the tetrahedral arrangement [52]. In a real ZnO crystal, the wurtzite structure deviates from the ideal arrangement as the *c/a* ratio or the *u* value changes. It should be pointed out that a strong correlation exists between the *c/a* ratio and the *u* parameter, in that when the *c/a* ratio decreases, the *u* parameter increases such that the four tetrahedral distances remain nearly constant. This is achieved through a distortion of the tetrahedral angles due to long-range polar interactions. In addition to intrinsic material properties, the lattice parameters are affected by extrinsic properties such as the free electron concentration (via the deformation

potential of the conduction band minimum), the concentration of foreign impurities with different ionic radii which can replace the host atom, substrate-induced strain and temperature [53].

Growth facets of ZnO nanorods

The tetrahedral structure in ZnO unit cell gives rise to polar asymmetry along the hexagonal axis. The distribution of the cations and anions could take specific configuration as determined by crystallography technique resulting in four common surfaces. Some of these surfaces can be terminated entirely with cations or anions, resulting in positively or negatively charged surfaces, called polar surfaces which are responsible for the spontaneous polarization of ZnO. The polar surfaces of ZnO are Zn (0001) and O ($000\bar{1}$) basal planes with termination faces along the c axis, while ($11\bar{2}0$) and ($10\bar{1}0$) constitute non-polar faces with an equal number of zinc (Zn) and oxygen (O) atoms. These polar surfaces of the ZnO have untransferable and unchangeable ionic charges and their interaction at the surface depends on their distribution. Thus, in results, the structures have been shaped with a minimal electrostatic energy which is responsible for the fabrication of polar surface dominated ZnO nanostructures such as nanowires, nanorods, nanotubes, nanospring, nanocages, nanobelts and etc. Furthermore, the existence of polar surfaces in the crystal structure of ZnO is known to be responsible for different chemical and physical properties as a well as a key factor during crystal growth and defect generation in ZnO. The polar surfaces contribute to the variety of ZnO nanostructures by surface reconstruction to maintain a stable structure. For instance, in a one-dimensional structure (like nanorods) the oppositely charged ions produced result in a normal dipole moment and spontaneous polarization along the c-axis as well as a divergence in surface energy, thus assisting the growth of the structures. Whereby, the relative growth rate of these crystal faces will determine the final shape and aspect ratio of the ZnO nanostructures.

2.5 Electronic band structure

Considering that ZnO is a candidate semiconductor for optoelectronic device applications, a clear understanding of the band structure is of critical importance in explaining the optical and electrical properties as means towards improving the device performance. The process of optical absorption and emission have been influenced by bound excitons which are extrinsic transition related to dopants or defects thereby usually responsible for creating discrete electronic states in the band gap. Theoretically, neutral or charged donors and

acceptors are the members by which exciton could be bound with and it merely depends on the band structure of semiconductor material.

Therefore, since the development of ZnO as a semiconductor, various theoretical and experimental approaches have been devoted to understanding its band structure. The theoretical approaches used to calculate the band structure of wurtzite ZnO include the First-principle (FP) calculations [54, 55] the Green's functional method (KKB) [56] a self-interaction corrected pseudo-potential (SIC-PP) or the empirical tight-binding Hamiltonian, and local density approximation (LDA) [56, 57] techniques. On the other hand, the common experimental approaches used to measure the electronic core levels in solids are the emission techniques, UV-diffuse reflectance/absorption, X-ray induced photoabsorption, and low energy electron diffraction methods.

A qualitative agreement between the theoretical and experimental results has been made regarding the wide and direct band gap of the wurtzite structure of the ZnO. However, a quantitative disagreement regarding the Zn 3d state remained a challenge. Recent theoretical calculations have reported good agreement with the experimental studies by including the Zn 3d as a core level in their calculations. For example, D. Vogel et al. [58] further improved the LDA method by incorporating atomic self-interaction corrected pseudo potentials (SIC-PP), in which Zn 3*d* electrons had been accurately taken into account to calculate the electronic band structure of ZnO. The corresponding results of the band structure E(k) for wurtzite ZnO is given along the symmetry lines in the Brillouin zone as shown in Figs. 2.7.

These methods measure the optical band gap energy between the occupied and empty bands in ZnO. This energy represents the energy difference between full and empty states. The top filled states are called the valence band and the maximum energy of the valence band of states is called the VBM. The lowest band of empty states above the gap is called the conduction band with the lowest point in that band called the CBM. It could be seen that both the VBM and the CBM coincide at Γ point (K = 0), indicating that ZnO is a direct band gap semiconductor. The horizontal dashed lines indicate the measured gap energy and d-band width. The conduction band of wurtzite ZnO is constructed from s-like states and it is symmetrical about the Γ point, while the valence band is constructed mainly from p-like states.

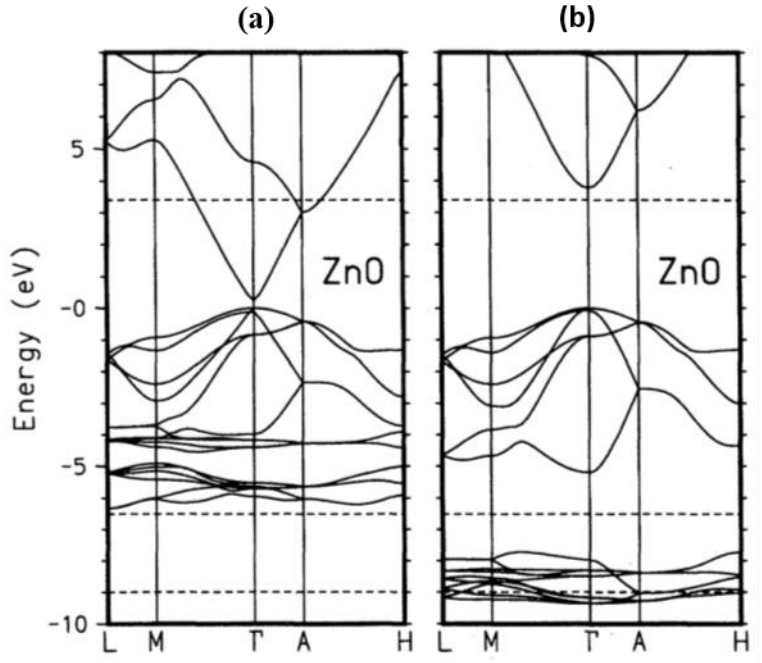

Figure 2.7: (a) Electronic Band structure of bulk wurtzite ZnO computed by (a) local density approximation (LDA) and (b) self-interaction corrected pseudo-potential (SIC-PP) methods [Reprinted with permission from [58], Copyright 1995 by the American Physical Society].

The band gap as determined from the standard LDA calculations is only ~3 eV, as shown in Fig. 2.7(a). This shrunk band gap was obtained because 3d states have been treated as core levels in order to simplify the calculations in the standard LDA method. According to the calculation results from the SIC-PP method, the bottom 10 bands (occurring around -9 eV) correspond to Zn 3*d* levels as shown in Fig. 2.7(b). The next 6 bands from -5 eV to 0 eV are derived from the 2*p* orbitals of oxygen. The first two conduction band states are strongly Zn localized and correspond to unoccupied Zn 3*s* levels. In contrast to the left panel, the d-bands are shifted down in energy considerably and concomitantly the gap is opened drastically. In addition, the dispersion and bandwidth of the O 2p valence bands are changed significantly. The gap energy and the d-band position are grossly improved as compared to the standard LDA results. Consequently, the band gap determined from SIC-PP method is 3.4 eV, which is very close to the experimental results (3.37 eV) which proves that the band gap energy and d-band position have been significantly improved as compared to the standard LDA results.

Additionally, it is also worth to know that the ZnO valence band is split experimentally by crystal field and spin-orbit interaction into three states named A, B and C under the wurtzite symmetry. This splitting is schematically illustrated in Fig. 2.8. The A and C subbands are known to possess Γ7 symmetry, whilst the middle band, B, has Γ9 symmetry.

These three bands correspond to a light hole (A), heavy holes (B) and the crystal field split band (C). The band splitting values are measured at 4.2 K [59].

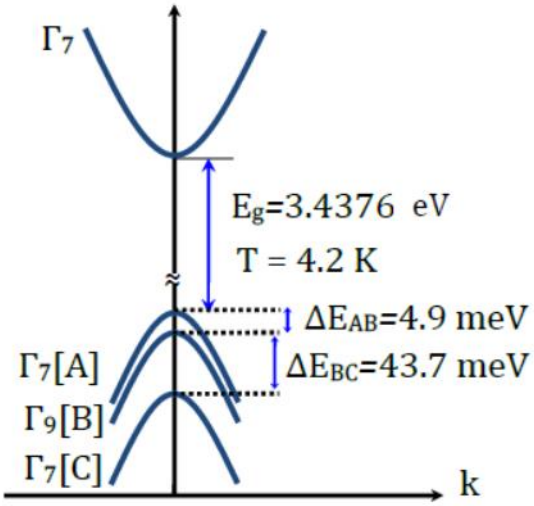

Figure 2.8: Low-temperature band structure of ZnO showing valence band splitting into three (A, B, C) which is caused by crystal field and spin-orbit splitting [60].

2.6 Physical and mechanical properties of ZnO

Numerous theoretical and experimental studies have been carried out to determine the physical properties of ZnO. The fundamental physical parameters of ZnO in the wurtzite structure at the room temperature are listed in table 2.1. However, there is still some uncertainty in the values of the thermal conductivity and the effective mass of the hole mobility due to the presence of some crystal defects in the material [61]. In addition, a stable and reproducible p-type doping in ZnO is still a challenge and cannot be achieved. The findings regarding the values related to the mobility of hole and its effective mass are still arguable. The values of the carrier mobility can surely be enhanced after achieving good control on the defects in the material [61].

It is well known that the mechanical properties of a semiconductor are essential for electromechanical applications such as transducers, actuators, etc. These properties are fundamentally described by hardness, piezoelectric constant, stiffness, yield stress and Young's and bulk modulus parameters. Since ZnO lacks central symmetry in its crystal structure, it contains piezoelectric characteristics in the form of stress and strain. The strain (ε), is observed when an external force induces deformation in a solid structure, but the internal mechanical force that opposes the solid deformation and tries to conserve its initial state is quantified by a physical stress (σ). The values of stress (σ) and strain (ε) are directly correlated.

Table 2.1: Basic physical properties of wurtzite ZnO at room temperature [62, 63]

Physical properties	Value
Lattice constants (nm)	a_o = 0.32495, c_o = 0.52069
Density g/cm^3	5.606
Molecular mass (g/mol)	81.389
Space group, lattice type	P6$_3$mc (Wurtzite)
Melting point (℃)	1975
Boiling point (℃)	2360
Thermal conductivity W/Km	0.6-1.2
Linear expansion coefficient (/℃)	*a*: 6.5x10^{-6}, *c*: 3.0x10^{-6}
Static dielectric constant	8.656
Refractive index	2.008-2.029
Energy band gap (eV)	3.3714, direct
Exciton binding energy (meV)	60
Electron effective mass (m$_o$)	0.24
Electron Hall mobility (low n-type conductivity) cm^2/Vs	200
Hole effective mass (m$_o$)	0.59
Hole Hall Mobility (for low p-type conductivity) cm^2/Vs	5-50
Static dielectric constant	8.656
Debye Temperature (^{o}K)	370
Intrinsic carrier concentration (cm^{-3})	< 10^6 cm^{-3} (max n-type >10^{20} cm^{-3} electrons; max p-type < 10^{17} cm^{-3})
Lattice energy (kcal/mole)	964
Piezoelectric coefficient (pC/N)	D33 = 12
Electron mobility (cm^2/Vs)	~210

More so, the mechanical stress and strain can be converted into electric power and vice-versa a property which makes ZnO attract considerable attention for use in self-powered devices applications at the nanoscale level. Many investigations have been done on ZnO nanostructures based on its mechanical properties, for instance, Xu et al. [64] have studied ZnO nanowires for producing electric power, while Riaz et al. [65] reported buckling and elastic stability of vertical ZnO nanorods and nanotubes quantitatively by the nano-indentation technique. In our study, we reported severally on the effects of different growth parameters on the strain and stress within the structures of ZnO nanostructures. The calculations were based on data obtained from XRD technique.

2.7 Applications of ZnO nanostructures

ZnO has gathered great interest in nanoscience due to its diverse and versatile properties which give rise to varied applications. For instance, the wide band gap of ZnO makes ZnO

material suitable to form clusters consisting of ZnO nanocrystals and ZnO nanowires. The wide band gap also favours the synthesis of p-n homojunctions as reported in some literature. Many fine optical devices can be fabricated based on the free-exciton binding energy in ZnO that is 60 meV because large exciton binding energy makes ZnO eligible to persist at room temperature and higher too. One-dimensional (1-D) ZnO nanostructures with well distributed and highly aligned properties are considered to be one of the most important nanomaterials for fabricating nanodevices for applications in various areas as highlighted at the introduction of this chapter. The ZnO nanopowders are spin-coated on a substrate for thin film applications.

Thin films

Thin film can be defined as a material created by the random nucleation and growth processes of individually condensing/reacting atomic/ionic/molecular species on a substrate. The structural, chemical, metallurgical and physical properties of such materials are strongly dependent on a number of deposition parameters and thickness [66]. Thin films have very interesting properties that are quite different from those of the bulk materials which they are made of. As the film becomes thinner, the surface properties become more important than the bulk. The other cause of interest is the miniaturization of elements such as electronic resistors, thin film transistors and capacitors. This is because of the fact that their properties depend on a number of interrelated parameters and also the deposition technique. The thin films are characterized by the thickness, crystalline orientation and multilayer aspects. Electronic semiconductor devices and optical coating are the main applications benefiting from thin films constrictions [67]. Thin films have numerous applications in protection, where the thin layer protect the coated material from corrosion, oxidation and wear; in optics to enhance (increase, decrease or filter) the material's transmittance or reflectance for a certain wavelength, and also for the color separation [68]; and in electronic devices [66]. Coating (deposition) of a thin layer onto substrates will facilitate the process of integrating a huge number of devices in one chip. The thin film is used in integrated circuits (IC), flat panel displays (FPD), light emitting diodes (LED), etc.

References

[1] S. M. U. Ali, Fabrication and characterization of ZnO nanostructures for sensing and photonic device applications, Linköping University Electronic Press, Doctoral dissertation, 2012.

[2] Ü. Özgür, Y. I. Alivov, C. Liu, A. Teke, M. Reshchikov, S. Doğan, H. Morkoc, Journal of applied physics 98(4), (2005) 11.

[3] Z. L. Wang, Materials Science and Engineering: R: Reports 64(3), (2009) 33-71.

[4] G. C. Yi, C. Wang, W. I. Park, Semiconductor Science and Technology 20(4), S22-S34

[5] N. H. Alvi, S. U. Ali, S. Hussain, O. Nur, M. Willander, *Scripta Materialia*, *64*(8), (2011) 697-700.

[6] S. M. Usman Ali, M. H. Asif, A. Fulati, O. Nur, M. Willander, C, Brännmark, P. Strålfors, U. H. Englund, F. Elinder, B. Danielsson, Nanotechnology, IEEE Transactionon 10, (2011) 913-919.

[7] Y. Li, F. Della Valle, M. Simonnet, I. Yamada, J. J. Delaunay, Nanotechnology 20(4), (2008) 045501.

[8] M. S. Arnold, P. Avouris, Z. W. Pan, Z. L. Wang, The Journal of Physical Chemistry B 107(3), (2003) 659-663.

[9] C. H. Liu, W. C. Yiu, F. C. K. Au, J. X. Ding, C. S. Lee, S. T. Lee, Applied physics letters, 83(15), (2003) 3168-3170.

[10] Wang, Yan-Xin, Qi-Feng Zhang, Hui Sun, Yan-Ling Chang, Jin-Lei Wu, Acta Phys. Sin (2008), 1141-1144.

[11] B. Weintraub, Y. G. Wei, Z. L. Wang, Angewandte Chemie International Edition, 48(47), (2009) 8981-8985.

[12] J. Zhou, N. S. Xu, Z. L. Wang, Advanced Materials 18(18), (2006) 2432-2435.

[13] Z. Li, R. Yang, M. Yu, F. Bai, C. Li, Z. L. Wang, The Journal of Physical Chemistry C 112(51), (2008) 20114-20117.

[14] J. C. Johnson, H. Yan, R. D. Schaller, P. B. Petersen, P. Yang, R. J. Saykally, Nano Letters 2(4), (2002) 279-283.

[15] C. Ronning, P. X. Gao, Y. Ding, Z. L. Wang, D. Schwen, Applied physics letters 84(5), (2004) 783-785.

[16] J. Qiu, W. Yu, X. Gao, X. Li, Nanotechnology 17, (2006) 4695-4698.

[17] H. Morkoc, U. Ozgur, Zinc Oxide: Fundamentals, Materials and Device Technology. ISBN: 9783-527-40813-9 Ed., Germany: WILEY-VCH, 2009.

[18] Z. N. Urgessa, Growth and Characterization of ZnO Nanorods using chemical bath deposition, Nelson Mandela Metropolitan University, PhD thesis 2012.

[19] M. Sulkesa and Z. Sulkes, Am. J. Phys. 79, (2011) 11.

[20] F. Clabau, X. Rocquefelte, S. Jobic, P. Deniard, M. H. Whangbo, A. Garcia, T. Le Mercier, Chemistry of Materials 17(15), (2005) 3904-3912.

[21] Bernard Valeur, Molecular Fluorescence Principles and Applications, New York: Wiley-VCH, 2001.

[22] R. Dingle, Phys. Rev. Lett. 23, (1969) 579 581 Communication 145 (2008) 321-326.

[23] K. Vanheusden, W. L. Warren, C. H. Seager, D. R. Tallant, J. A. Voigt, B. E. Gnade, Journal of Applied Physics 79(10), (1996) 7983-7990.

[24] S. Yamauchi, Y. Goto, T. Hariu, Journal of Crystal Growth 260(1), (2004) 1-6.

[25] K. Johnston, M. O. Henry, D. M. Cabe T. Agne, T. Wichert, Proceedings of the Second Workshop on "SOXESS European Network on ZnO, 27-30 October, Caernarfon, Wales, UK, 2004.

[26] J. Zhong, A. H. Kitai, P. Mascher, W. Puff, Journal of the Electrochemical Society 140(12), (1993) 3644-3649.

[27] M. Liu, A. H. Kitai, P. Mascher, Journal of Luminescence 54(1), (1992) 35-42.

[28] X. Yang, G. Du, X. Wang, J. Wang, B. Liu, Y. Zhang, S. Yang, Journal of crystal growth 252(1), (2003) 275-278.

[29] N. H. Alvi, K. Ul Hasan, O. Nur, M. Willander, Nanoscale research letters 6(1), (2011) 130.

[30] C. H. Ahn, Y. Y. Kim, D. C. Kim, S. K. Mohanta, H. K. Cho, Journal of Applied Physics 105(1), (2009) 013502.

[31] A. van Dijken, E. A. Meulenkamp, D. Vanmaekelbergh, A. Meijerink, The Journal of Physical Chemistry B 104(8), (2000) 1715-1723.

[32] Z. Fan, P. C. Chang, J. G. Lu, E. C. Walter, R. M. Penner, C. H. Lin, H. P. Lee, Applied Physics Letters 85(25), (2004) 6128-6130.

[33] D. C. Reynolds, D. C. Look, B. Jogai, H. Morkoc, Solid State Communications 101(9), (1997) 643-646.

[34] Liu, Mi, A. H. Kitai, P. Mascher, Journal of Luminescence 54.1, (1992) 35-42.

[35] P. Klason, T. M. Borseth, Q. X. Zhao, B. G. Svensson, A. Y. Kuznetsov, M. Willander, Solid State Communications 145(5), (2008) 321-326.

[36] F. Oba, S. R. Nishitani, S. Isotani, H. Adachi, I. Tanaka, Journal of Applied Physics 90(2), (2001) 824-828.

[37] S. M. Usman Ali, N.H. Alvi, Z. Ibupoto, O. Nur, M. Willander, B. Danielsson, Sensors and Actuators B: Chemical 152(2), (2011) 241-247.

[38] M. Liu, A. H. Kitai, P. Mascher, Journal of Luminescence 54(1), (1992) 35-42.

[39] W. M. Kwok, Y. H. Leung, A. B. Djurisic, W. K. Chan, D. L. Phillips, Applied Physics Letters 87(9), (2005) 093108.

[40] A. Janotti, C. G. Van de Walle, Physical Review B 76(16), (2007) 165202.

[41] S. A. Studenikin, N. Golego, M. Cocivera, Journal of Applied Physics 84(4), (1998) 2287-2294.

[42] M. Razeghi, A. Rogalski, Journal of Applied Physics 79(10), (1996) 7433-7473.

[43] D. Zwingel, Journal of Luminescence 5(6), (1972) 385-405.

[44] O. F. Schirmer, D. Zwingel, Solid State Communications 8(19), (1970) 1559-1563.

[45] J. M. Smith, W. E. Vehse, Physics Letters A 31(3), (1970) 147-148.

[46] V. A. Coleman, C. Jagadish, Processing, properties and applications, (2006) 1-20.

[47] Z. L. Wang, Phys.: Condens. Matter 16, (2004) R829–R858.

[48] C. H. Bates, W. B. White, R. Roy, Science 137(3534), (1962) 993-993.

[49] C. Jagadish, S. J. Pearton, (Eds.). Zinc oxide bulk, thin films and nanostructures: processing, properties, and applications. Elsevier, (2011).

[50] Z. G. Yu, H. Gong, Pi. Wu, Journal of crystal growth 287(1), (2006) 199-203.

[51] M. Mehrabian, R. Azimirad, K. Mirabbaszadeh, H. Afarideh, M. Davoudian, Physica E: Low-dimensional Systems and Nanostructures 43(6), (2011) 1141-1145.

[52] A. El-Shaer, MBE growth and characterization of ZnO-based layer and hetrojuction, Universitat Carol- Wilhelmina zu Braunschweig, PhD thesis 2008.

[53] M. H. Huang, Y. Wu, H. Feick, N. Tran, E. Weber, P. Yang, Advanced Materials 13(2), (2001) 113-116.

[54] P. Schröer, P. Krüger, J. Pollmann, Physical Review B, 47(12), (1993) 6971.

[55] A. Schleife, F. Fuchs, J. Furthmüller, F. Bechstedt, Physical Review B, 73(24), (2006) 245212.

[56] S. Bloom, I. Ortenburger, Physica status solidi (b) 58(2), (1973) 561-566.

[57] U. Rössler, Physical Review 184(3), (1969) 733-738.

[58] D. Vogel, P. Krüger, J. Pollmann, Physical Review B, 52(20), (1995) R14316.

[59] B. K. Meyer, H. Alves, D. M. Hofmann, W. Kriegseis, D. Forster, F. Bertram, U. Haboeck, Physica status solidi (b) 241(2), (2004) 231-260.

[60] A. R. H. Preston, B. J. Ruck, L. F. J. Piper, A. DeMasi, K. E. Smith, A. Schleife, S. M. Durbin, Physical Review B 78(15), (2008) 155114.

[61] D. I. Florescu, L. G. Mourokh, F. H. Pollak, D. C. Look, G. Cantwell, X. Li, Journal of applied physics 91(2), (2002) 890-892.

[62] J. G. Lu, Z. Z. Ye, J. Y. Huang, L. P. Zhu, B. H. Zhao, Z. L. Wang, S. Fujita, Applied physics letters 88(6), (2006) 063110.

[63] J. K. Dangbegnon, Nelson Mandela Metropolitan University, PhD thesis 2010.

[64] S. Xu, Y. Qin, C. Xu, Y. Wei, R. Yang, Z. L. Wang, Nature nanotechnology 5(5), (2010) 366-373.

[65] M. Riaz, A. Fulati, G. Amin, N. H. Alvi, O. Nur, M. Willander, Journal of Applied Physics 106(3), (2009) 034309.

[66] J. Poortmans, V. Arkhipov (Eds.), thin film solar cells: fabrication, characterization and applications, England: John Wiley & Sons, (2007).

[67] C. K. Nain, K. A. Maini, Thin films and their application in military and civil sectors, DRDO, New Delhi, 2010.

[68] K. Ellmer, A. Klein, B. Reche, Transparent conductive zinc oxide basics and applications in thin film solar cells, Springer Science & Business Media, New York, USA, 2008

Chapter 3

Experimental methods and characterization techniques

Brief accounts of the synthesis and characterization methods used in this study are introduced in this chapter. Un-doped, Ga/Al-doped and co-doped ZnO NPs were prepared using the reflux precipitation method; GZO nanopowders were deposited on a glass substrate using the spin coating technique to form the transparent conducting film seed layer upon which ZNRs were grown using the CBD technique. Various characterization techniques were used to analyze and to investigate the nanopowders and thin films properties. The techniques used include the x-ray diffraction (XRD), scanning electron microscopy (SEM), energy-dispersive x-ray spectroscopy (EDS) and atomic force microscopy (AFM) which were used to study structural, morphological, elemental composition and topographical properties of the samples. photoluminescence (PL), cathodoluminescence (CL) and UV-Vis spectroscopies were used for luminescence and optical properties investigations.

3.1 Growth and deposition techniques

3.1.1 Reflux-precipitation method and growth of doped and un-doped ZnO nanopowders

Reflux precipitation method

A number of specific methods have been developed in the synthesis of doped and un-doped ZnO nanostructures. The common ones are sol-gel, emulsion, hydrothermal, chemical bath deposition and the co-precipitation methods. The sol-gel technique [1] is a wet chemical process used in the fabrication of metal oxides from a chemical solution, and this acts as a precursor for an integrated network (gel) of discrete particles. The precursor solution can be either deposited on the substrate to form a film, cast into a suitable container with the

desired shape, or used to synthesize powders. The emulsion methods [2] micro-emulsion or direct/inverse micelles represent an approach based on the formation of micro/nano-reaction vessels from a ternary mixture containing water, a surfactant and oil. Metal precursors in water will precede precipitation as oxo-hydroxides within the aqueous droplets, typically leading to mono-dispersed materials with sizes limited by the surfactant-hydroxide contact. In hydrothermal methods [2,3] the metal complexes are decomposed thermally either by boiling in an inert atmosphere or by using an autoclave with the help of higher temperatures (160-280 ˚C) [3] and pressures (90–930 psi). A suitable surfactant agent is usually added to the reaction media to control particle size and limit agglomeration. The chemical bath deposition [2] (CBD) on the other hand, is a technique that produces a solid film on a substrate during a single immersion through the control of the kinetics of formation of the solid. This method would be discussed in details in the sub-section of this chapter since it is the technique employed to grow the ZnO NRs in this project. Importantly, the co-precipitation method [4] involves dissolving a salt precursor in water (or another solvent) to precipitate the nanoparticles, which form with the help of a base.

In this study, we have adopted a version of co-precipitation referred to as the reflux-precipitation method to synthesize the un-doped, Ga and/or Al-doped ZnO nanoparticles (NPs). The method involves the use of reflux system in the production unit of the experiment. The reflux precipitation method was used in the synthesis of the NPs because it offers several advantages over the methods mentioned above and others such as the thermal vapour deposition laser ablation, vacuum arc deposition and electrochemical process. These other methods, reportedly, possess many complex steps; require sophisticated equipment and rigorous experimental conditions [5] which demand very high power synthesis conditions in temperature or pressure that make sizing up of the product a daunting challenge unlike the reflux precipitation method which allows synthesis at low temperatures, using simple equipment and at low-cost. The versatility of the reflux precipitation method allows the modification of various growth conditions such as the temperature, growth duration, precursor concentration and the pH which are crucial in engineering the structural and optical properties of the nanomaterials.

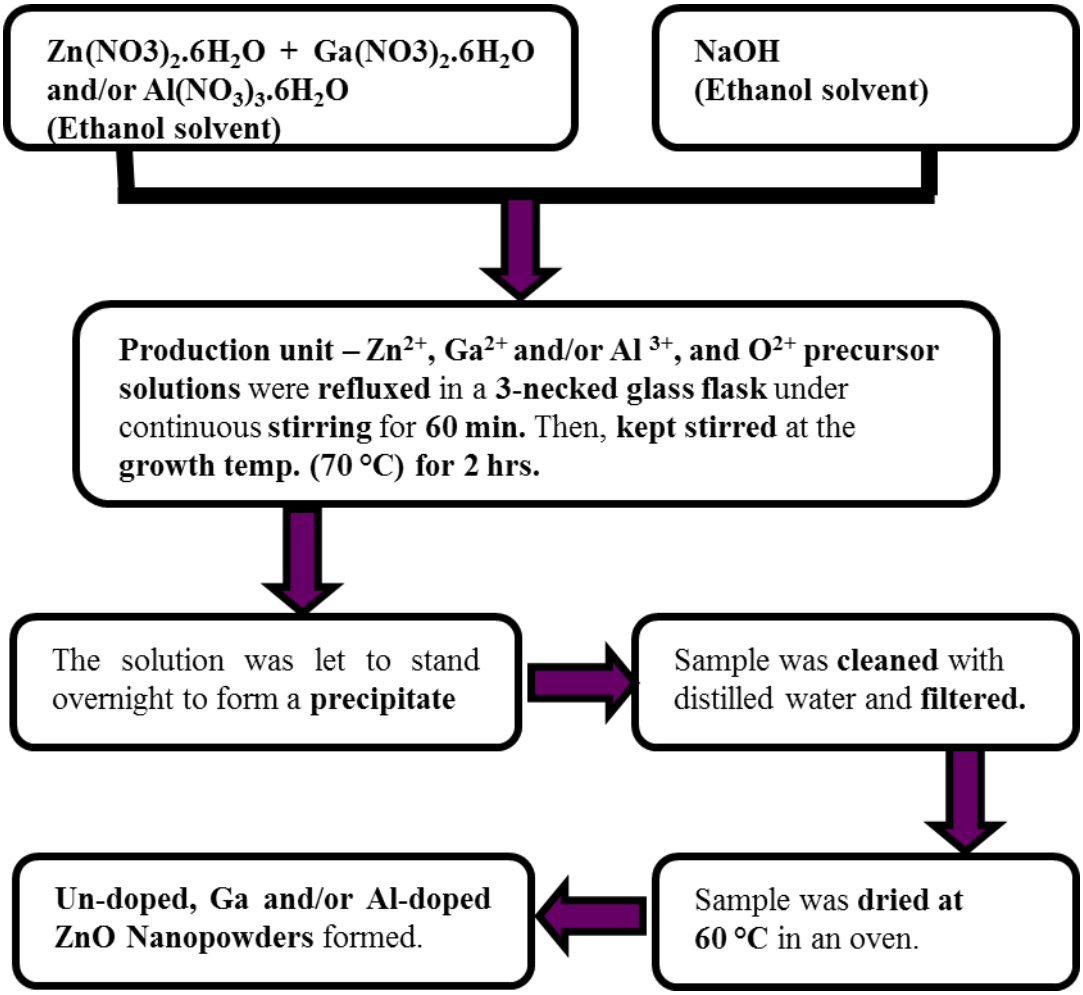

Figure 3.1: Flow diagram of the reflux-precipitation process used in the synthesis of un-doped, Ga and/or Al-doped ZnO nanoparticles.

Essentially, in the present study, the NPs were grown using zinc nitrate hexahydrate and/ or aluminium nitrate hexahydrate as zinc and Al precursors respectively together with sodium hydroxide as a source of hydroxyl groups. Ethanol was used as a solvent, while distilled water for cleaning the samples. Fig. 3.1 shows the general procedure followed in the reflux-precipitation method for the synthesis of the NPs. The procedure entails making of precursor solutions, the reaction in the production unit, precipitation and cleaning of the samples, drying and annealing processes. The details on the synthesis procedure are provided under experimental sections of chapters 4-7 of this work.

3.1.2 Deposition of Ga-doped ZnO thin film and spin coating technique

In the present research work, the optimized Ga-doped ZnO (GZO) nanopowders prepared using the reflux-precipitation method were deposited on glass substrates to form thin films

using the spin-coating technique. This fabrication process involved substrate pre-treatment and spin-coating process.

Substrate preparation

Pre-cleaning treatment of substrates is very crucial for fabricating the high quality and vertically aligned nanowires/nanorods, nanotubes and nanowalls because the unwanted chemicals, and foreign matters on the surface of the substrates, as well as the oxide layers on the glass surface can generate the instability and unpredictability during processing. The glass substrates were, initially, immersed in an acidic solution in order to remove the native oxide layers from the surface and then treated with acetone, methanol and ethanol for 5 minutes each in a sonicator. After the sonication, the substrates were dried using high-pressure nitrogen gas.

Spin coating

The spin coating technique has found a large endorsement among the research community because it is fast, simple and low-cost technique; can easily produce a homogenous and uniform film and has a low crystallization temperature.

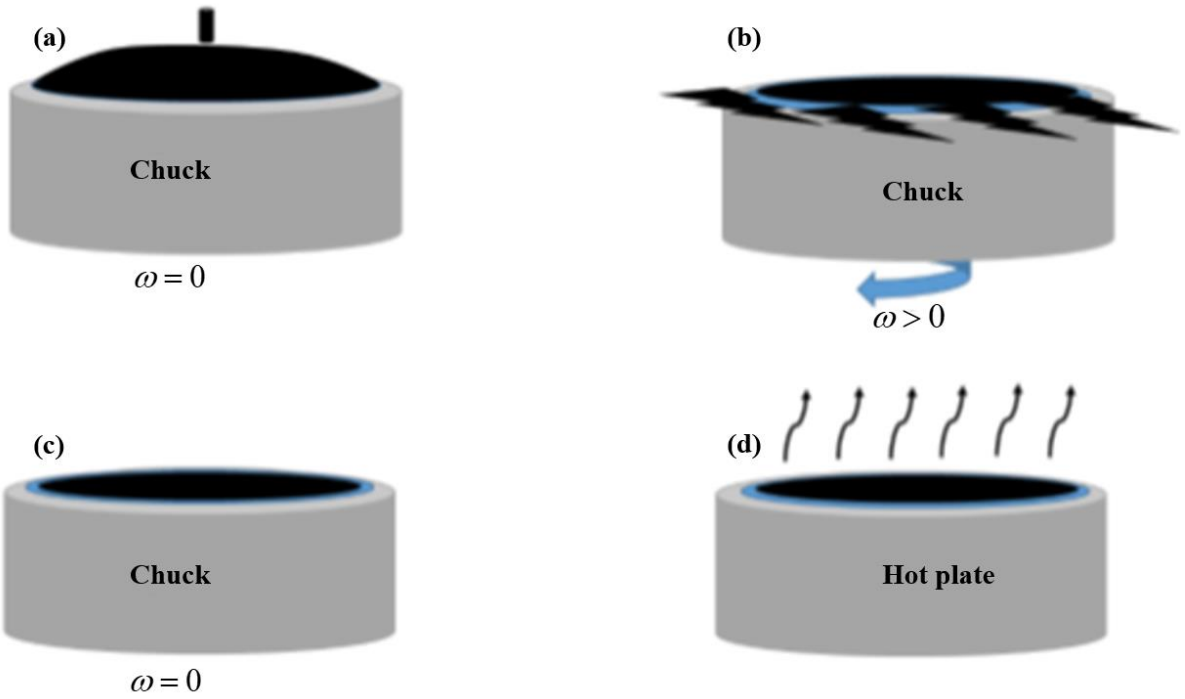

Figure 3.2: Schematic diagram of the spin coating processes.

The typical spin coating procedure is illustrated in Fig. 3.2. The process begins with dispensing of a small amount of fluid solution onto a spun (rotated) substrate. The spinning induces a centripetal force on the substrate surface, which in turn causes the solution to

spread off toward the substrate edges, leaving a thin layer of the dispensed material. The solution mostly contains organic solvents, therefore, this process may be followed by heating to evaporate the solvents and then the desired material will be left as the thin layer.

The final properties of the deposited film are dependent on different parameters. These include the factors related to the machine (spinning speed, spin acceleration toward the final speed and the time of the spinning); the viscosity and molarity of the solution; the substrate material and structure; the annealing processes as well as environment upon the substrate (air speed, quality, humidity, dust particles and the noise created by the operator).

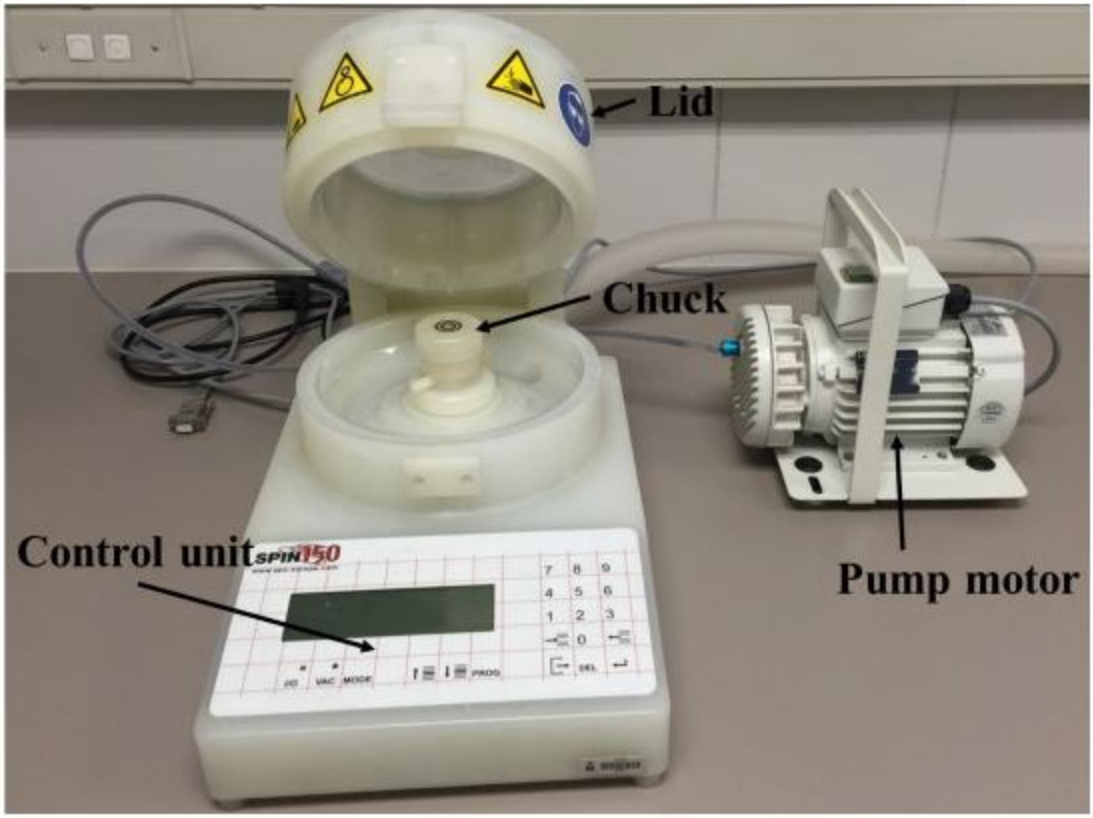

Figure 3.3: SPEN 150 spin coater from semiconductor production system at the University of the Free State.

Fig. 3.3 shows the spin coater system used in this research. The main parts of the system are the rotatable chuck used to hold and spin the substrate, the lid used to cover the machine during the deposition process, the pump motor to provide vacuum to hold the substrate on the chuck and the bowl which contains the system parts. Among the few disadvantages of the spin coating technique are the fact that only a small per centage (2-5 %) [6] of the dispensed solution will be utilized, while the rest of the solution is flung into the bowl and as the substrate size increases, the sufficient spinning rate is found to decrease.

3.1.3 Growth of ZnO nanorods and the chemical bath deposition technique

The ZnO nanorods were grown on Ga-doped ZnO seeded glass substrate using the CBD method. The experimental procedures and the growth mechanism of ZnO NRs from hexamine and zinc nitrate using CBD are discussed in Chapters 8 and 9 of this work. However, some pertinent literature on the CBD technique is highlighted in this section. They include the brief history, advantages and basic principle of CBD, the nucleation and crystal growth techniques and also the factors affecting thin film deposition process in CBD.

Overview of the CBD method

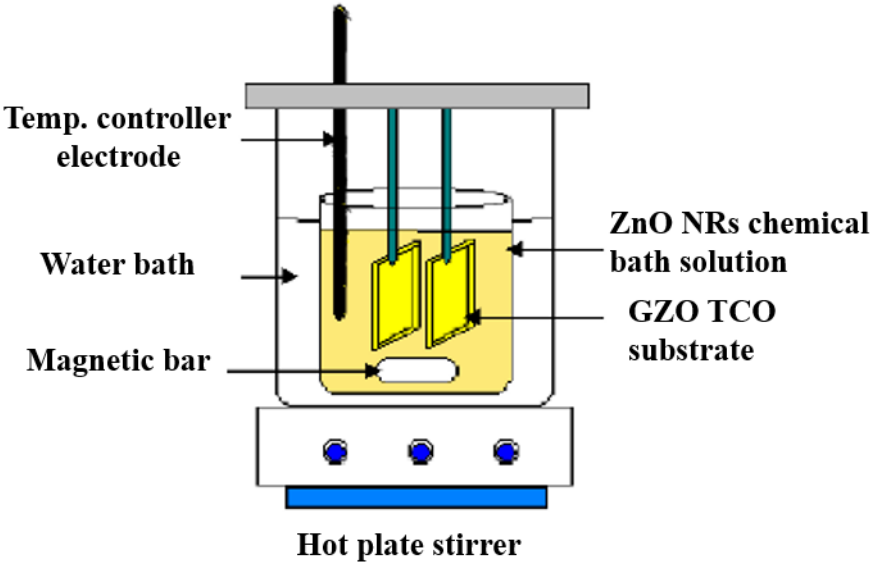

Figure 3.4: Schematic diagram of the apparatus used for the growth of ZnO NRs by CBD

The thin film deposition technologies are either purely physical methods (Top-down approach) or purely chemical (Bottom-up approach) methods [7,8]. In physical methods, the film material is moved from a target source with some form of energy to the substrate. This method is widely used in compound thin films. Examples of physical methods include the vacuum evaporation, various sputtering techniques, spray pyrolysis, electrodeposition, ion beam assisted coating and molecular beam epitaxy. Chemical film fabrication method involves chemical reaction and the precursors are mostly components undergoing reaction at the substrate surface or in the vicinity of the substrate. Under chemical methods, we have the gas phase chemical processes such as conventional chemical vapour deposition (CVD), laser CVD, metal organochemical deposition (MOCVD) and plasma enhanced chemical

vapour deposition. Liquid phase chemical techniques include electrodeposition, chemical bath deposition (CBD), electrodeless deposition, anodization, successive ionic layer adsorption and reaction (SILAR), spray pyrolysis etc. [9]. In the present work, CBD technique is used for growth of ZNRs films on the Ga-doped ZnO seeded substrate. The setup similar to the one shown in Fig. 3.4 was employed.

The CBD process involves the deposition of a solid film on a substrate during a single immersion through the control of the kinetics of formation of the solid. The first recorded report of CBD crystal growth was published in 1933 by Bruckman who produced a PbS thin film from a solution containing lead acetate, thiourea and sodium hydroxide [10]. Since then CBD has been used to deposit films of a variety of semiconductors. In the recent two decades, it has been widely applied successfully, reproducibly, and at low cost, to the synthesis of thin films and other morphologies for solar cells. To this end, many different types of oxide nanostructures such as ZnO and TiO_2 materials have been successfully deposited by CBD method. For instance, Andres-Verges et al. [11] reported an aqueous solution growth method of ZnO for the first time in 1990. More than 10 years later, Vayssieres et al. [16] used this method to grow nanorods on a substrate. Since then CBD growth of ZnO nanorods becomes common practice. The most successful approach for the synthesis of ZnO nanorods involves the reaction between equimolar solutions of zinc nitrate hexahydrate ($Zn(NO_3)_2 \cdot 6H_2O$) and hexamine ($C_6H_{12}N_4$) [12-15].

The CBD method offers many advantages over its counterparts and therefore has drawn great interest among the researchers. Being an aqueous chemical growth method, CBD can be carried out at low temperatures (<100 ^oC), it is simple and cost-effective for the fabrication of nanostructures Vayssieres et al. [16]. It is particularly suitable since it does not require high-pressure containers and is also entirely recyclable, safe and environmentally friendly because only water or alcohols is used as a solvent. In addition, because no organic solvents or surfactants are present, the purity of the materials is substantially improved. The by-products (residual salts) are easily washed out by water due to their high solubility. In most cases, no additional heat or chemical treatment is necessary, which presents a significant improvement compared with surfactant, template, or membrane based synthesis methods. The technique is ideally suited for producing uniform films with thickness in the 0.05-0.3 μm range in most cases. This method is, thus, an increasingly important complement to other solution-based techniques in the fabrication of nanostructures. Nevertheless, CBD has also some shortcomings: Firstly, in the classical beaker configuration, the material yield during film formation is very low, about a few

percent, leading to an unnecessary waste production and increased treatment costs. The reason is that the volume to surface ratio is very high and that only a small part of the solution is contributing to the film formation, the remaining leading to the formation of colloids in the bulk of the solutions [17, 18]. Secondly, the formation of particles leads not only to the generation of a significant amount of waste but also to the creation of defects in the deposited film [19].

The basic working principle behind the CBD process is similar to those for all precipitation reactions and it is based on the relative solubility of the product. At a given temperature when the ionic product of reactants exceeds the solubility product, precipitation occurs. Whereas if the ionic product is less than the solubility product, then the solid phase produced will dissolve back to the solution resulting in no net precipitation [20]. The solubility product is mainly affected by the temperature, solvent and particle size [21]. The equilibrium between a precipitate and its ions in solution will shift according to whether the heat of solution is endothermic or exothermic [22]. Using a solvent of lower dielectric constant, the solubility of a moderately insoluble substance in water is reduced by the addition of alcohol or some other water-miscible solvent. As particle size decreases, solubility appears to increase. Consequently, the CBD technique can be used to deposit any compound that satisfies two basic requirements which are: the source of cations (metal) and anions (hydroxide) must dissolve preferably in water (or alcohol) and must form a crystal, and the formed crystal must be insoluble and chemically stable in the solvent used. The crystal formed can grow either by homogeneous nucleation in solution and/or by hetero-nucleation on a substrate.

Homogeneous nucleation can occur due to local fluctuations in the solution concentration, temperature, or other variables. The first stage of the growth is a collision between individual ions or molecules to form embryos. These embryos grow by collecting individual species that collide with them. In this type of growth, adsorption of ions on the embryo is expected to be the most probable growth mechanism. If the concentration of embryos in the solution is large, collisions between embryos can also play an important role. On the other hand, heterogeneous nucleation may take place as a result of two distinct mechanisms. The first one is a growth mechanism involving the reaction of atomic species at the surface of stable nuclei pre-coated onto the substrate or impurities on it. It corresponds to an atom-by-atom process, also called "ion-by-ion" [23]. The second deposition mechanism is associated with the oriented attachment (for polar crystals) of particles formed by homogeneous nucleation on the wetting/seed layer pre-coated onto the substrate [24, 25].

It can be considered a cluster-by-cluster growth. Whatever mechanism dominates, the general steps in such solution growth are expected to be: generation of growth species, diffusion from the bulk to the growth surface, adsorption and surface growth.

The balance between homogeneous and heterogeneous nucleation processes depends on the deposition mechanism. It is generally believed that high supersaturation levels favour homogeneous nucleation, whereas low supersaturation levels favour heterogeneous nucleation [26]. In order to maintain low supersaturation levels during the growth process, the nutrient supply has to be finely controlled. The formation of larger nuclei, which leads to precipitation, when the objective is to grow on pre-seeded substrates, is a waste of reagents. One common technique is the use of seeding layers to facilitate heterogeneous nucleation. Moreover, seeding of the substrate with nanoparticles lowers the thermodynamic barrier by providing nucleation sites, and hence improves the aspect ratios and optical properties, and ensures uniformity in the growth of ZnO nanostructures [27, 28]. This implies that any factor that will improve the seed layer will improve the as-synthesized nanostructures. In addition to supersaturation, the other main parameters that affect these nucleation processes are pH and temperature. The temperature, in particular, is an important thermodynamic factor and plays a key role in controlling crystal growth rate. Higher temperatures enhance the kinetic energy of the precursors and this favours homogeneous nucleation in the solution.

Clearly, the CBD technique involves several steps beginning with dissociation in solution the mass transport of reactants, chemical reaction, nucleation, desorption and thermal treatment for the desired crystal growth. Therefore, the technique offers the opportunity to control various growth parameters to determine and achieve desired film properties. These parameters include the concentrations of the precursors, the molar ratio of the metal to the base precursors, pH of the solution, growth time, growth temperature and the complexing agents. Fekadu et al [29], in their work on PbS thin films, showed that deposition growth time strongly influenced the preferred orientations of the crystallites as well as structural parameters such as average crystallite size, strain and dislocation density. The effect of the concentration of the reactants (cation and anion Sources) have been severally reported to influences the whole physical and chemical properties of the deposited thin film. For instance, Hodes et al [30] explained that by changing the composition of the reactive solution, competition between the processes of homogeneous and heterogeneous nucleation could be altered to favour thin film growth. The effect of growth temperature was also reported to affect the film deposition in a number of ways. For example, as temperature

increases dissociation of the complex increases hence the kinetic energy of the molecules also increases leading to the greater interaction between ions and subsequent deposition at volume nucleation centres of the substrate [31] and therefore influence the nucleation process as mentioned earlier. The effect of chemical bath solution pH is also reported to influence the reaction rate, as well as the rate of deposition because these parameters depend on the supersaturation condition and the rate of the formation of MX (where M and X is the number of metals and O-/ ions respectively). If the concentration of the ion in the solution is higher, the M ion concentration will lower and the reaction rate will be slow [32]. Similarly, the nature of the substrates used in CBD growth is crucial in order to obtain an adherent film [33, 34] while the complexing agent was reported to, among other effects, to influence the hydrolysis and concentration of the metal ions.

3.2 Characterization techniques

3.2.1 X-ray diffraction

Matter is a group of atoms arranged together, either randomly (amorphous) e.g. liquid and glass or regularly in a certain order (crystalline). In crystalline materials, the smallest volume is the unit cell which describes the crystal structure. Each crystalline material has a unique atomic arrangement (fingerprint) depending on the type of the unit cell.

XRD is the science of determining the arrangement of the atoms within a crystal from the manner in which a beam of X-rays is scattered from the electrons within the crystal. XRD is a versatile, non-destructive technique used to study the overall structure of bulk solids, including lattice constants, identification of unknown materials, the orientation of single crystals, the orientation of polycrystalline, stress, strain, texture, films thickness etc. XRD analysis can provide the crystalline quality and dominant crystallographic planes of the given material. In addition, the diffraction spectrum also provides information regarding the types of phases present in the material and can be used to calculate the approximate average grain size using Scherrer's equation [35]. Fig. 3.5 is an XRD spectra obtained for the ZnO NPs.

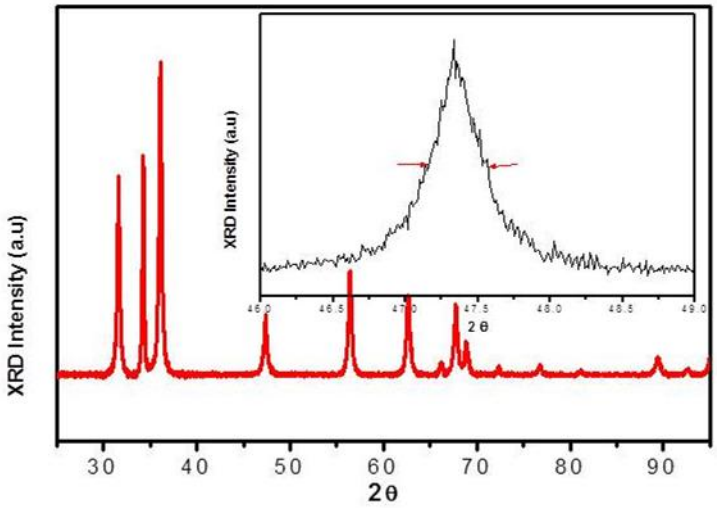

Figure 3.5: Typical XRD spectrum of ZnO nanoparticles.

In this study, the XRD data were collected using the D8 Bruker Advanced AXS GmbH X-ray powder diffraction system shown in Fig. 3.6 with a resolution of 0.02 ˚ for 2θ and a Cu-Kα x-ray tube (λ = 1.54056 Å). The X-ray scans were performed between 2θ values of 30° and 80° using a step size of 0.05 in almost all measurements.

Figure 3.6 D8 Bruker Advanced AXS GmbH X-ray diffractometer at the University of the Free State.

Bragg's Law

The principle of XRD is strongly correlated with Bragg's law. The atoms in crystals interact with X-rays in such a way as to produce interference. The interaction can be thought of as if the atoms in a crystal structure reflect the waves. But, because a crystal structure consists of an orderly arrangement of atoms, the reflections occur from the atomic planes.

Consider a beam of monochromatic X-rays entering a crystal with one of its planes oriented at an angle of θ to the incoming beam. The x-ray interacts with a crystal and is scattered by the atoms in adjacent planes. Fig. 3.7 shows two such X-rays, where the spacing between the atomic planes occurs over the distance, d.

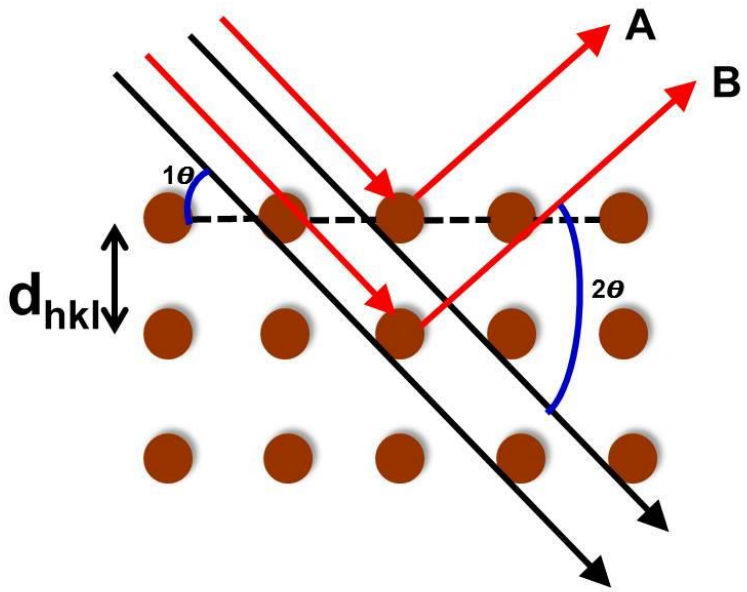

Figure 3.7: Monochromatic X-rays entering a crystal [6].

Ray A reflects off of the upper atomic plane at an angle θ equal to its angle of incidence. Similarly, Ray B reflects off the lower atomic plane at the same angle θ. While Ray B is in the crystal, however, it travels a distance of 2a farther than Ray A. If this distance 2a is equal to an integral number of wavelengths (nλ), then Rays A and B will be in phase on their exit from the crystal and constructive interference will occur. If the distance 2a is not an integral number of wavelengths, then destructive interference will occur and the waves will not be as strong as when they entered the crystal. Thus, the condition for constructive interference to occur is $n\lambda = 2a$. But, from trigonometry, we can figure out what the distance 2a is in terms of the spacing, d, between the atomic planes.

$$a = d \sin \theta, \text{ or } 2a = 2\ d \sin \theta, \text{ thus}$$

$$n\lambda = 2d \sin \theta \qquad (3.1)$$

This is known as Bragg's Law for X-ray diffraction.

What it says is that if we know the wavelength, λ, of the X-rays going into the crystal, and we can measure the angle θ of the diffracted X-rays coming out of the crystal, then we know the spacing (referred to as ***d-spacing***) between the atomic planes. Any atomic arrangement

(crystal) has a unique XRD pattern and the final XRD pattern will be obtained from the sharp interference maxima (peaks) that have occurred due to the constructive interferences.

The XRD method is used to analyze structural parameters such as crystallite size, microstrain (stress), Texture Coefficient and dislocation density (δ). The knowledge of such parameters especially for new materials is important prior to their technical applications [36]. Moreover, the XRD is the most convenient tool for crystallographic structural analysis like phase identification, phase quantification and lattice parameter refinement.

Crystallite size measurement

The diffraction peaks positions and relative intensities can be changed by the presence of various types of defects such as a small number of dislocations in crystals with dimensions of millimetres. The small size of grain size can be considered as another kind of defect and can change diffraction peak widths. Very small crystals cause peak broadening. The crystallite size is easily calculated as a function of peak width (specified as the full-width at half maximum peak intensity (FWHM)), peak position and wavelength using the Scherrer's formula [35].

$$D = \frac{K\lambda}{\beta_{1/2} Cos\theta_{\beta}} \tag{3.2}$$

Where, K is the shape factor (K = 0.94), D is the crystallite size of the particle, λ is the wavelength of the incident X-ray beam used (1.5405 Å); θ is the Bragg's diffraction angle; and ß is the full width at the half-maximum in radians. The Scherrer's formula is commonly used to estimate the size of very small crystals from measured width of their diffraction curves. Note that whether a value of K = 0.9 or 1 is used depends on shapes of the crystallites assumed to be the sample.

Determination of lattice parameters

For the wurtzite structure, the interplanar distance of {hkl} plane is related to the lattice parameters *a* and *c* via the Miller indices *hkl* and the diffraction peaks were observed to satisfy the equation below in the case of ZnO hexagonal structure [37].

$$\frac{1}{d^2_{(hkl)}} = \frac{4}{3}\left(\frac{h^2 + hk + k^2}{a^2}\right) + \frac{l^2}{C^2} \tag{3.3}$$

Where *d* is the spacing between planes of Miller indices *h, k,* and *l, a* and *c* are the lattice parameters. The lattice constants *a* for ⟨100⟩ plane is calculated by

$$a = \frac{\lambda}{\sqrt{3}\sin\theta} \tag{3.4}$$

For the (101) plane, the lattice constant c is calculated by substituting the value of *a* in equation (1) to obtain,

$$sin^2\theta = \frac{\lambda^2}{4}\left[\frac{4}{3}\left(\frac{h^2+hk+k^2}{a^2}\right)+\frac{l^2}{c^2}\right] \quad (3.5)$$

Since, from the Bragg's law:

$$n\lambda = 2d \text{ Sin}\theta \quad (3.6)$$

and with the first-order approximation $n = 1$. For the ⟨002⟩ plane

For the lattice parameters determination for a c-plane oriented sample includes a measurement of d_{001} in order to determine the *c* lattice parameter and for the determination of a lattice from a second measurement of d_{hkl} with either *h* or *k* different from zero [38].

Texture Coefficient

The crystallographic texture in thin films, i.e. the preferred orientation of particular crystal planes relative to the film substrate, is a common and frequently useful phenomenon. Important materials properties, such as polarization, dielectric constant and elastic modulus, are typically anisotropic, and the most effective use of anisotropic materials in thin film applications often involves controlling the texture of the film. The texture coefficient (TC) represents the texture of the particular plane, deviation of which from unity implies the preferred growth [39]. The degree of preferred orientation σ of the sample as a whole can be assessed by estimating the standard deviation of all the $TC_{(hkl)}$ values calculated from the sample

$$\sigma = \sqrt{\frac{\sum_{i=1}^{N}\left(TC_{hkl} - TC_i\right)^2}{N}} \quad (3.7)$$

Where TCi is the texture coefficient of powder sample and its value is always unity. The value of σ is an indicator of the degree of orientation of a sample and can be used to compare different samples. A value of zero for σ indicates that the sample is completely randomly oriented and the sample with a higher value of σ has a preferred orientation [40]. Alternatively, the relative intensity ratio between [002] and [101] planes are can be used to

characterize the orientation of ZNRs. Thus, the degree of c-orientation described by the relative texture coefficient was calculated using the expression [41].

$$TC_{(002)} = I_{002}/(I_{(100)} + I_{(002)} + I_{(101)} + I_{(102)} + I_{(102)} + I_{(102)} + I_{(102)} \quad (3.8)$$

$$TC_{(101)} = I_{101}/(I_{(100)} + I_{(002)} + I_{(101)} + I_{(102)} + I_{(102)} + I_{(102)} + I_{(102)}) \quad (3.9)$$

Where $TC_{(002)}$ is the relative texture coefficient for [002] diffraction plane and $I_{(100)}$, $I_{(002)}$, $I_{(101)}$, $I_{(102)}$, $I_{(110)}$, $I_{(103)}$ and $I_{(112)}$ are the measured diffraction intensities due to [100],[002] ,[101], [102], [110], [103], and [112] planes respectively.

3.2.2 Scanning electron microscope

SEM is a highly important analytical tool used to study the morphology and topography of the solid materials. SEM uses a focused beam of high-energy electrons (typical range from 5 – 35 keV) to generate a variety of signals at the surface of solid specimens. The signals that derive from electron reveal information about the sample including external morphology (texture), diameter, length, thickness, density, shape, chemical composition, crystalline structure and orientation of materials making up the sample.

The beam of electrons in SEM is produced and accelerated from an electron source and passed through a series of condenser and objective lenses, which focus the electron beam. The electron beam is focused vertically toward the specimen by electromagnetic lenses and scanned over a specific area on the specimen surface by the same way as in a Cathode Ray Tube (CRT). Accelerated electrons carry significant amounts of kinetic energy, and this energy is dissipated as a variety of signals produced by electron-sample interactions when the incident electrons are decelerated in the solid sample. These signals include secondary electrons, backscattering electrons, Auger electrons, photons, visible light (cathodoluminescence-CL) and X-Rays. This process is illustrated in Fig. 3.8. Secondary electrons are emitted as a result of energy exchange (inelastic scattering) between the primary electrons and atoms. The energy lost by the primary electron will appear as a gain in secondary electrons with kinetic energy less than 100 eV. The kinetic energy of numerous emitted secondary electrons is varying depending on the atomic structure and its composition. Thus, secondary electrons produce SEM images and are most valuable for showing morphology and topography on the samples. Backscattered electrons are primary electrons that have been reflected from the solid surface by elastic scatterings and are most useful for illustrating contrasts in the composition in multiphase samples [42]. Photons are

characteristic X-rays that are used for elemental analysis and continuum X-ray. The kinetic energy differences of all emitted electrons, either secondary or backscattered, play an important role in the formation of SEM image. A scintillation detector is used to capture the emitted electron and to convert their energy into emission or electric current. Depending on the specimen and the equipment setup, the contrast in the final image provides information on the specimen composition, topography and morphology. The final SEM image is a layout of the energy distribution of the ejected electrons (secondary and backscattered electrons) as a function of their positions. The heavier elements look brighter on SEM image, due to fact that the backscattered coefficient is proportional to the atomic number of the elements [43].

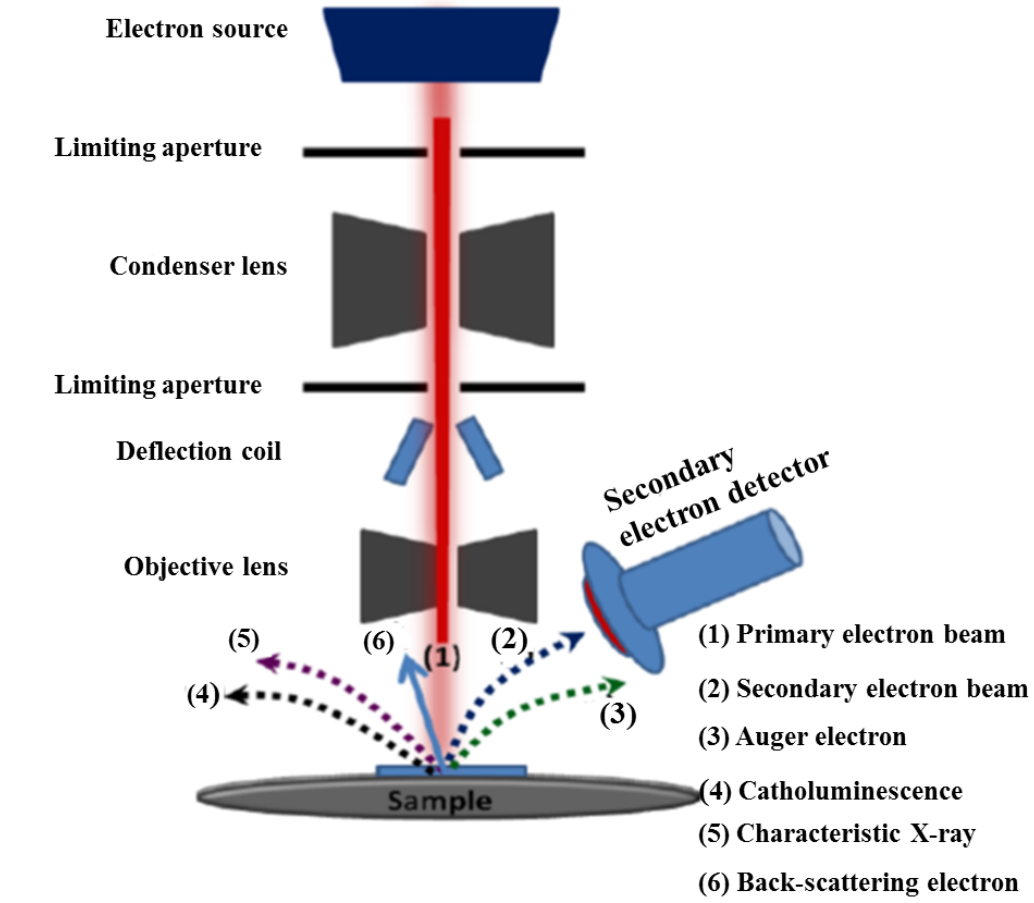

.

Figure 3.8: Schematic diagram of SEM experimental setup and the types emitted electrons and photons due to the electron beam-sample interaction [44].

In this study, a JEOL JSM-7800F SEM Model equipped with Oxford Aztec EDS shown in Fig. 3.9 was used. The SEM image was done with 5 kV electron beam. In most applications, data are collected over a selected area of the surface of the sample, and a 2-dimensional image is generated that displays spatial variations in these properties. Areas ranging from approximately 1 cm to 5 microns in width can be imaged in a scanning mode using conventional SEM techniques (magnification ranging from 20X to approximately

30,000X and the spatial resolution of 50 to 100 nm) [45]. The SEM is routinely used to generate high-resolution images of shapes of objects (SEI) and to show spatial variations in chemical compositions: 1) acquiring elemental maps or spot chemical analyses using EDS, 2) discrimination of phases based on mean atomic number (commonly related to relative density) using BSE, and 3) compositional maps based on differences in trace element "activators" (typically transition metal and Rare Earth elements) using CL [46]. It is also widely used to identify phases based on qualitative chemical analysis and/or crystalline structure. Precise measurement of very small features and objects down to 50 nm in size is also accomplished using the SEM.

Figure 3.9: Schematic diagram of SEM (model JEOL JSM-7800F) equipped with Oxford Aztec EDS at the department of Physics of University of the Free State.

3.2.3 Energy dispersive X-ray spectroscopy

The surface chemical or elemental composition of the synthesized powders grown in this research study was determined by EDS spectroscopy. (EDS or EDX) is a chemical microanalysis technique used in conjunction with SEM. The EDS technique detects X-rays emitted from the sample during the bombardment by an electron beam to characterize the elemental composition of the analysed volume. Features or phases as small as 1 μm or less can be analysed [47].

The information about the chemical composition of the sample is obtained by measuring the intensity distribution and energy of the signal generated by a focussed electron beam impinging on the sample. The source of the electron is the electron gun of a scanning

electron microscope. The incident beam of electrons interacts with core electrons of the sample's atoms transferring sufficient energy to it, thereby ejecting it from the target atom. This results in the creation of a hole within the atom's electronic structure. An electron from an outer, higher energy shell then occupies the hole releasing excess energy in the form of an X-ray photon. As a result of electronic transitions which occur between the outer and inner core levels a characteristic X-ray is emitted when the ionized atom 'relaxes' to a lower energy state by the transition of an outer-shell electron to the vacancy in the core-shell which provides a quantitative and qualitative elemental composition of the sample [49]. Due to a well-defined nature of the various atomic energy levels, it is clear that the energies and associated wavelengths of the set of x-rays will have characteristic values for each of the atomic species present in a sample [13] as shown in Fig. 3.10(a) and (b).

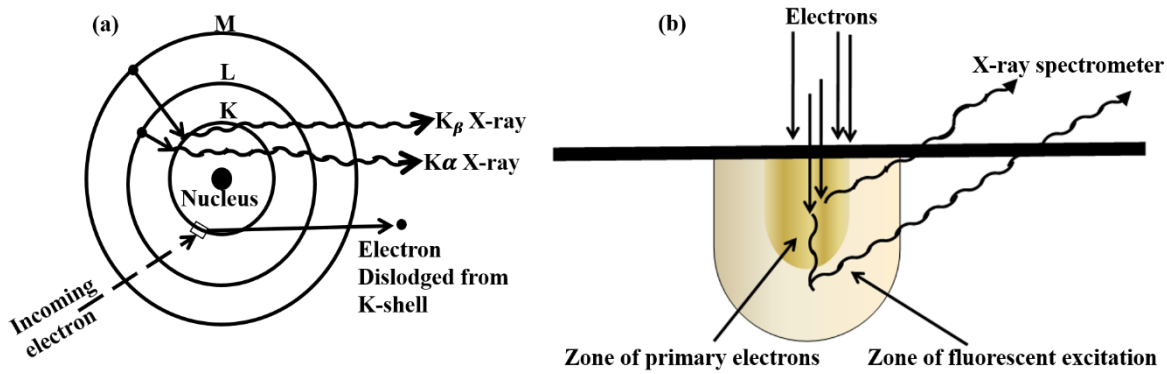

Figure 3.10: (a) and (b) Characteristic x-ray radiation [48].

A characteristic X-ray is usually emitted when the ionized atom 'relaxes' to a lower energy state by the transition of an outer-shell electron to the vacancy in the core shell. The X-ray is called characteristic because its energy equals the energy difference between the two levels involved in the transition and this difference is characteristic of the material.

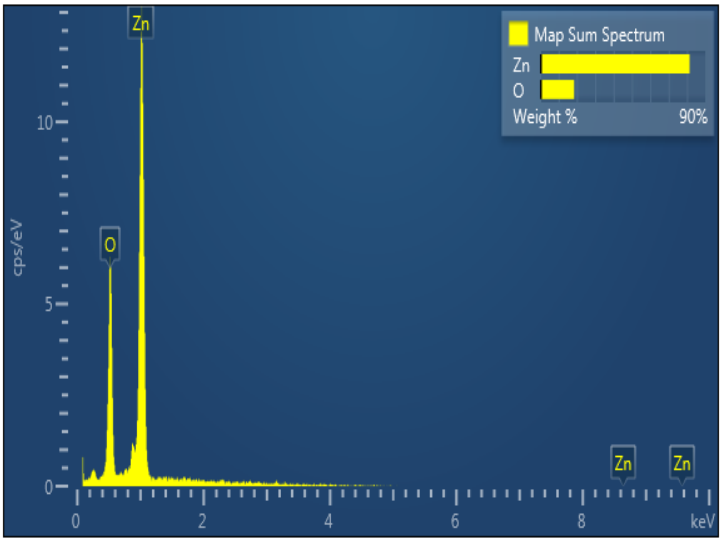

Figure 3.11: Example of an EDS spectrum of ZnO.

From the output of an EDS analysis we obtain an EDS spectrum, see Fig. 3.11. The EDS spectrum shows the frequency in counts of X-rays received for each energy level. The spectrum normally plots the peaks corresponding to the energy levels for which the most X-rays have been received. Each of these peaks corresponds to a specific atom, and therefore characteristic of a specific element. The intensity of a peak in the spectrum correlates with the concentration of the element in the sample [50].

3.2.4 Atomic Force Microscopy

AFM is a high-resolution scanning probe microscopy used to investigate the surface profiles of materials at nanoscale levels and can provide information about their topographic and mechanical properties. The simplest design configuration of the AFM technique is a probe containing a small cantilever with a sharp tip (about 10 nm) at its end that is used to scan the sample surface. The probe is attached to a piezoelectric crystal and positioned vertically above the sample holder (see Fig. 3.12). The piezoelectric crystal is responsible for scanning the tip in a raster pattern over a selected area on the sample surface, by moving the probe toward X, Y or Z directions. When the tip is brought in to the proximity of a sample surface, Van der Waals forces between the tip and the sample's atoms lead to a deflection of the cantilever [51], causing it bend upward or downward.

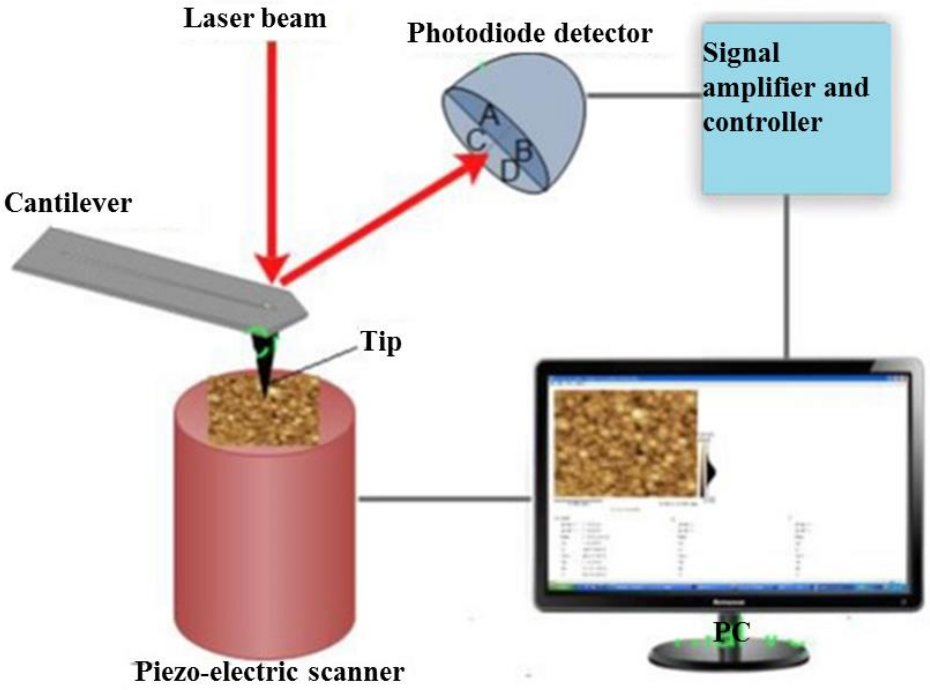

Figure 3.12: Schematic diagram of an AFM system [6].

The deflection of the cantilever, resulting from the changes of the sample's surface topography, is measured by optical lever technique where a beam from a laser diode is focused onto the end of the cantilever and the position of the reflected beam is monitored by a position sensitive photodetector [51]. By measuring the deflection distance [(A+B) – (C+D)], the height between the material and the tip will be calculated. The variation in the height of the tip from the material surface during the scanning process represents the topography information. All physical quantities are fed back to a computer to obtain two and three-dimensional topographical images or other properties of interest.

The AFM technique has three operation modes for imaging: contact mode in which the tip makes a soft physical contact with the sample surface (repulsive force is dominant), non-contact mode in which the tip does not stick to the sample surface (attractive force is dominant) and tapping mode in which short and long-range forces are operating. The use of a particular operation mode is determined according to the sample characteristic as well as the cantilever properties [52]. In this work, the surface topography and roughness were examined from images captured in contact mode using a Shimadzu SPM-9600 AFM (at the University of the Free State, Department of Physics facilities) shown in Fig. 3.13. The root mean square roughness was roughly calculated by analyzing the topography scans of the thin films surface using commercial software that came with the system.

Figure 3.13: Shimadzu SPM-9600 model AFM used during the experiment.

3.2.5 Photoluminescence spectroscopy

PL is a physical process in which several semiconductor materials absorb and then re-radiates photons. Quantum mechanically, this can be described as an excitation of an electron to a higher energy state and then a return to a lower energy state accompanied by the emission of the photon as illustrated in Fig. 3.14.

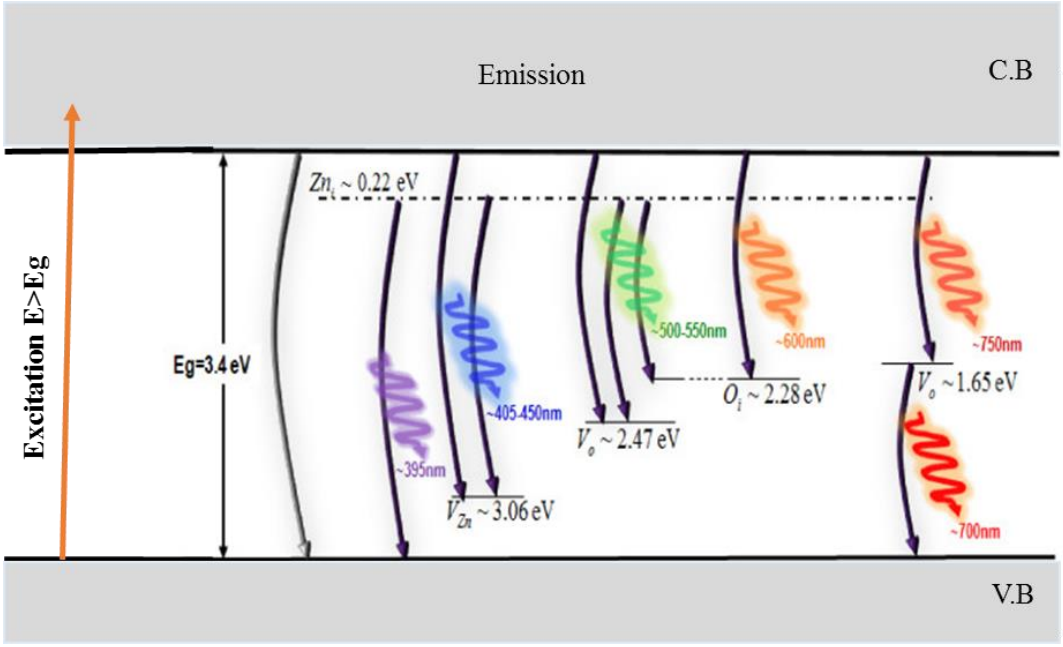

Figure 3.14: Excitation and Emission processes in ZnO material

The PL technique is a powerful and a relatively simple method, extensively used for characterization in semiconductor physics for a number of reasons It is non-destructive because it is based on pure optical processes, no sample preparation is required and it is highly sensitive. Different types of samples (powder, liquid or bulk semiconducting material) can be characterized. However, since PL relies on radiative recombination, it is very difficult for the investigation of non-radiative processes and it is not suitable for characterization of samples of poor quality [53].

The operation of PL measurement can be described in few steps as shown in Fig. 3.15. Firstly, the sample is optically excited with a laser beam or UV light with energy greater than its band gap. The incident photons are absorbed under creation of the electron-hole pairs in the sample. As a result, the electron from the ground state (valence band) will be elevated to the conduction band through a process of photo-excitation. Secondly, after a short time, the electrons drop down to recombine with the holes at its initial state or to any luminescent centre from which the electron has excited. The imparted energy, is thus, dissipated by the sample through the emission of light (radiative transition), or thermally (non-radiative transition). In the case of photo-excitation, this luminescence is called photoluminescence. Thirdly, the emitted light is observed and disseminated by a double grating monochromator and photomultiplier detectors. The energy of the emitted photon is associated with the difference in the energy levels of the electrons and the hole that was involved in specific transition process between excitation and equilibrium state. Finally, the luminescence is collected, and intensity of emitted photons recorded as a function of the energy or wavelength, to produce a PL spectrum.

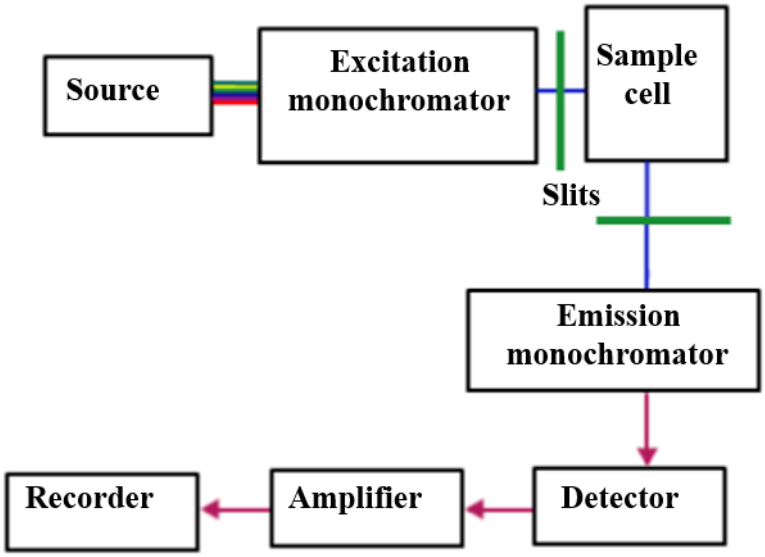

Figure 3.15: Schematic diagram of the principle of fluorescence spectrometer.

PL is used to obtain information on the electronic structure and determine the extrinsic and intrinsic properties of the semiconductor. The materials that can be deduced from the PL study include the size of the band gap, recombination mechanism, surface properties as well as the density of states and excitonic states. It is particularly suited for the detection of shallow-level impurities, but can also be applied to certain deep-level impurities/defects, provided that their recombination is radiative [54]. To gain more knowledge about the electronic structure, magnetic and electric fields can be applied in a controlled manner. Moreover, external forces can be used in PL investigations, e.g. the strain by exposing the material to mechanical pressure.

In the present work, the PL data was collected using the Cary Eclipse Spectrophotometer (Fig. 3.16). The Cary Eclipse Spectrophotometer (add schematic of PL system) uses a Xenon flash lamp (60-75W) for superior sensitivity, high signal-to-noise and fast kinetics. It measures the Emission of light from samples in four modes. Using Xenon Lamp technology, it captures a data point in every 12.5 ms and scans at 24 000 nm/min without peak shifts. The Cary Eclipse is the only spectrophotometer with room light immunity.

Figure 3.16: Cary Eclipse Fluorescence Spectrophotometer model LS-55 at the University of the Free State, Physics Dpt.

3.2.6 Catholuminescence spectroscopy

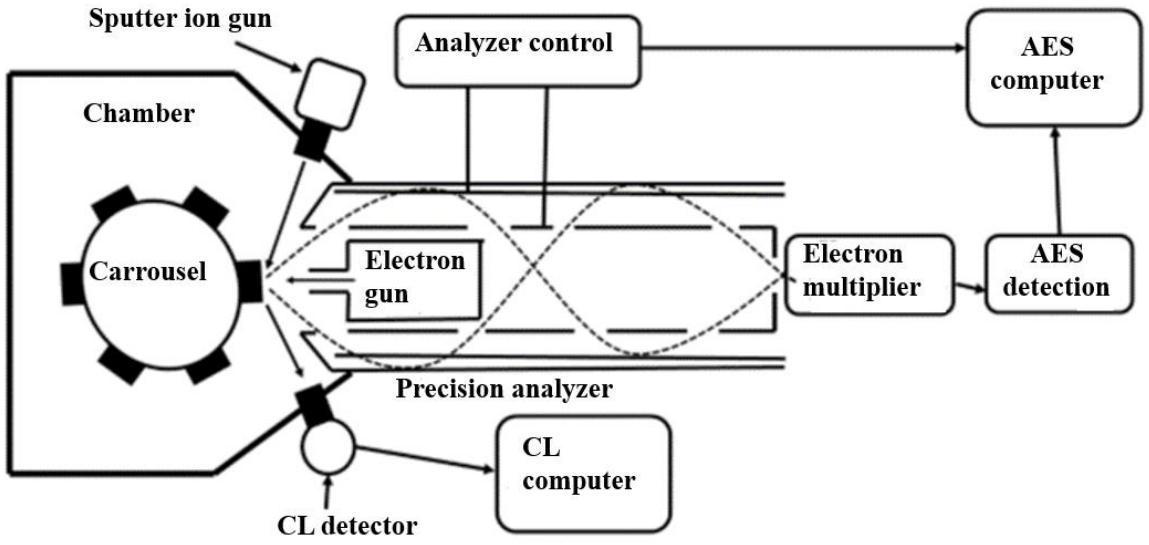

Figure 3.17: Schematic diagram of AES and CL system [6].

CL is a non-destructive analytical technique that is widely used in scientific laboratories to investigate the luminescent properties of materials such as phosphors, semiconductors, dielectric and ceramic materials. CL refers to the emission of light by the substance when excited by energetic electrons, where the cathode is the electrons source. Essentially, the CL technique is similar to the PL in working principle; the difference is in their excitation sources and energy. Fig. 3.17 shows a diagrammatic expression of the AES vacuum system coupled with a CL spectrometer.

A major breakthrough in cathodoluminescence instrumentation came with the development of CL detectors that could be attached to a scanning electron microscope (SEM). Because of its high magnification capability and the capability of combining CL and SEM observations (e.g., backscattered and secondary imaging), SEM–CL is rapidly becoming the technique of choice for high-resolution CL imaging [55].

The CL is generated alongside other emissions such as secondary electrons, backscattered electrons, X-rays, and photons when a specimen on the stage of SEM microscope is bombarded with a beam of high-energy electrons [56]. This is followed by absorption of energy of the primary electron by the atoms of the specimen which causes an electron to be promoted from the ground state to the excited state leading to the formation of electron-hole pairs. When the electron falls back to its ground state (direct band to band recombination) or other luminescent centres (structural defects), the absorbed energy will be released in form of photons (cathodoluminescence) emissions. The value of the photon

energy is determined by the luminescent centre where the promoted electron fell back to. A CL detector attached to the SEM is used to obtain CL spectra. In the present studies, the CL detector was attached to JSM-7800F field emission SEM equipment shown in Fig. 3.9.

3.2.7 UV-Visible Spectroscopy

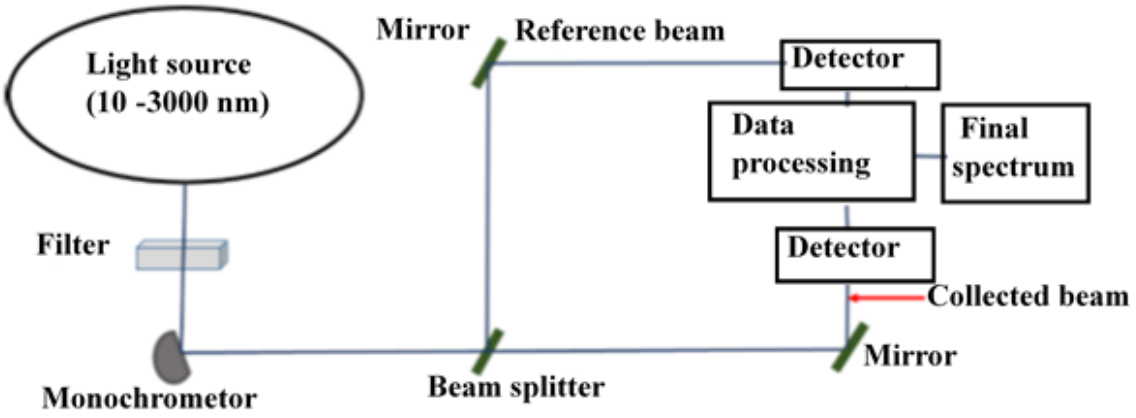

Figure 3.18: Schematic diagram of a double-beam UV-Vis basic working principle [6].

The UV-Vis spectrophotometer is an optical technique used to study the absorption and reflection properties of a material which involves the measurement of the attenuation of a beam of light after it passes through a sample or after reflection from a sample surface. It utilizes a light in the ultraviolet (UV) region and visible region of the electromagnetic spectrum to determine the absorption properties. A deuterium lamp is used to produce light with the wavelength ranging from 10 nm to 330 nm, and a tungsten lamp for the light with the wavelength range from 300 nm to greater than 3000 nm.

The working principle of the UV-Vis spectrophotometer, Fig. 3.18, is based on the light absorption by the examined material, which can be performed in two modes: reflectance and transmittance. When light with a certain wavelength is incident on the material surface, it can be absorbed, reflected, transmitted or partly absorbed. In the UV-Vis measurement, a light from the source is split into two beams; one directed to the detector as a reference and the other directed to the sample. Part of the incident light on the sample will be absorbed and the other part will be diffused and reflected. As the sample is positioned in an integrating sphere, the diffused-reflected and scattered light will be collected and sent to the detector. The reflected light will be subtracted from the reference light resulting in the amount of absorbed light by the material. Absorption of radiation by a sample is measured at various wavelengths and plotted by a recorder to give the spectrum which is a plot of the

wavelength of the entire region selected versus the absorption (A) of light at each wavelength.

Figure 3.19: Perkin Elmer lamb 950 UV-VIS Spectrophotometer at the University of the Free State, Physics Department.

Basically, the absorption/reflection spectrum provides information about the materials ability to absorb and reflect light. The band gap of the sample can be obtained from the UV-Vis data by extrapolating the straight line portion of $(\alpha hv)^2$ to $(\alpha hv)^2 = 0$ of Tauc's plot [57]. The UV-Vis system, shown in Fig. 3.19, was used in this research.

References

[1] M. Ohyama, H. Kozuka, T. Yoko, Thin Solid Films 306 (1997) 78-85,

[2] B. Weintraub, Z. Zhou, Y. Li, Y. Deng, Nanoscale 2, (2010) 1573-1587.

[3] W. L. Suchanek, J. Cryst. Growth 312, (2009) 100–108.

[4] O. D. Jayakumar, H. G. Salunke, R. M. Kadam, M. Mohapatra, G. Yaswant, S. K. Kulshreshtha, Nanotechnology 17, (2006) 1278–1285.

[5] Rizwan Wahab, S. G. Ansari, Young-Soon Kim, Hyung-Kee Seo, Hyung-Shik Shin, Appl.Surf. Sci., 253 (2007) 622–7626.

[6] Emad Hasabeldaim Hadi Hasabeldaim, Surface characterization and cathodoluminescence degradation of ZnO powder and thin films, MSc Thesis, University of the Free State, 2016.

[7] J. George, Preparation of Thin Films, Marcel Dekker, Inc., New York, (1992).

[8] Y. R. Toda, K. S. Chaudhari, A. B. Jain, D. N. Gujarathi, Asian J. Chem. and Envi. Res., 4(1), (2011) 40-43.

[9] H. M. Pathan, C. D. Lokhande, Bulletin of Materials Science 27(2), (2004) 85-111.

[10] G. H. Fekadu, Synthesis and characterization of cadmium selenide (Cdse) and lead sulphur selenide (Pbs1-Xsex) thin films by chemical bath deposition method, Doctoral dissertation, Kwame Nkrumah University of Science and Technology, 2015.

[11] M. A. Verges, A. Mifsud, C. J. Serna, J. Chem. Soc. 86, (1990) 959-963,

[12] X. J. Feng, L. Feng, M. H. Jin, J. Zhai, L. Jiang, J. Am. Chem. Soc. 126, (2004) 62-63.

[13] Q. C. Li, V. Kumar, Y. Li, H. T. Zhang, T. J. Mark, R. P. H. Chang, Chem. Mater. 17, (2005) 1001.

[14] X. D. Gao, X. M. Li, W. D. Yu, J. Phys. Chem. B 109, (2005) 1155-1161,

[15] L. Yu, G. M. Zhang, S. Q. Li, Z. H. Xi, D. Z. Guo, J. Cryst. Growth 299, (2007) 184-188,

[16] L. Vayssieres, K. Keis, A. Hagfeldt, S. E. Lindquist, Chemistry of Materials 13(12), (2001) 4395-4398.

[17] D. S. Boyle, A. Bayer, M. R. Heinrich, O. Robbe, P. O'Brien, Thin Solid Films 361, (2000) 150-154.

[18] A. A. -C. Reádigos, V. M. García, O. Gomezdaza, J. Campos, M. T. S. Nair, P. K. Nair, Semicond. Sci. Technol. 15(11), (2000) 1022-1029.

[19] H. M. Pathan, C. D. Lokhande, Bulletin of Materials Science 27(2), (2004) 85-111.

[20] S. R. Das, K. L. Chopra, Thin film Solar Cells, Plenum Press, New York, ISBN-10: 0306411415, 1983.

[21] D. J. Pietrzyk, C. W. Frank, Analytical Chemistry: An Introduction, Academic Press, New York, 1974.

[22] D. A. Skoog, D. M. West, Fundamentals of Analytical Chemistry, 2nd Ed., Holt, Rinehart and Winston, New York, 1980.

[23] G. K. Padam, S. K. Gupta, Appl. Phys. Lett. 53, (1988) 865-867,

[24] E. J. H. Lee, C. Ribeiro, E. Longo, Edson R. Leite, J. Phys. Chem. B 109, (2005) 20842-20846,

[25] C. Pacholski, A. Kornowski, H. Weller, Angew. Chem. Int. Ed. 41, (2002) 1188-1191.

[26] B. Weintraub, Z. Zhou, Y. Li, Y. Deng, Nanoscale 2, (2010) 1573-1587,

[27] H. K. Lee, M. S. Kim, J. S. Yu, Nanotechnology 22, (2011) 445602,

[28] J. Song, S. Lim, J. Phys. Chem. *C*, 111, (2007) 596-600,

[29] H. G. Fekadu, F. K. Ampong, T. Abza, I. Nkrumah, R. K. Nkum, F. Boakye, Elixir Thin Film Tech. 76, (2014) 28432-28437.

[30] G. Hodes, Chemical solution deposition of semiconductor films, Marcel Dekker, Inc., New York, ISBN 0-8247-0851-2, 2002.

[31] S. M. H. Al-Jawad, F. H. Alioy, Eng. & Tech. Journal 31(4), (2013) 505-519.

[32] P. P. Hankare, S. D. Delekar, M. R. Asabe, P. A. Chate, V. M. Bhuse, A. S. Khomane, B. D. Sarwade, Journal of Physics and Chemistry of Solids 67(12), (2006) 2506-2511.

[33] R. S. Mane, C. D. Lokhande, Materials Chemistry and Physics 65(1), (2000) 1-31.

[34] O. P. Moreno, G. A. Avila, J. R. Cerna, J. H. Tecorralco, M. C. Portillo, J. M. Juárez, O. Z. Ángel, Journal of Materials Science and Engineering A *1*, (2011) 692-704.

[35] Wagner R S and Doherty C, J. Electroceram. Soc. 113**,** (1996) 1300 3 4596,

[36] A. R. Bushroa, R. G. Rahbari, H. H. Masjuki, M. R. Muhamad, Vacuum 86(8), (2012) 1107-1112.

[37] B. D. Cullity, S. R. Stock Elements of X-ray Diffraction, 3rd edn Prentice Hall. New York, 2001.

[38] V. Darakchieva, Strain-related structural and vibrational properties of group-III nitride layers and superlattices, Doctoral dissertation, Linkoping studies in science and technology, 2004.

[39] S. Ilican, M. Caglar, Y. Caglar, Materials Science-Poland 25(3), (2007) 709-718.

[40] S. Gupta, K. Munirathnam, Indian Journal of pure and Applied Physics 52, (2014) 44-52.

[41] D. I. Rusu, G. G. Rusu, D. Luca, Acta Physica Polonica A., 119 (6) (2011).

[42] P. W. Hawkes J. C. H. Spence, Science of Microscopy, New York, USA: Springer, vol. 1, 2007.

[43] R. F. Egerton, physical principle of electronic microscopy: An introduction to TEM, SEM and AEM, Springer, New York, pp. 016502, 2008.

[44] S. T. S. Dlamini, Characterization of Y3 (Al, Ga) 5O12: Ce^{3+} phosphor thin films prepared by pulsed laser deposition, University of the Free State, Doctoral dissertation, 2013.

[45] http://en.wikipedia.org/wiki/Scanning_electron_microscope [Accessed 12/12/2017].

[46] P. R. Berman, advances in atomic, molecular and optical physics, Academic press, Amsterdam, Vol.45, 1997.

[47] Description of EDS Technique http://mee-inc.com/index.html [Accessed 03/10/2017].

[48] Energy Dispersive X-ray Spectroscopy (EDS/EDX), [online]. Available from http://www.thermo.com/com/cda/technology/detail/1,,12700,00.html[Accessed 01/12/ 2017].

[49] B. G. Yacobi, L. L. Kazmerski, D. B. Holt, (Eds.*)* Microanalysis of solids. Springer Science & Business Media, (2013).

[50] EDS online Available from http://ion.eas.asu.edu/descript_eds.htm [Accessed 17 Dec 2017].

[51] A. Y. M. Ahmed, Luminescence properties of $Y_{3(}AlGa)_5)_{12}$: Tb thin films, PhD Thesis, University of the Free State, 2014.

[52] A. Vilalta-Clemente, K. Gloystein, Principles of Atomic Principles Force Microscopy (AFM), Physics of Advanced Materials Winter School, Aristotle University of Thessaloniki, 2008.

[53] Photoluminescence [0nline], Available from http://www.purdue.edu/REM/rs/sem.htm [Accessed 08/08/2017].

[54] Q. Nguyen, the optically detected magnetic resonance studies of intrinsic defects in dilute, PhD thesis, Linköping University Dissertation No.901, 2004.

[55] R. F. Egerton, Physical principles of electron microscopy, New York: Springer, p. 41, 2005.

[56] E. Coetsee, PhD Thesis, University of the Free State, 2010.

[57] J. Tauc, R. Grigorovichi, A. Vancu A, Phys. Status Solidi 15 (1966) 627**.**

Chapter 4

Band gap engineering, enhanced morphology and photoluminescence of un-doped, Ga and/or Al-doped ZnO nanoparticles by reflux precipitation method

4.1 Introduction

ZnO TCO has emerged as the most attractive alternative to the most popular indium-doped tin oxide (ITO) owing to its low cost, nontoxicity, suitability for deposition of film, large band gap energy (~3.37 eV) as compared to high level of toxicity, high cost, low stability and material scarcity of ITO [1]. Additionally, elements of Group III such as boron, aluminium, gallium and indium have been doped into ZnO to generate extra electrons so as to enhance its conductivity, crystallinity and optical transmittance [2, 3]. To this end, aluminium-doped zinc oxide (AZO) and gallium-doped zinc oxide (GZO) nanostructures in a ZnO series have been researched on widely because of their noble electrical and optical properties. For instance, Al doping produces material with high conductivity and thermal/chemical stability [4-5], high transparency and low resistivity [6] while Ga-doped ZnO is more stable and has greater resistance to oxidation and low reactivity when compared with other impurities [7, 8]. And Ga ionic radius and covalent radius are nearly equal to that of Zn [9]. Besides, the conductivity of GZO films is reported to be approaching that of ITO. Gallium and aluminium co-doped ZnO (GAZO) materials [10] have also been advanced since they are expected to possess the material strengths of both GZO and AZO nanostructures.

As far as the study on Ga and /or Al-doped ZnO nanostructures is concerned, the available literature majorly deals with the effects of different growth and post-growth parameters on various properties of Al/Ga-doped and co-doped ZnO thin films. For instance, Lin et al. [11] in their study on the comparison of AZO, GZO, and AGZO thin films using pulsed direct current magnetron sputtering, investigated the electrical properties,

transmittance, effects of texturing, and applicability as the front contact for a-Si:H solar cells. They found that AZO and GZO films have better electrical properties than AGZO film; While, Ebrahimifard et al. [12] who made a comparison of transparent conductive Al or Ga single doped ZnO thin films with Al and Ga co-doped ZnO demonstrated the capability of co-doped samples in the optoelectronic industry. Similarly, Seo et al. [13] in their work investigated the dependencies of the electrical, optical, structural, and morphological properties on the thickness of the AGZO films grown by an LFTS system using co-sputtering. They reported optimal material properties of AGZO thickness at 200 nm. However, there are very few reports on the Ga/Al-doped and co-doped ZnO nanoparticles (NPs). Yet, the characteristics of the nanopowders or NPs have considerable influences on producing high-quality thin films [14]. For example, a fundamental way to enhance the quality of the transparent conducting oxide (TCO) electrode layer, an integral part in the structure of thin film solar cells [15], is by improving the seed layer component. It was reported; seeding of the glass substrate with nanoparticles ensures uniformity of ZnO nanorods (NRs) and improves optical properties by providing nucleation sites which lowers thermodynamic barriers [16]. This implies that any factor that will improve the seed layer will improve not only the property of the TCO film but also, the properties of nanostructures grown on the film.

It is for this reason that this study aims to compare the material properties of Ga and Al-doped and co-doped ZnO NPs along with un-doped ZnO counterpart with the view to identify the seeding material with the desired properties for the fabrication of impurity-doped ZnO transparent electrode thin film for subsequent growth of well-aligned ZnO NRs to form a photoanode of the dye-sensitized solar cell.

We believe, the present study advances the understanding of the effects of Ga/Al single doping and co-doping on the structural, luminescence and optical of the ZnO NPs as it goes further to compare the results with the un-doped ZnO NPs. Moreover, the reflux precipitation synthetic method used in this experiment is less reported on to synthesize Ga/Al-doped and co-doped ZnO NPs. Achamma and Shajeem [17] found some defect emission from their Ga-doped ZnO NPs prepared by the hydrolysis technique. The obtained PL was, however, of poor quality. Different authors have also reported the synthesis of Ga doped ZnO [12, 18]. In all these reports, other than us the synthesis was performed via time consuming, expensive procedures and mostly on thin films. Liu et al [18] obtained PL spectra of GZO films which showed near band edge (NBE) emission and broad orange deep-level emission. The NBE emission shifted to a higher energy region and the intensity

decreased with the increase of Ga concentration. The blue shift of the NBE emission results from the Burstein-Moss effect. The quenching of the NBE emission was ascribed to the non-radiative recombination. The orange emission is related to the oxygen vacancies. Interesting in our results was the decrease in the orange/green defect emission and an increase in the emission in the blue part of the spectrum, which was different from previous studies. Our results showed that GZO NPs had superior structural and optical properties to ZnO, AZO and GAZO NPs and thus would be useful for seeding on the glass substrate to produce a transparent conducting oxide film.

4.2 Experimental Procedure

The chemical reagents sodium hydroxide (NaOH), zinc nitrate ($Zn(NO_3)_{2)}$ and gallium nitrate hexahydrate ($Ga(NO_3)_3.6H_2O$) were of analytical grade and as such used without purification. ZnO, AZO, GAZO and GZO NPs were synthesized by reflux precipitation method.

In order to dope Ga and/or Al in the ZnO host material, $Zn(NO_3)_2.6H_2O$ was mixed with $Ga(NO_3)_3$ and/or $Al(NO_3)_3$ dopants precursors and dissolved in ethanol solvent. The total doping amount was maintained at 2 mol% ratio of doping(s) per Zn precursor solution (i.e. $Al/Zn = Al + Ga/Zn = Ga/Zn = 2$ mol% ratio) and the contents of the Al and Ga, in the case of co-doped samples, were varied between 0 and 2 mol. %. Thus, the resultant impurity-doped and co-doped ZnO NPs were: AZO (2 mol% Al), GAZO (1:1 mol% Ga/Al), GAZO (1.5:0.5 mol% Ga/Al), GAZO (1.7:0.3 mol% Ga/Al), GAZO (1.9:0.1 mol% Ga/Al) and GZO (2 mol% Ga). The 2 mol% doping level has been used due to the previous experimental best results obtained at this doping level. Ammonia (NH_3) in an aqueous solution was used as a complexing agent and was added dropwise to the mixture of $Zn(NO_3)_2$ and $Ga(NO_3)_3/Al(NO_3)_3$ or co-doping mixture of $Zn(NO_3)_2$, $Ga(NO_3)_3$, and $Al(NO_3)_3$ solution, and pH values of the Zn/Ga or Zn/Al or Zn/Ga/Al precursor solution was adjusted to 5 pH by using a Hanna pH 211 pH meter. Zn/Ga precursor sol. pH of 5 was determined to produce GZO NPs with suitable luminescence, structural and optical properties in our previous experiment. 100 mg PVP was added as a surfactant to reduce agglomeration of the NPs during the growth. In the three-neck glass flask, 0.2 M Zn/Ga or Zn/Al or Zn/Ga/Al precursor sol. was heated to 70 °C growth temperature while stirring. To this, 0.8 M solution of NaOH was added dropwise for 60 minutes while refluxing and stirring continuously. The formed mixture was kept stirred for two hours at the same

growth temperature and allowed to stand for some time for precipitation to form. The material was then filtered and washed several times with deionized water. The washed sample was dried at 60 °C in an oven for one hour and collected for package. The same method was followed to prepare un-doped ZnO NPs from aqueous solutions of 0.8 M NaOH and 0.2 M $Zn(NO_3)_2$. The Zn precursor solution was earlier adjusted to 5pH and PVP added as required.

The as-grown nanoparticles were subjected to XRD analysis (XRD, Advanced D8 Bruker powder diffractometer), with a Cu anode X-ray tube (with a K radiation wavelength of 1.54 Å), to study their crystal structure. The study of surface morphology and elemental composition, as well as the CL of the samples, were done using a Jeol JSM-7800F Field Emission equipped with Oxford Aztec EDS. The PL data was measured using a fluorescence spectrophotometer (Cary Eclipse model LS-55). The optical reflectance spectra and were collected using a UV-Vis spectrophotometer (Perkin Elmer Lambda 950). All measurements were conducted at room temperature.

4.3 Results and Discussion

4.3.1 XRD analysis

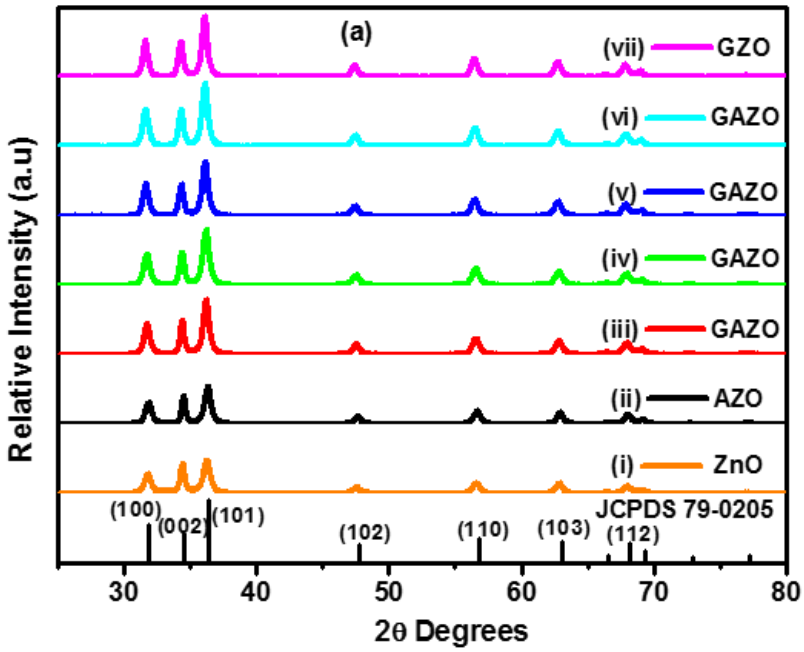

Figure 4.1: (a) XRD patterns of (i) ZnO, (ii) AZO (2 mol% Al), (iii) GAZO (1:1 mol% Ga/Al), (iv) GAZO (1.5:0.5 mol% Ga/Al), (v) GAZO (1.7:0.3 mol% Ga/Al), (vi) GAZO (1.9:0.1 mol% Ga/Al) and (vii) GZO (2 mol% Ga) nanoparticles.

The XRD patterns of the ZnO, AZO, GAZO and GZO NPs are shown in Fig. 4.1(a). All of the samples were polycrystalline and display a hexagonal wurtzite crystal structure of ZnO [19], which matches well with space group P63mc (No. 186) (JCPDS database pdf No. 79–0205). Cell parameters: a = 3.264 and c = 5.219. The XRD spectra depict the diffraction peaks of ZnO only. No trace of other diffraction peaks such as Zn_1-xGa_xO_4 and Ga_2O_3 indicating an effective doping as the Al/Ga took place of Zn or located in the interstitial sites in the ZnO lattices or segregated into the noncrystalline region in the grain boundaries while conserving the original ZnO lattice structure [20]. The mean crystallite sizes were calculated using the [002,100–103,110] and [112] diffraction planes of XRD spectra by Scherrer's formula [21] and found to be 16.5, 18, 18.5 and 19 nm for ZnO, AZO, GAZO(1:1 Ga/Al) and GZO NPs respectively. The crystallite size values increased slightly with the increase in Ga content in the samples due to the fact that Ga^{3+} which has the bigger ionic radius (0.62 Å) than Al (0.53 Å), substitute for the Zn^{2+} site in ZnO host lattice resulting in a bigger volume of the unit cell of ZnO. Besides that, Ga–O with longer covalent bond length (1.92 Å) is thought to cause an increase in the volume of unit cell as compared to the bond length of Al-O (1.8 Å) [22]. Additionally, it was reported that increasing the content of Al in the lattice of ZnO decreases the crystallite size, as stated earlier, which results in more grain boundaries leading to higher electron scattering [7], and therefore affecting the crystallinity and optical properties of the samples.

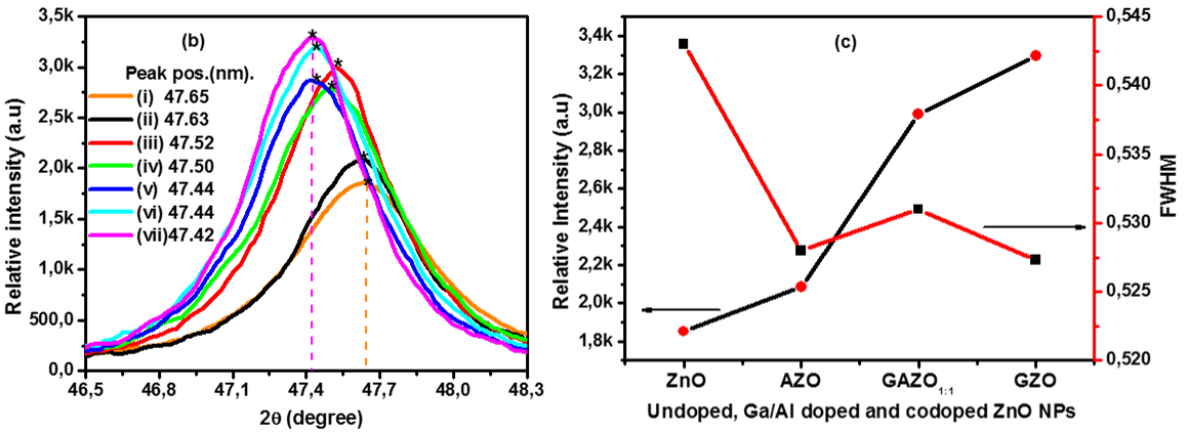

Figure 4.1: (b) An enlarged image of diffraction plane [102] for (i) ZnO, (ii) AZO (2 mol% Al), (iii) GAZO (1:1 mol% Ga/Al), (iv) GAZO (1.5:0.5 mol% Ga/Al), (v) GAZO (1.7:0.3 mol% Ga/Al), (vi) GAZO (1.9:0.1 mol% Ga/Al) and (vii) GZO (2 mol% Ga) NPs. **(c)** Rel. intensity and the FWHM of [102] diffraction peaks for undoped, Ga/Al-doped and co-doped ZnO NPs.

Fig. 4.1(b) shows the variation in diffraction peak [102] intensity, peak width and position of the ZnO, AZO, GZO and GAZO NPs at different Ga/Al % doping levels. As

illustrated in Fig. 4.1(c) the peak intensity increased while the FWHM became narrower, insinuating improvement in crystallinity, as the Ga doping levels increased. This implies that Al doping increament deteriorates the crystallinity of the NPs, as a result of lattice distortion in ZnO NPs due to stress caused by the smaller radius of Al^{3+} (0.054 nm) compared to Zn^{2+} ions (0.074 nm) [23]. Ebrahimifard et al. [12] reported that the higher Madelung energy and solubility limit in case of the Ga cause slightly higher crystallinity in GZO samples compared to AZO samples.

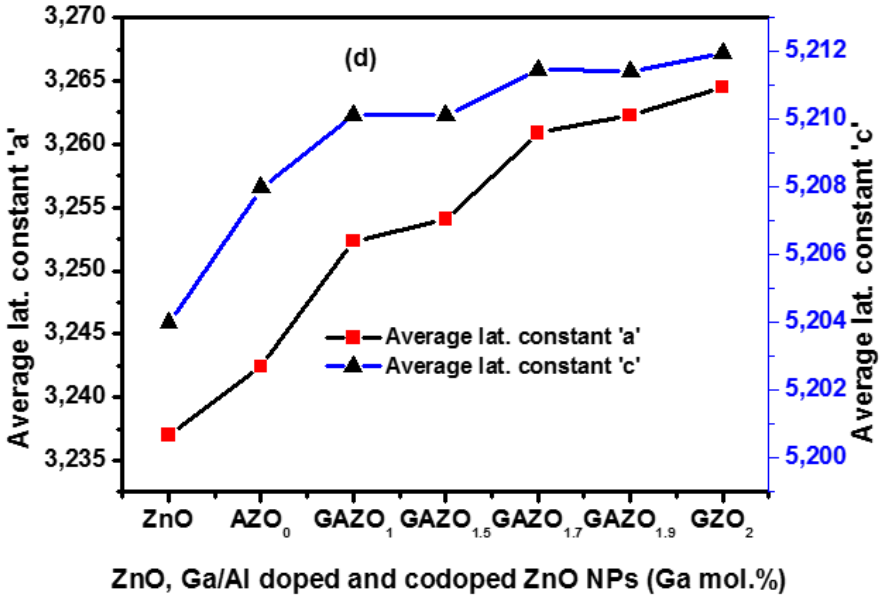

Fig. 4.1: (d) Graph of lattice constants 'a' and 'c' of ZnO, Ga and / or Al doped ZnO NPs for varied Ga content (0-2 mol%) in the dopant ratios.

The deviation in [102] plane diffraction peak position, in the 2θ region from 47.65° to 47.42°, was analyzed in Fig. 4.1(b). The approximately linear deviation toward the lower angle of diffraction with the increase in mol% Ga was occasioned by a change in stress in the NPs [24]. The observed shift can be attributed to the increase of lattice constants that come from the substitution of more Ga^{3+} ions on the Zn^{2+} sites or the presence of interstitial Ga atoms that occupy the ZnO lattice and the larger ionic radius of Ga ions. This is in agreement with the Bragg law, which states that decrease in the Bragg angle $2\boldsymbol{\theta}$ reveals the increase in interplanar spacing. The average lattice parameters 'a' and 'c' of the samples for [002,100–103,110] and [112] diffraction planes were estimated from the relation [25], and the results outlined in Fig 4.1.(d). The average lattice constants 'a' and 'c' were calculated as a = 3.263 and c = 5.208 Å respectively, showing an increase in trend with the increase in mol% Ga. These values are in close range to the bulk ZnO lattice constants shown in the JCPDS card result,i.e., a = 3.264 and c = 5.219 Å. The slight deviation of the observed

lattice parameters could be due to the substitution of Ga and/ or Al ions and the presence of intrinsic point defects like zinc antisites, oxygen vacancies, and extended defects.

4.3.2 SEM and EDS analysis

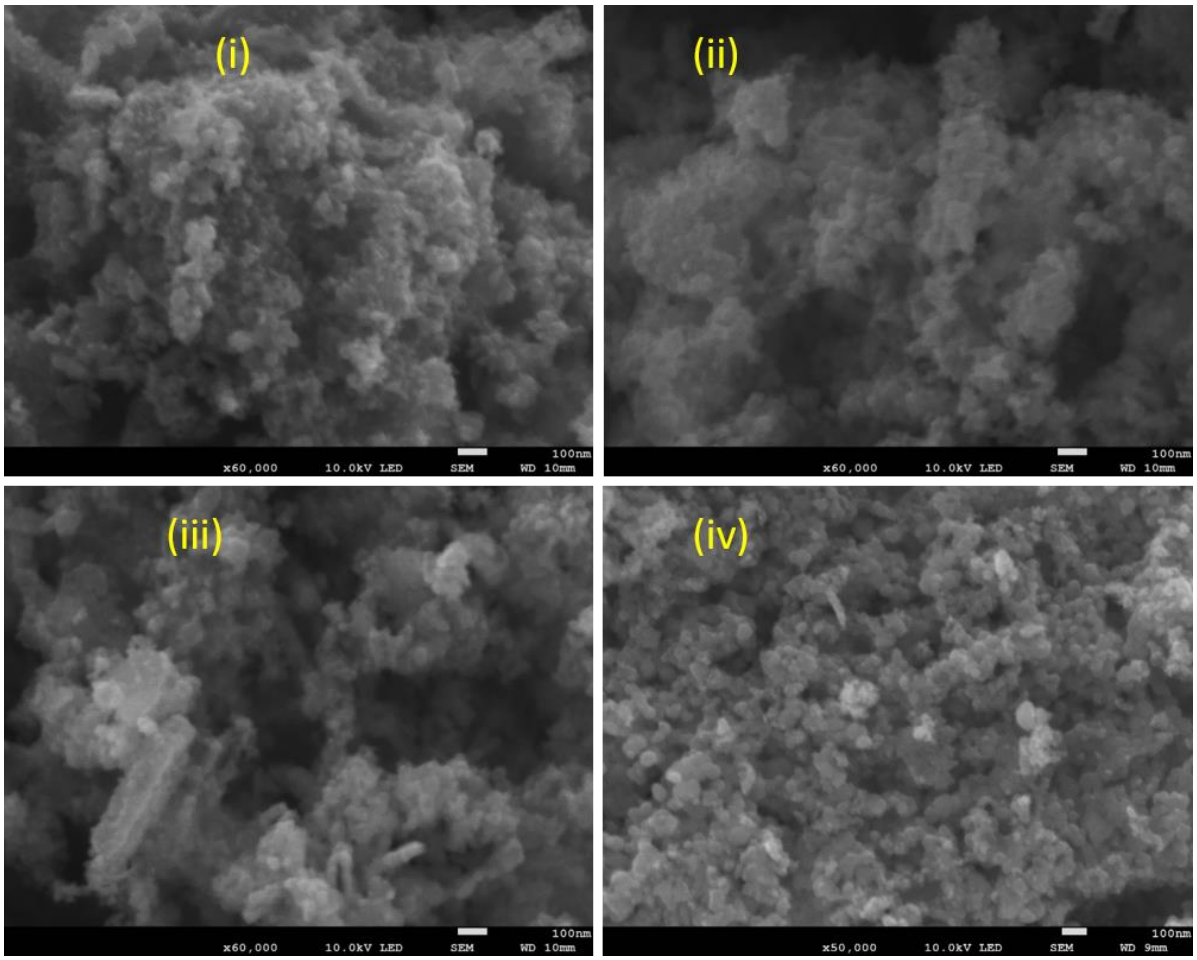

Figure 4.2: (a) SEM micrographs of (i) ZnO, (ii) AZO (2 mol% Al), (iii) GAZO (1:1 mol% Ga/Al) and (iv) GZO (2 mol% Ga) NPs.

The SEM images in Fig. 4.2(i-iv) compare the changes in morphologies of ZnO, GZO, AZO and GAZO NPs with the doping and co-doping ratios. The morphology was observed to improve with the increase in Ga doping levels in the sample as more regular and dispersed particles are formed. Un-doped ZnO sample showed the most agglomerated NPs. The GZO NPs have homogenous denser structure compared with the AZO NPs, the former consist of larger, spherical and uniformly spread NPs. The dense structure of the conducting layer is favorable for easy transport of the charge carriers. The homogeneity of GZO NPs could be due to the fact that the solid solution of Ga/Zn is known to be more stable than Al/Zn solid-solution owing to the smaller distortion of the crystal structure in the case of Ga doping. It

could be seen that the particle sizes of SEM images decrease with the decrease of the mount of Ga in the sample or rather with the increase in Al dopant content from 0.5 to 2.0 mol% in consistency with the crystallite size values calculated by Scherrer's formula. The decrease in size could be as a result of the combined effects of the increased incidents of nucleation centers induced by dopants and the growth stress disturbance occasioned by the difference in ionic radius between zinc and dopant atom [26]. The increase in number of nucleation resulted in development of small grains as dopant is incorporated into the host material; whereas, the larger growth stress disturbance was due to the bigger difference in radius between Zn^{2+} (0.074 nm) and Al^{3+} (0.054 nm) [27] as compared to the lesser ionic difference between Ga^{3+} (0.062 nm) and Zn^{2+}.

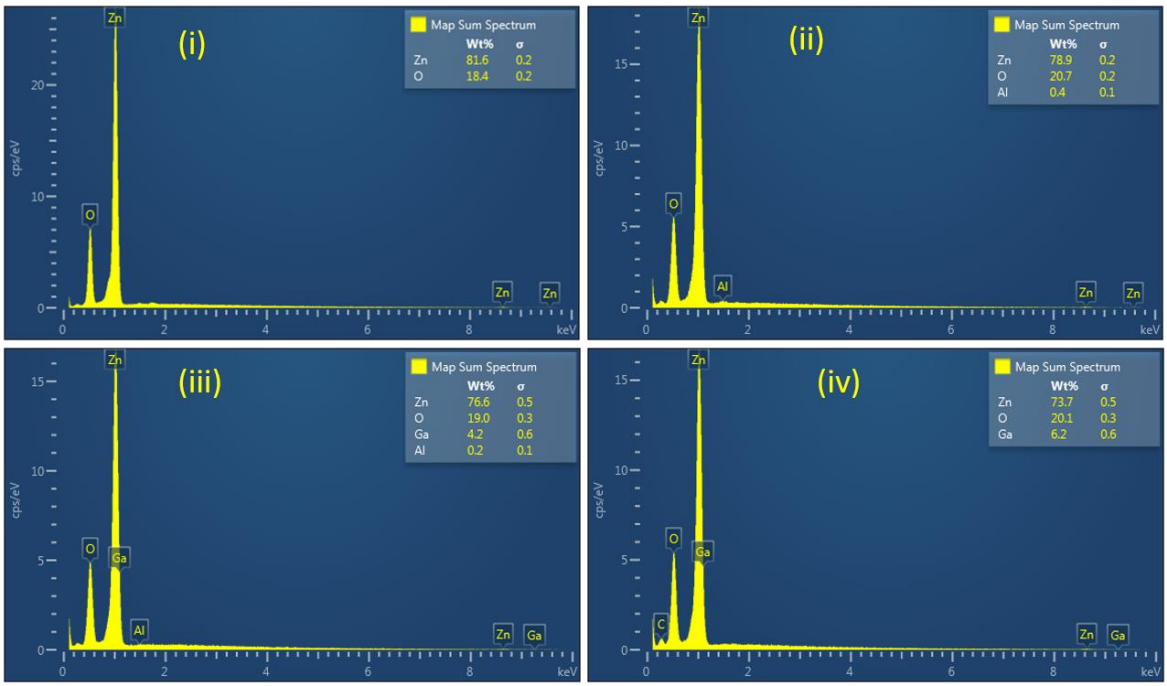

Figure 4.2: (b) EDS images of (i) ZnO, (ii) AZO (2 mol% Al), (iii) GAZO (1:1 mol% Ga/Al) and (iv) GZO (2 mol% Ga) NPs.

The EDS images for ZnO, Ga/Al-doped and co-doped ZnO NPs are shown in Fig. 4.2(b). It was established that the collected powders were composed of zinc, Ga and/or Al and oxygen as well as ZnO phase. The high purity of the prepared samples was in accordance with the XRD spectra. However, a small trace of carbon element was found in some samples attributable to the carbon tape used to hold the sample on to the holder [28].

Table 4.1: Calculated EDS elemental composition and Growth chemical contents in mol% for un-doped, Ga/Al doped and co-doped ZnO NPs.

	Composition (mol%)	ZnO (un-doped)	AZO (0% Ga, 2% Al)	GAZO (1% Ga, 1% Al)	GZO (2% Ga, 0% Al)
Zn mol.% content	EDS composition	52,03	47,96	48,26	45,58
	Growth chemical	50	49,5	49,5	49,53
O mol% content	EDS composition	47,97	51,45	48,95	50,83
	Growth chemical	49,53	49,5	49,5	49,53
O/Zn mol%	EDS composition	92,19	107,27	101,42	111,51
	Growth chemical	100	100	100	100
Ga mol% content	EDS composition	0	0	2,48	3,6
	Growth chemical	0	0	0,5	0,94
Ga/Zn mol%	EDS composition	0	0	5,14	7,88
	Growth chemical	0	0	1,01	2,04
Al mol% content	EDS composition	0	0,59	0,31	0
	Growth chemical	0	1,01	0,5	0
Al/Zn mol%	EDS composition	0	1,23	0,63	0
	Growth chemical	0	2,04	1,01	0

Table 4.1 illustrates the comparison of the EDS elemental composition in mol% as calculated from the EDS results in wt% and Growth chemical contents in mol% for un-doped, Ga/Al doped and co-doped ZnO NPs. It could be deduced that the mol% composition of Zn in the samples decreased with the increase in mol% Ga dopant; but subsequent decrease in mol% of Al, as expected. Indicating that Ga would take the substitutional position of Zn in the lattice. It is also noted that the EDS result showed relatively smaller mol% composition of Al in the sample as compared to Ga, even when the sample was doped with Al alone or when the codoping ratio was 1:1. This could be due to the difference between AZO and GZO in their Madelung energy [12]. It was reported that the lower amount of Madelung energy in GZO compared to the AZO may favor substitution of Ga in GAZO samples especially when there are less substitutional positions in the crystal structures at higher total doping levels. Moreover, from the analysis of EDS result it could be observed that there is a nearly stoichiometric O/Zn atomic ratio, within the instrumental resolution. The observed O/Zn ratio relation suggests the great convenience to achieve control over compositions of the samples as desired for different applications.

The study of elemental mapping, not shown in this paper, revealed that Zn and O elements distributed uniformly throughout the powder sample. However, the mapping did

not show the presence of Ga and Al since probably their contents are less than the limit of detection, though small peak of Al dopant could be seen in EDS images and Ga dopant peak was located same position as the Zn element on EDS images. Nevertheless, the influence of the dopants on the optical and structural properties of the NPs is clearly demonstrated.

4.3.3 Photoluminescence Analysis

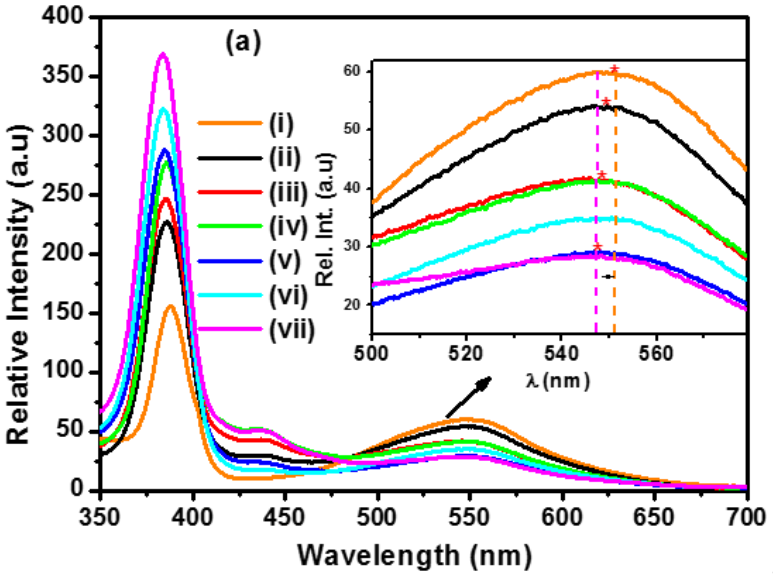

Figure 4.3: (a) RT PL emission spectra for (i) ZnO, (ii) AZO (2 mol% Al), (iii) GAZO (1:1 mol% Ga/Al), (iv) GAZO (1.5:0.5 mol% Ga/Al), (v) GAZO (1.7:0.3 mol% Ga/Al), (vi) GAZO (1.9:0.1 mol% Ga/Al) and (vii) GZO (2 mol% Ga). (Inset: enlarged spectra of DLE emissions).

Fig. 4.3(a) shows the emission spectra of ZnO and Ga/Al doped, co-doped ZnO NPs. The spectra exhibit strong UV emission between 383 and 386 nm commonly known as the exciton emission, minor emission peaks around 440 nm in the blue-green spectral region and diminished broad defect level emission (DLE) around 550 nm when excited at a 280 nm wavelength. The PL spectra clearly shows the increase in exciton peak intensity with the increase in mol% Ga in the sample, giving the GZO NPs (2 mol% Ga) the strongest luminescence band around 384 nm in the UV range. The enhanced UV emission is indicative of an improvement in crystallinity and was verified by the observable decrease in the DLE (inset Fig. 4.3a) peak intensity with the increase in mol% Ga, suggesting a continuous reduction in defects concentration. This is due to the decrease in the concentration of interstitial oxygen in the AZO/GZO nanostructures which occurs when Al or Ga is doped in ZnO. In the process the residual O ions get consumed by Al^{3+} and Ga^{3+} ions [29]. The existence of extrinsic or intrinsic point defects such as antisite oxygen (O_{Zn}),

have been commonly associated with DLE. On the other hand, the un-doped ZnO NPs depicted the lowest peak intensity of the excitonic emission but strongest DLE emission. The minor blue emission peaks around 440 nm observed in the PL spectra is commonly related to zinc vacancy [30]. The blue emission was also found to generally increase with the increase in mol% Ga in the sample.

It is clearly seen from Fig. 4.3(a) that as a result of the increase of mol% Ga concentration, the FWHM of exciton peak emission decreased. This was, again, an indication of improvement of crystallinity resulting from the increase in Ga doping levels.

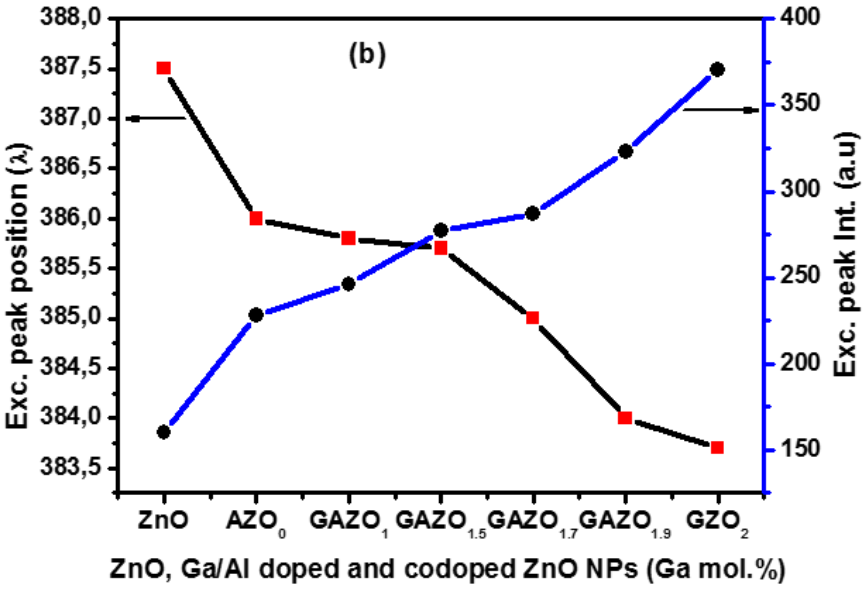

Figure 4.3: (b) Shift in exciton peak position and intensity for undoped, Ga/Al doped and codoped ZnO NPs.

As can be seen from Fig. 4.3(b), the excitonic peak positions shifted from 387.5 to 383.7 nm corresponding to ZnO and GZO NPs. The blue-shift of UV photoluminescence with increasing Ga concentration could be due to change in band gap as a result of Burstein-Moss effect triggered by doping.

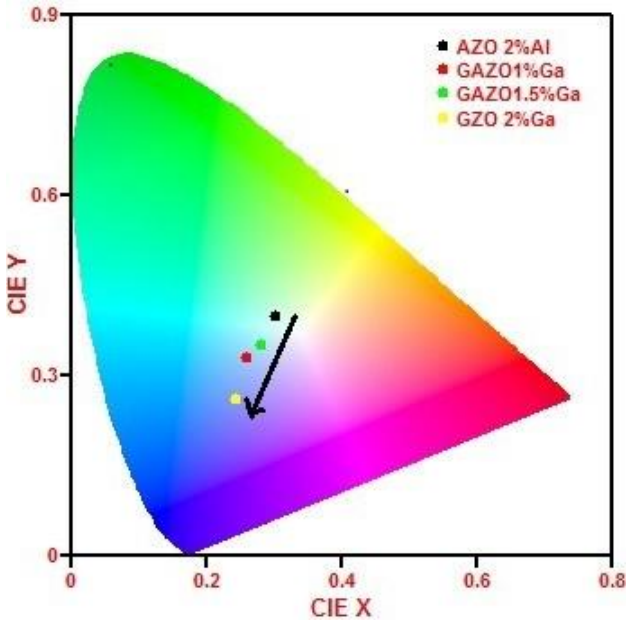

Figure 4.4: Chromaticity graph illustrating CIE color co-ordinates for AZO (2 mol% Al), GAZO (1:1 mol% Ga/Al), GAZO (1.5:0.5 mol% Ga/Al) and GZO (2 mol% Ga) NPs.

The Commission International de I'Eclairage (CIE) chromaticity diagram of Ga/Al doped and co-doped ZnO NPs are presented in Fig. 4.4. The x, y coordinates of the CIE, which is used to describe the color properties of the source of light, shifted from white toward the blue light emission with the increasing Ga doping content in the sample. The blue shift of coordinates with increasing Ga doping concentrations is also supported by the blue shift in wavelengths of the PL spectra.

4.3.4 Optical properties

The reflectance spectra of un-doped, Ga/Al-doped and co-doped ZnO NPs in the UV-vis region are presented in Fig. 4.5(a). The reflectance of the NPs was measured in the wavelength range from 300 to 600 nm. All the samples showed absorption edges around 370 nm which is close to the optical band gap of ZnO.

The absorption band edges moved towards the shorter wavelength side with increasing Ga doping levels partly, due to the variation of the crystallite sizes attributed to the improvement in the crystalline quality of the NPs [31]. The blue shift of the absorption edge of the samples could also be due to the Burstein-Moss effect [32,33] which result from increase of the carrier concentration blocking the lowest states in the conduction band since Ga dopants tend to contribute more free carriers in the structure of ZnO than Al. Therefore, the optical band gap is expected to increase by increasing the doping content of Ga. Similar results were reported in other studies [34, 35]. Moreover, [12] highlighted that since more

electrons lost from Al atoms participate in forming stronger covalent bonds less free electrons may be available to be released into the lattice of the host material as compared to Ga atoms.

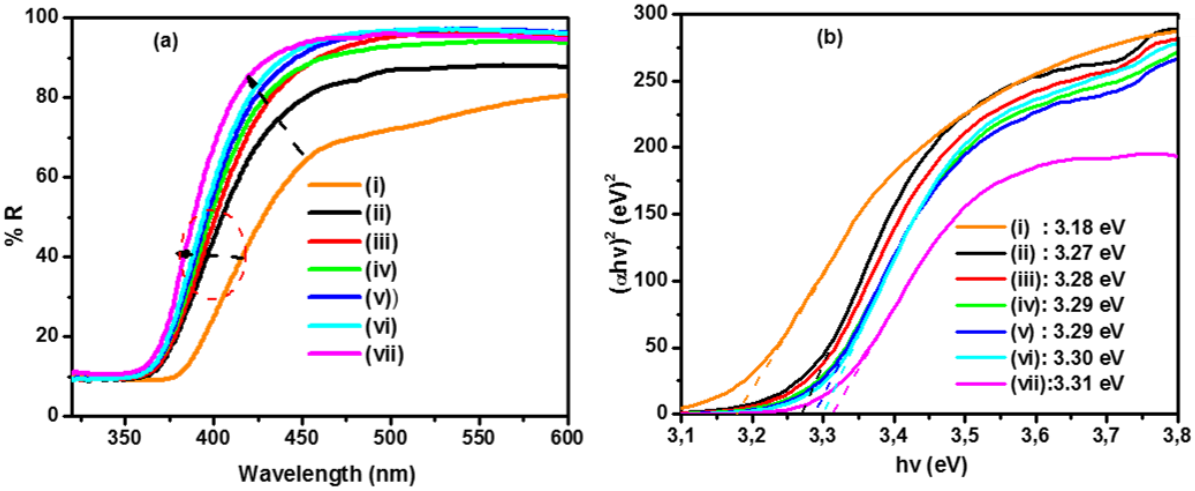

Figure 4.5: (a) Optical reflectance spectra and (b) Plot of $(\alpha hv)^2$ versus hν for (i) ZnO, (ii) AZO (2 mol% Al), (iii) GAZO (1:1 mol% Ga/Al), (iv) GAZO (1.5:0.5 mol% Ga/Al), (v) GAZO (1.7:0.3 mol% Ga/Al), (vi) GAZO (1.9:0.1 mol% Ga/Al) and (vii) GZO (2 mol% Ga) NPs.

Fig. 4.5(b) shows the optical band gap of ZnO, AZO, GAZO and GZO NPs calculated from the reflectance data by using the well-known Tauc's plot method [36],

$$(\alpha hv)^2 = A(hv - Eg) \quad (4.1)$$

Where α is optical absorption coefficient, Eg is the band-gap energy, and hv is the photon energy. The bandgap values were obtained by extrapolating the linear part of the curve of $(\alpha hv)^2$ versus (hv) to intercept x axis at $\alpha^2 = 0$. The calculated band gap increased from 3.18 eV to 3.31 eV corresponding to the energies of ZnO and GZO NPs as shown in Fig. 4.5(b). The linear band gap increase with Ga concentrations is important in attaining clear control of the process through varying Ga/Al mol% ratios so as to achieve the desired optical properties. Another explanation for the observed increase in the optical band gap with the increase in Ga doping levels could be due to the decrease in lattice defects and stress [37]. Tensile stress is known to cause a red shift in the band gap.

Conclusions

Un-doped ZnO, AZO, GAZO and GZO NPs were successfully prepared using the reflux precipitation method at a relatively low temperature (70 ºC) and at a 5 pH Zn/Ga/Al precursor solution. The XRD patterns of the impurity-doped and co-doped ZnO NPs showed

a hexagonal wurtzite crystal structure confirming the efficiency of the synthesis process. The SEM study revealed enlarged particles with an improved morphology as the Ga doping levels increased. The high purity of the samples produced shown by XRD spectra was confirmed by the EDS results which indicated that the collected powders were composed of diffraction peaks of ZnO only and the route has pure ZnO phases. The structural analysis showed that the 2 mol% Ga-doped ZnO NPs possess high crystalline quality, good crystalline size and minimum stress among its counterparts. The PL spectra also showed that the sample with a 2 mol% Ga doping level presented the maximum UV emission signal which was consistent with the least intensity of the DLE emission it portrayed, an indication of diminishing defects in the lattice. The blue shift in the exciton peak emission with the increase in Ga content closely followed the blue shift in the band edge emission triggered by the Burstein-Moss effect. The results of this work show that, indeed, Ga/Al-doped and co-doped ZnO NPs have superior material properties to their un-doped counterpart. Most importantly, the results indicate that GZO is the most suitable seeding material with fairly good material properties to make TCO thin films upon which to grow ZnO NRs for use as a photo anode in dye-sensitized solar cells.

References

[1] M. Chen, Z. L. Pei, C. Sun, J. Gong, R. F. Huang, L. S. Wen. Materials Science and Engineering, B 85, (2001) 212.

[2] B. E. Sernelius, K. F. Berggren, Z. C. Jin, I. Hamberg, C. G. Granqvist, Physical Review B 37, (1988) 10244.

[3] H. Fujiwara, M. Kondo, Physical Review B 71, (2005) 075109.

[4] T. Minami, Semiconductor Science and Technology 20, (2005) S35.

[5] T. Minami, T. Miyata, Y. Ohtani, T. Kuboi, Physica Status Solidi (RRL)-Rapid Research Letters 1, (2007) 31.

[6] A. Kahlout, N. Al, S. Al Dahoudi, K. Heusing, R. Moh Karos, P. W. De Oliveira, Nanoscience and Nanotechnology Letters 6, (2014) 37.

[7] A. AlKahlout, Journal of Sol-gel Science and Technology 67, (2013) 331.

[8] C. Y. Tsay, K. S. Fan, C. M. Lei, Journal of Alloys and Compounds, 512 (2012) 216.

[9] P. K. Nayak, J. Yang, J. Kim, S. Chung, J. Jeong, C. Lee, Y. Hong, Journal of Physics D: Applied Physics 42, (2008) 035102.

[10] W. Lee, S. Shin, D. R. Jung, J. Kim, C. Nahm, T. Moon, B. Park, Current Applied Physics 12, (2012) 628.

[11] Y. C. Li n, T. Y. Chen, L. C. Wang, S. Y. Lien, Journal of The Electrochemical Society 159, (2012) 599-604

[12] R. Ebrahimifard, M. R. Golobostanfard, H. Abdizadeh, Applied Surface Science, 290 (2014) 252.

[13] K. W. Seo, H. S. Shin, J. H. Lee, K. B. Chung, H. K. Kim, Vacuum 101, (2014) 250-256

[14] J. Liu, W. Zhang, D. Song, Q. Ma, L. Zhang, H. Zhang, R. Wu, Journal of Alloys and Compounds 575, (2013) 174-182.

[15] T. Söderström, F. J. Haug, X. Niquille, C. Ballif, Progress in Photovoltaics: Research and applications 17, (2009) 165.

[16] H. K. Lee, M. S. Kim, J. S. Yu, Nanotechnology 22, (2011): 445602.

[17] G. Achamma, J. Shajeem, IOSR Journal of Applied Chemistry (IOSR-JAC) 10(2), (2017) 60

[18] Z. F. Liu, F.K. Shan, J. Y. Sohn, S. C. Kim, G. Y. Kim, Y. X. Li, and Y. S. Yu, Journal of Electroceramics 13, (2004) 183.

[19] J. El Ghoul, C. Barthou, M. Saadoun L. El Mir Journal of Physics B 405, (2010) 597.

[20] Y. D. Ko, K. C. Kim, Y.S. Kim, Superlattices and Microstructures 51, (2012) 933.

[21] J. P. Mathew, G. Varghese, Jacob Mathew, Chinese Physics B 21, (2012) 078104.

[22] C. C. Chen, H. C. Wu, Materials 9, (2016) 164.

[23] S. Y. Kuo, W. C. Chen, F. I. Lai, C. P. Cheng, H. C. Kuo, S. C. Wang, W. F. Hsieh, Journal of Crystal Growth 287, (2006) 78.

[24] V. Kumar, Singh Neetu, R.M. Mehra, A. Kapoor, L. P. Purohit, H. C. Swart, Thin Solid Films 539, (2013) 161.

[25] B. D. Cullity, Elements of X-ray Diffraction, second ed., 1978, Addison Wesley MA, United States, (1956) 285.

[26] M. C. Jun, S.U. Park, J.H. Koh, Nanoscale research letters, 7 (2012) 639.

[27] J. Hu, R.G. Gordon, Journal of Applied Physics, 71 (1992) 880.

[28] J. Ungula, B.F. Dejene, Physica B 480, (2016) 26.

[29] D. P. Pham, H. T. Nguyen, B. T. Phan, T. M. D. Cao, V. D. Hoang, V. A. Dao, J. Yi, C. V. Tran, Advances in Condensed Matter Physics, (2014) 971528.

[30] W. Zhu, S. Kitamura, M. Boffelli, E. Marin, E. Della Gaspera, M. Sturaro, A. Martucci, G. Pezzotti, Physical Chemistry Chemical Physics 18, (2016) 9586.

[31] M. C. Jun, S. U. Park, J. H. Koh, Nanoscale Research Letters 7, (2012) 639.

[32] E. Burstein, Physical Review 93, (1954) 632.

[33] T. S. Moss, Proceedings of the Physical Society. Section B 67(10), (1954) 775.

[34] J. Liu, W. Zhang, D. Song, Q. Ma, L. Zhang, H. Zhang, X. Ma, and H. Song, Ceramics International 40, (2014) 12905.

[35] S. H. I. N. Jin-Hyun, S. H. I. N. Dong-Kyun, L. E. E. Hee-Young, L. E. E. Jai-Yeoul, Transactions of nonferrous metals society of China 21, (2011) 96.

[36] J. Tauc, R. Grigorovici, A. Vancu, Physica Status Solidi (b) 15, (1966) 627.

[37] P. Duran, F. Capel, J. Tartaj, C. Moure, Advanced Materials Interfaces 14, (2002) 137.

Chapter 5

Effects of different Ga doping concentration on structural and optical properties of Ga-doped ZnO nanoparticles by precipitation reflux

5.1 Introduction

Ga-doped ZnO (GZO) is an example of ZnO based transparent conducting oxides (TCO) being pursued in the recent time for use as photo anodes in dye-sensitized solar cells (DSSCs), due to its low resistivity, high transmittance, non-toxicity and resource availability [1]. Besides, research has shown that the structural and opto-electrical properties of GZO are comparable to those of widely employed Indium Tin Oxide TCO and the performance of GZO TCO based DSSCs was found to be superior to fluorine-doped tin oxide based DSSCs under the same growing condition [2]. Doping into the ZnO lattice by replacing Zn^{2+} ions with higher valent ions such as Ga^{3+}, Al^{3+} and In^{3+} is one way to induce dramatic changes in the electrical and optical properties and to obtain thermally stable conductivity in ZnO for solar cells applications. Ga has a similar ionic radius and covalent radius (0.062 and 0.126 nm), as compared to those of Zn (0.074 and 0.134 nm), respectively [3, 4]. Thus, Ga^{3+} can be substituted for Zn^{2+} over a larger doping range compared to other metal dopants in its group, without any lattice distortion.

Many studies on GZO nanostructures have reported an optimum concentration of 4 mol% GZO doping while others chose 2, 3, or 5 mol% GZO level to obtain thin films and other nanostructures, which have excellent material properties [5–7]. Gomez and Olvera et al. [8] reported an optical transparency in the range of 80% and a minimum electrical resistivity of the order of 7.4×10^{-3} Ωcm at 2 mol% Ga doping level. In spite of these reports, there is still a task to produce GZO NPs with excellent structural, optical and chemical properties.

A number of methods for the synthesis of GZO nanopowders have been investigated [9-11]. But unlike some which use complex processes to obtain the samples or demand very high

power synthesis conditions in temperature or pressure that makes sizing up of the product a daunting challenge, the precipitation method offers several advantages, which include cost effectiveness, high purity, homogeneity and small crystalline size of its product [12].

In this work, we focus on the optimization of the Ga doping levels in GZO NPs in order to improve the structural, optical and luminescence properties as well as to ensure a large scope of transparency not only in the visible region but also in the near UV region using the precipitation reflux method. To the best of our knowledge, there are only handful of reports in the literature on the synthesis of GZO NPs using this method.

5.2 Experimental Procedure

GZO NPs were synthesized with different Ga^{3+} concentrations. The chemical reagents sodium hydroxide (NaOH), zinc nitrate (Zn $(NO_3)_2$) and gallium nitrate hexahydrate (Ga $(NO_3)_3$. $6H_2O$) were of analytical grade and were used without further purification. In order to dope Ga in ZNPs, five different mol% doping concentrations (0, 1, 2, 4 and 5) were selected. $Zn(NO_3)_2$ was mixed with (Ga $(NO_3)_3$. $6H_2O$), dissolved in ethanol solvent to make a 0.5 M solution and put in a three-neck glass flask. The solution in the flask was heated under continuous stirring to 70 °C. 10 mg of PVP was added as a surfactant to reduce agglomeration of nanoparticles during the growth while 2 ml acetic acid was added to ensure both total dissolution of zinc nitrate and to adjust precursor solution to pH of 5.8. A solution of 1 M NaOH was added slowly (dropped for 60 minutes) into the three-neck glass flask containing zinc nitrate-gallium nitrate solution and refluxed under continuous stirring. The suspension formed with the dropping of NaOH was kept stirred for two hours at the same growth temperature and allowed to stand overnight. The material was then filtered and washed several times with deionized water with a pH of 7.5. The washed sample was dried at 60 °C in an oven for one hour and packaged into sample containers

To characterize the GZO NPs, XRD pattern was measured on a Philips model Bruker D8 Advance, Germany, X-ray diffractometer with Cu Kα irradiation (λ=1.5406 Å) in the 2θ range from 20° to 80°. To define the presence as well as different effects of Ga element on optoelectronic properties and to analyze surface morphology of GZO NPs the Jeol JSM-7800F SEM equipped with Oxford Aztec EDS was used. PL measurement was performed on a Cary Eclipse spectrophotometer (model LS-55). Finally, the reflectance spectra were collected using a Perkin Elmer Lambda 950 UV-Vis spectrometer.

5.3 Results and Discussion

5.3.1 XRD analysis

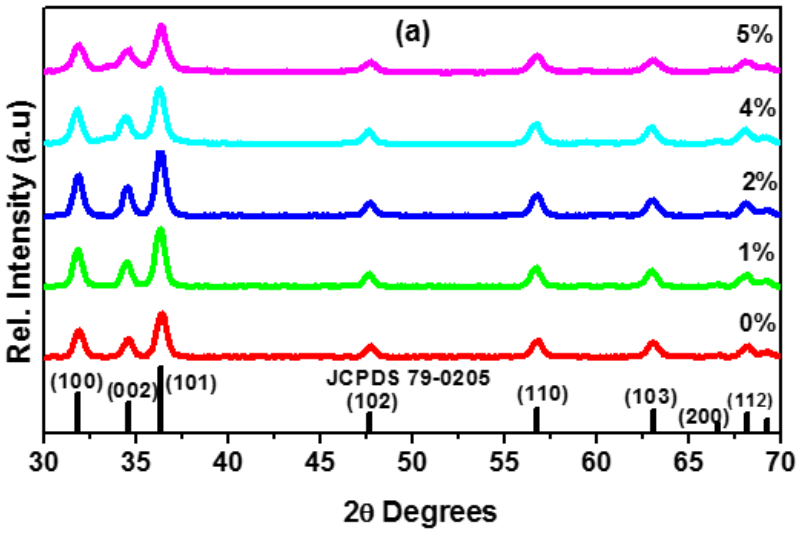

Figure 5.1: (a) X-ray powder diffraction patterns for GZO NPs prepared at different doping concentrations.

Fig. 5.1(a) shows the XRD spectra of GZO NPs synthesised at different mol% Ga doping concentrations. The diffraction patterns are made of broad peaks which match the hexagonal wurtzite structure of ZnO and are indexed to the reported values (JCPDS card, No. 79-0205). The XRD results display the diffraction peaks of ZnO only. The absence of impurity phases and other diffraction peaks such as $Zn_{1-x}Ga_xO_4$ and Ga_2O_3 proved that all the gallium ions successfully substituted for the Zn sites in the ZnO lattice when doping ZnO with gallium in this study. This also reveals that it is plausible for the Ga^{3+} to reside on zinc sites in the hexagonal lattice [13]. The average dimensions of crystallite size 'D' were estimated from the values of 2 θ and β of the XRD peaks using Scherrer's formula [14].

$$D = \frac{K\lambda}{\beta \cos\theta} \qquad (5.1)$$

where, K is the shape factor, (K = 0.94), D is the crystallite size of the particle, β is the diffraction line broadening measured at half of its maximum intensity (rad) FWHM and λ is the wavelength of X-rays used (1.5405 Å), and θ is the Bragg's diffraction angle.

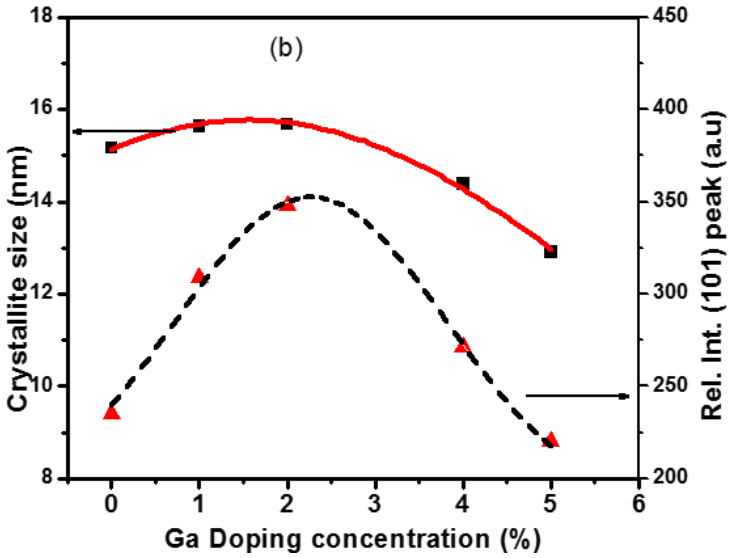

Figure 5.1: (b) Crystallite sizes and relative intensity of peak [101] as a function of Ga doping concentrations.

The crystallite sizes D and the relative intensity of peak [101] of the GZO NPs prepared at different concentration of the Ga dopant are plotted in Fig. 5.1(b). The D values are 15, 16, 16, 14 and 13 nm for 0, 1, 2, 4 and 5 mol% doping, respectively. It was observed that a small amount of Ga atoms results to the improvement in the crystalline quality and increase in crystallite size of the GZO NPs; as indicated by the highest value of D and peak intensity at the 2 mol% Ga doping concentration, but further increase in the Ga atoms lead to a decrease in the intensity of the peaks and crystallite sizes. This may be due to the fact that up to 2 mol% doping, Ga^{3+} ions replace the Zn^{2+} ions in the ZnO lattice but subsequent increase in doping levels may cause Ga^{3+} ions to occupy the interstitial positions in the ZnO lattice. Possibly, higher Ga doping levels could also weaken the crystallinity of GZO NPs due to the formation of stress caused by the smaller radius of Ga^{3+} ions (0.062 nm) compared with Zn^{2+} ions (0.074 nm).

5.3.2 Surface morphological analysis

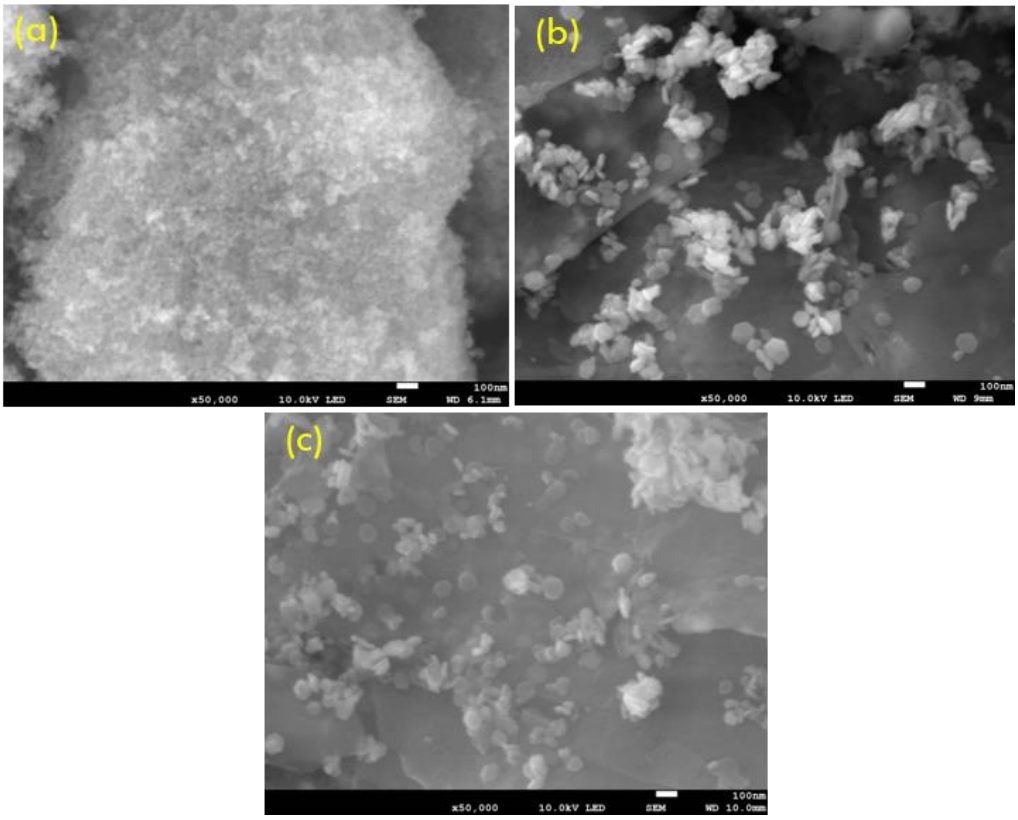

Figure 5.2: SEM micrographs of GZO NPs synthesized at (a) 0% (b) 2% and (c) 5% doping concentrations.

Figs 5.2(a-c) show the surface morphology images of the GZO NPs prepared at the different Ga doping concentrations (0, 2 and 5 mol%). Agglomerated tiny spherical particles were formed at 0 mol% doping which changed to less dense larger hexagonal shaped NPs at 2 % doping. We attribute the reduced density to the formation of large grains as a result of coalescence of the particles with the increase in doping concentration. In the case of doping at 5 mol% the observed decrease in the grain size could be due to increasing number of nucleation that result to formation of small grains when the impurities are incorporated into the host material [15]. The EDS spectra in Fig. 5.3 indicate that the nanoparticles were composed of zinc, oxygen and Ga and the route has pure ZnO phases as confirmed by XRD analysis.

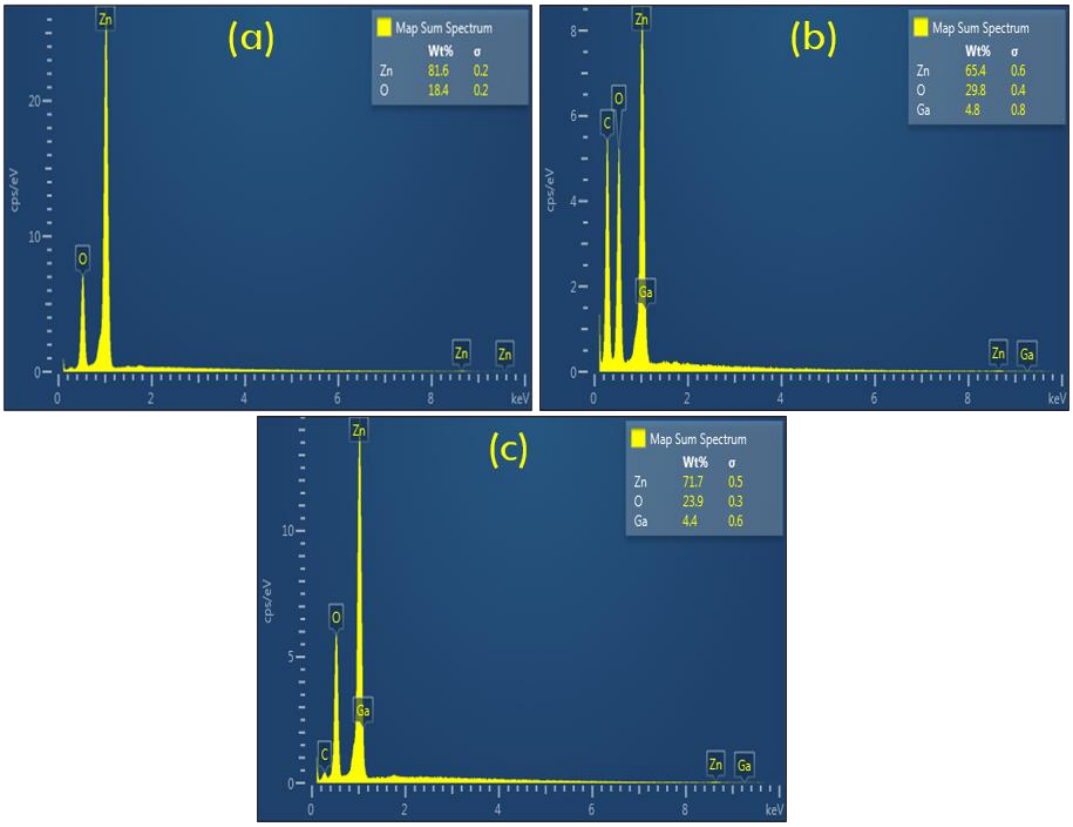

Figure 5.3: EDS spectra of GZO nanoparticles synthesized at (a) 0% (b) 2% and (c) 5% doping concentrations.

5.3.3 Photoluminescence analysis

The PL spectra of GZO NPs for different Ga doping concentrations are shown in Fig. 5.4(a), illustrating the common UV-visible emission due to near band emission (NBE) and deep level defects (DLE) along with blue emission bands around 435 nm and violet peak centred at 415-420 nm. The sharp and strong UV NBE that formed between 380 and 390 nm originated from the free exciton recombination of GZO NPs, while the DLE emissions are associated with oxygen defects [16]. It is also seen, from Fig. 5.4(a), that the intensity of the NBE emission increased as the doping concentration increased from 0 to 2% but reduced with further addition of the Ga dopant. The stronger NBE emission peak intensity in the PL indicates good optical properties of the ZnO NPs, which may be attributed to the reduced concentration of defects and improved crystallinity, in agreement with the XRD results and also as shown by the reduction of the DLE peak emission with an increase in doping concentration to 2 mol%. The quenching of the excitonic peak emission of the GZO NPs after 2 mol% Ga doping concentration was probably due to an enhanced bulk diffusion

process, defect generation and migration as a result of the increase in amount of Ga in the ZnO lattice.

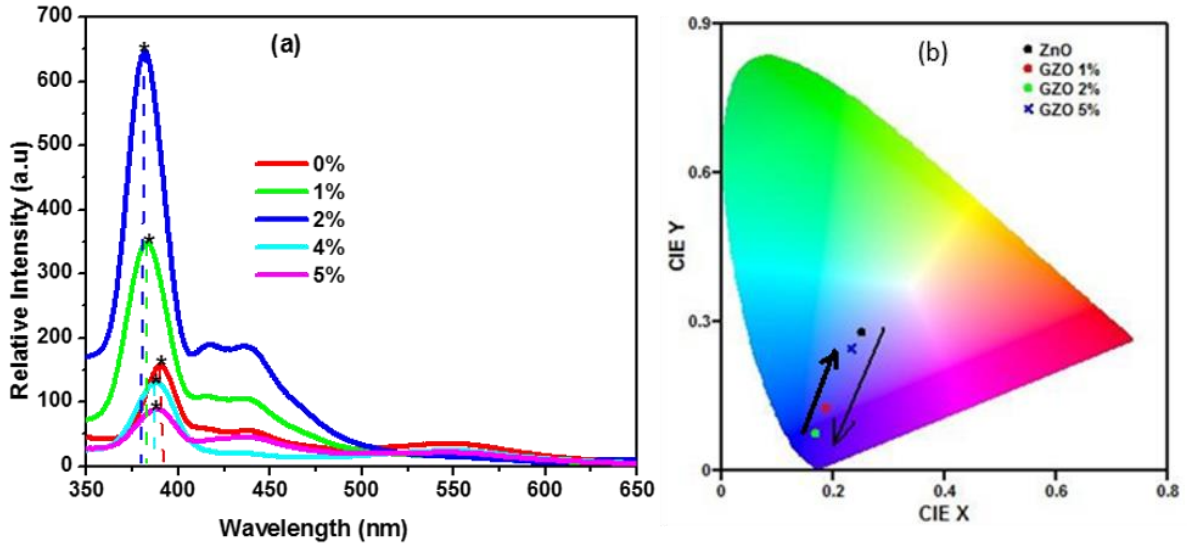

Figure 5.4: (a) PL emission spectra and (b) Chromaticity diagram depicting the CIE colour co-ordinates for GZO NPs for the different doping concentrations.

The violet peak observed in most samples, which was centred around 419 nm, was slightly shifted to larger wavelengths and increased in intensity with the increase in doping concentration to 2 mol%. The violet peak is associated with emission from the radiative transition between interface traps at the grain boundaries and the valence band [17]. Jeong et al. [18] also observed that the violet peak could arise from Zn vacancies.

The Commission International de I'Eclairage (CIE) chromaticity diagram of the GZO NPs is shown in Fig. 5.4(b). The CIE (x, y) colour co-ordinates for 0, 1, 2, 4 and 5% Ga doping concentrations are (0.25, 0.28), (0.19, 0.13), (0.168, 0.075), (0.28, 0.36) and (0.23, 0.25), respectively. The co-ordinates shift toward the shorter wavelength with the increase in mol% doping concentration but change to longer wavelengths for a further doping increase after 2 mol%. The blue shift of the co-ordinates with an increase in amount of dopant in the sample is also supported by the PL spectra wavelength shifts.

5.3.4 Optical properties

The reflectance spectra of the GZO NPs in the wavelength range of 300–600 nm are shown in Fig. 5.5(a). It can be observed that the onset of the band edge absorptions for the samples has shifted to the blue region of the spectrum with the increase in doping levels from 0 to 2%, and red shifted with a further increase in the doping concentration confirming the size dependent absorption properties of the GZO NPs.

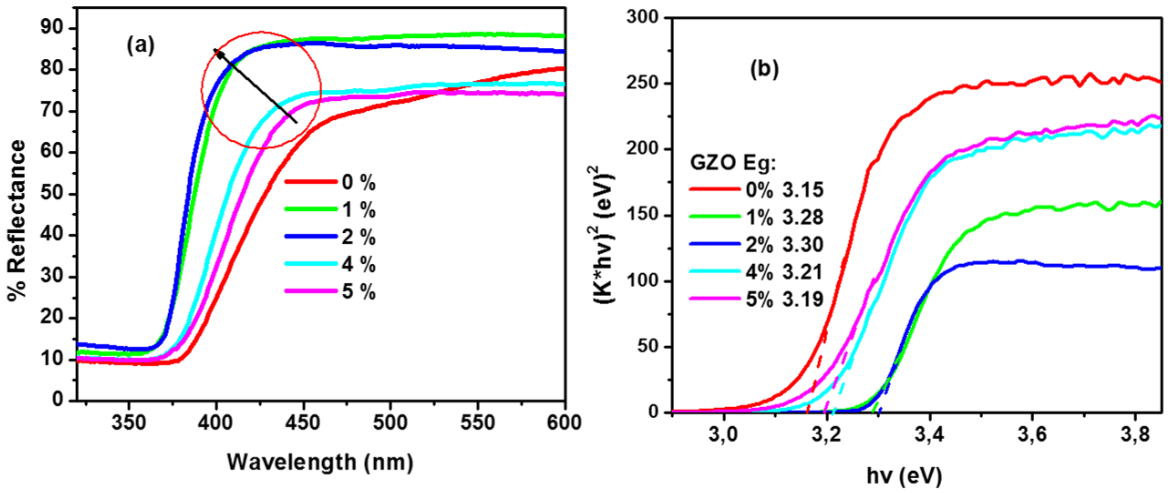

Figure 5.5: (a) The reflectance spectra and (b) Plot to determine the band gap energy of GZO nanoparticles prepared at various doping concentrations of Ga.

Similarly, the % reflectance in the UV region has increased as the doping levels increased to 2 mol%, but dropped as the concentrations increased to 5 mol%. Fig. 5.5(b) shows the plot to determine the optical band gap of the ZnO NPs by extrapolating the linear region of the $(Khv)^2$ versus hv graph to the energy axis, x = 0 value. The plots were obtained using the common Tauc's relation [19].

$$(Khv)^2 = A(hv - Eg)^2 \quad (5.2)$$

Where K is reflectance transformed according to the Kubelka-Munk remission function [20],

$$K = \frac{(1-R)^2}{2R} \quad (5.3)$$

hv is the photon energy, Eg is the optical band-gap energy between the valence band and the conduction band at n = 2 for direct transitions and A is a constant, depending on the electron–hole mobility and R is reflectance (%). The calculated band gap energy was found to be 3.15, 3.28, 3.30, 3.21 and 3.19 eV corresponding to the Ga doping ratios of 0, 1, 2, 4, and 5% respectively as shown in Fig. 5.5(b). The band gap values increased slightly with increasing Ga doping concentration to 2 mol%, and then decreased at higher doping. The highest optical band gap, 3.30 eV, was achieved in the GZO NPs doped with 2 mol% Ga due to the increase in carrier concentration, at this moderately doped level, caused by the contribution of Ga^{3+} ions at substitutional sites of Zn^{2+} ions and the higher energy-gap that

resulted from the Ga interstitial atoms. The extrapolated absorption onset is slightly blue shifted on increasing the Ga doping concentration. This absorption edge which shifts towards higher energy is associated with an increase of the carrier concentration blocking the lowest states in the conduction band as explained by Burstein-Moss effect [21, 22].

Conclusions

This study demonstrates that GZO NPs of high quality can be synthesised at a relatively low temperature (75 ºC) by precipitation reflux method by varying the Ga/Zn doping concentrations. It was established that the structural and optical properties of the GZO NPs depend strongly on the Ga doping levels. The XRD results showed the hexagonal phase pattern and the nanometric behaviour of the crystallites formed thus indicating the efficiency of synthesis process. This result shows that GZO NPs prepared at 2% Ga doping concentration exhibit the best crystal quality. Agglomerated tiny spherical particles were formed at 0% doping which changed to less dense larger hexagonal shaped NPs at 2% doping. It was seen that the intensity of the NBE emission increased as the doping concentration increased from 0 to 2% but reduced with further doping indicative of the superior optical properties at 2 mol% doping. The highest optical band gap, 3.30 eV, was also achieved in the GZO NPs doped with 2 mol% Ga due to the increase in carrier concentration, at this moderately doped level. The results of this work shows that a 2 mol% Ga-doped ZnO target is most suitable to make thin films with fairly good material properties for the use as a photo anode in DSSCs.

References

[1] M. Netrvalova I. Novotny L. Prusakova, V. Tvarozek, P. Sutta, Vacuum 86, (2012) 707–710

[2] H. Liu, V. Avrutin, N. Izyumskaya, Ü. Özgür, H. Morkoç, Superlattices and Microstructures 48(5), (2010) 458-484.

[3] P. K. Nayak J. Yang, J. Kim, S. Chung, J. Jeong, C. Lee, Y. Hong, J. Phys. D: Appl. Phys. 42, (2009) 035102

[4] K. Yoshino, T. Hata, T. Kakeno, H. Komaki, M. Yoneta, Y. Akaki, T. Ikari, Phys. Stat. Sol. (c) 0**,** (2003) 626.

[5] K. Jung, W. K Choi, S. J. Yoon H. J. Kim, J. W. Choi, Applied Surface Science 256, (2010) 6219.

[6] A. Miyake, T. Yamada, H. Makino, N. Yamamoto, T. Yamamoto, Thin Solid Films 517, (2008) 1037-1041.

[7] S. Nagarani, C. Sanjeeviraja, American Institute of Physics Conference Proceeding 1349, (2011) 589-590.

[8] H. Gomez, M. de la L. Olvera, Mater. Sci. Eng. B 134, (2006) 20-26.

[9] S. Du, Y. Tian, H. Liu, J. Liu, Y. Chen, Journal of the American Ceramic Society 89(8), (2006) 2440-2443.

[10] K. J. Chen, T. H. Fang, F. Y. Hung, L. W. Ji, S. J. Chang, S. J. Young, Y. J. Hsiao, Applied surface science 254(18), (2008) 5791-5795.

[11] J. Guo, J. Zheng, X. Song, K. Sun, Materials Letters 97, (2013) 34-36.

[12] K. Chongsri, W. Pecharapa, Integrated Ferroelectrics 165(1), (2015) 159-166.

[13] D. H. Zhang, T. L. Yang, J. Ma, Q. P. Wang, R. W. Gao, H. L. Ma, Materials Research Express 2, (2015) 9.

[14] R. S. Wagner, C. Doherty, J Electroceram Soc. 113 **(**1300 3), (1996) 4596.

[15] J. Hu, R. G. Gordon, J Appl. Phys. 72, (1992**)** 5381.

[16] B. Lin, Z. Fu, Appl. Phys. Lett 79, (2001) 943.

[17] B. J. Jin, S. Im, S. Y. Lee, Thin Solid Films 366, (2000) 107-110.

[18] S. H. Jeong, B. S. Kim, B. T. Lee, Appl. Phys. Lett 82, (2003) 2625.

[19] J. Tauc, R. Grigorovichi, A. Vancu, Phys. Status Solidi 15, (1966) 627.

[20] P. Duran, F. Capel, J. Tartaj, C. Moure, Adv. Mater 14, (2002) 137.

[21] E. Burstein, Physical Review 93, (1954) 632-633.

[22] T. S. Moss, Proceedings of the Physical Society Section B 67, (1954) 775.

Chapter 6

Effect of annealing on the structural, morphological and optical properties of Ga-doped ZnO nanoparticles by reflux precipitation method

6.1 Introduction

Zinc oxide (ZnO) is a well know n-type semiconductor having a wurtzite structure with a wide-band gap of 3.34 eV and a large exciton binding energy of 60 meV [1-2]. Besides its exceptional performance in electronics, photonics, catalysis, lighting, and chemical sensing, ZnO has received considerable attention in the recent times for use as alternative transparent conductive oxides (TCO) material due to advantages that include high electrical conductivity and high transmission in the visible region [3] and due to its attractive electrical and optical properties, low cost, abundant material resources and non-toxicity [4]. Indium-tin-oxides (ITO) presently used in industry as transparent electrodes have some concerns regarding its future availability, unstable supply, and increased cost of indium. However, the electrical resistivity of ZnO is too high (~10^{-3} Ωcm) to be used as a TCO [5]. So, group III elements such as aluminium, boron, indium, and gallium are used as a dopant to improve its electrical conductivity, crystal quality and optical transmittance in the visible (VIS) and near UV range [6, 7]. Group III doped ZnO thin films have been intensively researched for TCO applications such as flat panel displays, liquid crystal displays (LCDs), organic light-emitting diodes (OLEDs), and dye-sensitized solar cells (DSSCs) [8-10].

Compared to other metal dopants in its group, gallium is preferred for ZnO for application as TCO because GZO is more stable with respect to oxidation due to gallium's greater electronegativity in comparison with aluminium [11] and Ga ionic radius and covalent radius are nearly equal to that of Zn [12, 13]. Thus, Ga^{3+} can be substituted for Zn^{2+} over a larger doping range. There is, however, a charge compensation needed when Ga^{3+} replaces Zn^{2+}. This is normally done by the formation of oxygen defects. A number of methods for the synthesis of GZO nanostructure materials have been investigated. But

unlike some which use complex processes to obtain the samples or demand very high power synthesis conditions in temperature or pressure that makes sizing up of the product a daunting challenge, the precipitation reflux method offers several advantages, which include low temperatures, simple equipment and it is a low-cost method. Additionally, the above method has a high degree of versatility to modify several parameters, such as temperature, pH, and concentration of reactants, which in turn could modify the morphology, size and shape of the nanomaterials.

As far as the effect of annealing on GZO nanomaterials is concerned, the available literature majorly reports on the effect of annealing on GZO films, there are very few reports on GZO NPs. Y. Q. Li et al. [14] in their study on preparation of Ga-doped zinc oxide (GZO) nanoparticles by a polymer pyrolysis method reported that GZO NPs calcined at 600 °C show good crystallinity with the wurtzite structure. While, J.K. Sheu et al. [15] conducted annealing with temperature ranging from 400 to 800 ºC and reported the reduction in resistivity of GZO films which could be attributed not only to the activation of Ga dopants and to the increase of electron mobility but also to the enlargement of the grain size that occurred as a result of thermal annealing. K. Yim et al. [11] reported that annealing in an O_2 atmosphere makes the band gap of GZO film narrower, which can be explained as a red shift phenomenon due to grain growth. Tao-Hsing Chen et al. [16] in their work on the investigation into the properties of Ti-Ga–doped ZnO films also reported that the crystallinity of the ZnO film improves with an increasing annealing temperature (AT) only up to 400 °C and is accompanied by a smaller crystallite size and a lower surface roughness.

In our previous project, we reported improved optical and structural properties of GZO NPs at [Zn/Ga] 2 mol% ratio by reflux method. Annealing at different temperatures is required to enhance further the material properties of GZO NPs. For this reason, in the present investigation, effect of annealing on the structural, optical and luminescence properties of ZnO: Ga (2 mol%) NPs are studied. We aim to optimize the energy-band structure and effectively adjust the intensity of the luminescence properties of GZO NPs through annealing. These GZO NPs with enhanced crystallinity, minimum lattice stress, and lowest reflectance in the visible range at a relatively lower AT would be useful for deposition on a glass substrate to form the seed layer to produce a transparent conducting oxide.

6.2 Experimental procedure

The chemical reagents sodium hydroxide (NaOH), zinc nitrate ($Zn(NO_3)_2$) and gallium nitrate hexahydrate ($Ga(NO_3)_3.6H_2O$) were of analytical grade and were used without further purification. GZO NPs were synthesized by a simple precipitation reflux method. In order to dope Ga in ZNPs, Ga/Zn 2 mol% doping concentration was selected. ($Zn(NO_3)_2$) was mixed with ($Ga(NO_3)_3.6H_2O$), dissolved in ethanol solvent to make a 0.5 M solution and put in a three-neck glass flask. The solution in the flask was heated under continuous stirring to 70 °C. 10 mg PVP was added as a surfactant to reduce agglomeration of nanoparticles during the growth while 2 ml acetic acid was added to ensure total dissolution of zinc nitrate, and to prevent the formation of hydroxides. A solution of 1 M NaOH was added slowly (dropped for 60 minutes) into the three-neck glass flask containing zinc nitrate-gallium nitrate solution and refluxed under continuous stirring. The suspension formed with the dropping of NaOH was kept stirred for two hours at the same growth temperature and allowed to stand overnight. The material was then filtered and washed several times with deionized water. The washed sample was dried at 60 °C in an oven for one hour and some portions annealed in air at 300, 500 and 600 °C. The powders were annealed in air to the desired annealing temperatures from RT, held isothermally for 2 hrs. inside a programmable heat furnace until complete transformation took place and cooled in furnace to RT.

The crystal structure of the NPs was analyzed with an Advanced D8 Bruker powder diffractometer (XRD) with a Cu anode x-ray tube (with a K radiation wavelength of 1.54 Å). The average dimensions of crystallites were determined by the Scherer method from the broadening of the diffraction peaks. The surface morphology was studied using Jeol JSM-7800F Field Emission equipped with Oxford Aztec EDS (Energy-dispersive X-ray spectroscopy). Photoluminescence (PL) measurements were performed on a Cary Eclipse fluorescence spectrophotometer; model LS-55 with a built-in 150W xenon flash lamp as the excitation source and a grating to select a suitable excitation wavelength. The reflectance spectra were collected using a Perkin Elmer Lambda 950 UV-Vis photo spectrometer.

6.3. Results and Discussion

6.3.1 XRD Analysis

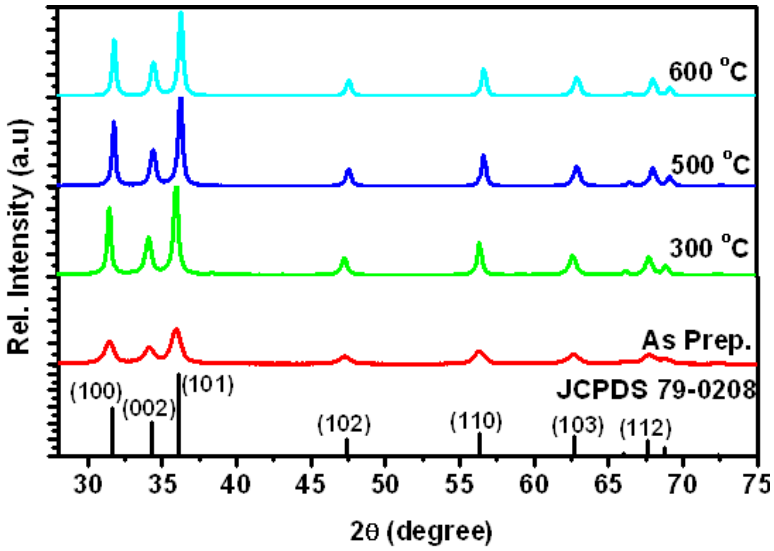

Figure 6.1: (a) X-ray diffraction patterns for Ga-doped ZnO NPs of as-prepared, 300, 500 and 600°C ATs.

Fig. 6.1(a) shows the XRD patterns of the as-prepared GZO NPs, as well as the NPs annealed at 300, 500 and 600 °C. It shows that all NPs have hexagonal wurtzite crystal structure of ZnO [17, 18], which matches well with space group $P6_3mc$ (No. 186) (JCPDS No. 79–0208). The XRD results show only diffraction peaks of ZnO without any trace of other diffraction peaks such as $Zn_{1-x}Ga_xO_4$ and Ga_2O_3.

The variation in diffraction peak intensity and position of the GZO NPs with the AT, in the 2θ region from 35° to 37°, are analyzed in Fig. 6.1(b). The diffraction peak becomes more intensified and narrower with annealing insinuating improvement in crystallinity of the NPs [19]. GZO NPs annealed at 300 °C registered the highest intensity, indicative of most enhanced crystallinity and grain growth. Because, partly, at this annealing temperature Ga^{3+} have already incorporated into the ZnO matrix as substitutional impurities on Zn lattice sites. The intensity fell slightly at higher ATs any further increase in temperature causes the displacement of Ga ions from substitutional position to interstitial or to grain boundaries resulting into poor crystallinity. This is confirmed by reduction of peak intensities at higher ATs.

The decrease in the FWHM of the diffraction peaks with the increase of the AT can be attributed to the coalescences of grains at higher ATs [20]. The shift to a higher angle of diffraction peak (101) with the increase in AT is occasioned by a change in stress in the GZO NPs [21] and may be related to decrease of lattice parameters that come from the oxygen deficiency and strain caused by crystallization during annealing process [22]. Additionally, ZnO NPs are known to have defects such as zinc antisites, oxygen vacancies and lattice disorders, which are reported to disappear with annealing resulting to the contraction of lattice. Flemban et al (23) also noted that isolated oxygen vacancy introduces shrinkage in both lattice parameters. It was observed that the diffraction peak [101] of the annealed samples were located at a higher diffraction angle, which meant smaller d value, than that of the as prepared once. During annealing, oxygen vacancies were generated while the majority Zn atoms were in the same valence state. It was suggested that oxygen vacancies might reduce the lattice strain and corresponding lattice parameters, at least the c value.

Furthermore, it is unlikely that the peak shifts observed could be due to the zero drift from the XRD equipment. Because, zero position was corrected before the scan, every sample was aligned in the same manner and all measurements conditions for the equipment is the same. Since, we have got good peak intensity more than 30 000 counts with invisible background or noises, a linear shift towards a higher 2θ with the AT could reflect that the shift can only be 'real.'

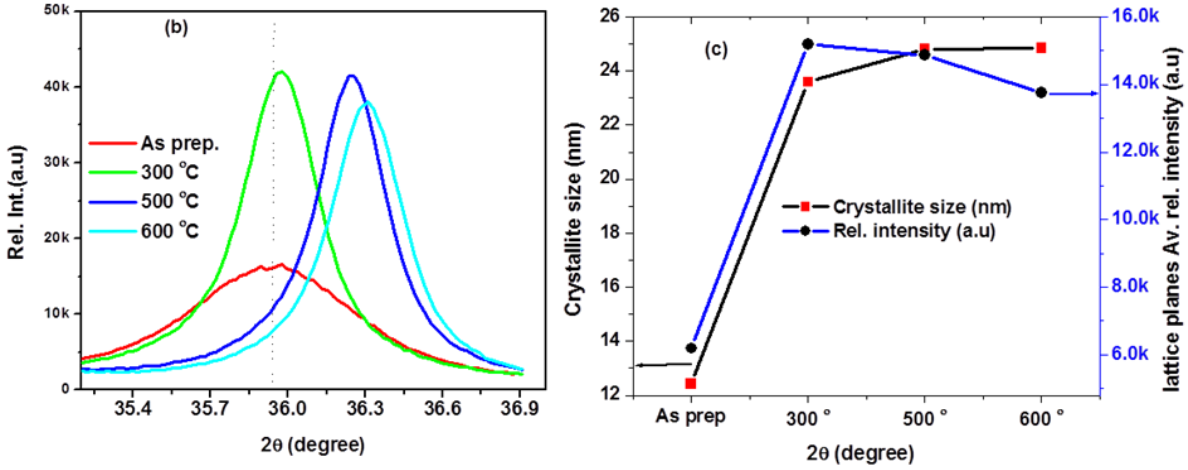

Figure 6.1: (b) relative intensity and position shift of [101] diffraction peak (c) crystallite size and the average relative intensity of various lattice planes for the Ga-doped ZnO NPs of as-prepared, 300, 500 and 600°C ATs.

The crystallite sizes of GZO NPs were calculated using the Scherer's formula [24].

$$D = \frac{K\lambda}{\beta_G \cos\theta} \quad (6.1)$$

where K is the shape factor (0.94), D is the crystallite size, β_G is the corrected integral breadth of the Gausian component in radians of the diffraction lines of XRD pattern;{β_G= $(B^2 - b^2)^{\frac{1}{2}}$, where B is the broadening of the observed sample and b is the instrumental broadening correction} λ is the wavelength of X-rays used (1.5405 Å), and θ is the Bragg's diffraction angle. The crystallite sizes calculated were 12, 24, 25 and 25 nm for the as-prepared NPs and 300, 500 and 600 ºC annealed samples as shown in Fig. 6.1(c). It is observed that the crystallite sizes of GZO NPs increased during annealing pointing out to the tendency of large grain growth in the nanoparticles that occurs as a result of movement of atoms to the favorable positions [25] to merge into adjacent particles forming larger particles due to annealing. The GZO NPs annealed at 300 ºC displayed the lowest crystallite size among the annealed samples.

To identify the effect of annealing and investigate the reason for the diffraction peak shift the lattice parameters (a and c) were estimated from the relation [26]. The experimental average lattice constants *a* and *c* of GZO NPs for [002], [101], [102], [103] and [112] lattice planes were determined as; As prep.(3.281, 5.207), 300 ºC (3.278, 5.211), 500 ºC (3.249, 5.207) and 600 ºC (3.244, 5.206) respectively, giving average lattice constants as a = 3.263 and c = 5.208 Å. These values are very close to ZnO ones in the JCPDS card result, i.e., a = 3.264 Å and c = 5.219 Å. The deviation of the lattice parameters may be due to the presence of various point defects as explained earlier. The mean ratio c/a of GZO NPs is 1.595 and is slightly less than that of pure ZnO (1.604). Moreover, values of the lattice parameter 'a' and 'c' decreased with an increase in AT. V. Kumar et al. [27], attributed the decrease in the values of lattice parameter to the lattice contraction that may have resulted from the presence of dangling bonds on the surface of the ZnO films. The above structural analysis reveals that an AT of 300 °C is essentially required to obtain GZO NPs with high crystalline quality and minimum stress.

6.3.2 SEM and EDS Analysis

The SEM images in Figs. 6.2(a-d) show the changes in morphologies of GZO NPs from regular hexagonal shapes to agglomerated and enlarged particles as the AT was increased. The annealed samples contained a mixture of nanorods and nanospheres. The grains also became denser with annealing, which can be considered the result of the coalescence

process, with the increase in AT. The results indicated that the crystal growth of the GZO NPs can be controlled by the AT. This is in good agreement with the XRD result.

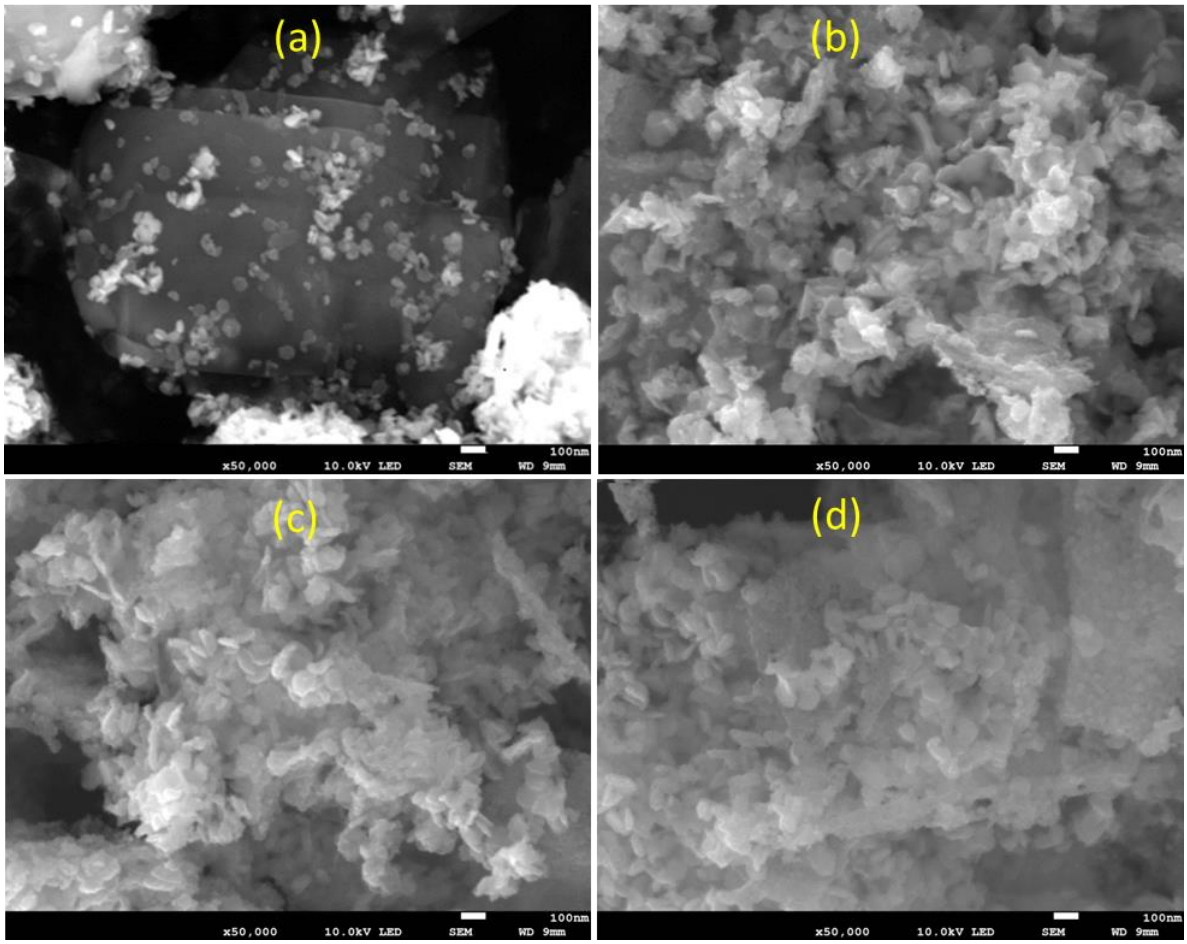

Figure 6.2: SEM micrographs of the Ga-doped ZnO NPs of (a) as-prepared (b) 300 (c) 500, and (d) 600 °C ATs, respectively.

The analysis of EDS spectra for GZO NPs annealed at different temperatures indicated that the collected powder was composed of zinc, gallium and oxygen in conformity with the XRD spectra which showed no presence of impurity phases. This also shows that the powder was successfully doped with Ga. However, a small trace of carbon element was found in all samples which could be attributed to the carbon tape used to hold the sample for characterization on the sample holder [28].

6.3.3 Photoluminescence Analysis

Fig. 6.3(a) shows the emission spectra of GZO NPs annealed at different AT. The spectra exhibit strong narrow bands at ~380 nm and emission peaks around 440 nm in the blue-green spectral region when excited at 280 nm wavelength. The UV emission corresponds to

near band edge emission due to free exciton recombination. The GZO NPs annealed at 300 ºC showed the strongest luminescence band around 384 nm in the UV range among the annealed samples. Unlike reports by many studies [29] the intensity of the UV emission peaks was found to be decreasing with annealing. It is generally understood that the annealing process enhanced the PL intensity due to the improvement in crystallinity which is known to reduce the recombination as a result of decreased density of defects. The improved crystallinity reduces the recombination centers in the NPs. Consequently, there is a decrease in non-radiative recombination and increase in radiative recombination for non-equilibrium photo generated carriers [30]. However, there are instances when the emission peaks are reported to decrease in intensity with annealing in agreement with our result. V. Kumar et al. [31] observed the decrease in integral intensity of the peaks corresponding to each defect state as well as the band to band transitions. This decrease in intensity of the emission peaks with the increase in AT was attributed to the decrease in defects concentrations in ZnO after annealing.

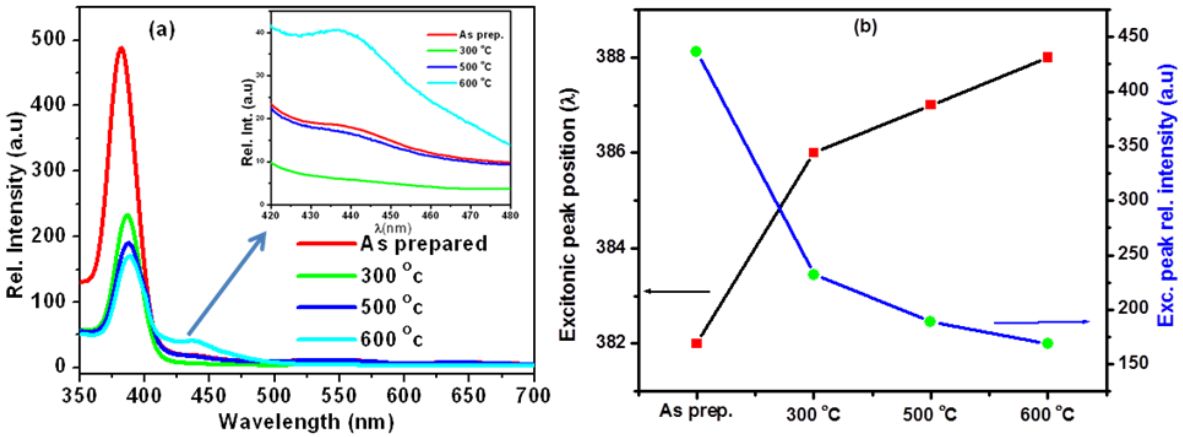

Figure 6.3: (a) PL emission spectra of GZO NPs (inset) Enlargement of blue peak emission around 440 nm (b) Changes in excitonic peak position and rel. intensities for different ATs.

The peak at 440 nm (inset: Fig. 6.3(a)) is a blue emission, which could originate from the defect emission of oxygen vacancies [32]. The peak intensity corresponding to blue emission has been found to increase with the increase of AT. The increase in AT caused the depletion of the grains which played a major role in increasing defect densities [33, 34]. The increase of particle size increased the volume ratio of bulk to depletion region and caused the intensity of non-radioactive recombination to increase. The emission around 550 nm peak which has been associated with the presence of various point defects: extrinsic or intrinsic, like antisite oxygen (O_{Zn}) was fully quenched in all samples indicating a very low concentration of such vacancies in our samples.

It is clearly observed from Fig. 6.4(a) that as a result of the increase of AT, FWHM of excitonic peak emission decreased. This was due to the improvement of crystallinity in the GZO NPs and is in conformity with the XRD measurements. It is also observed from the Fig. 6.3(b) that as the annealing temperature was increased from 300 to 600 ºC; the UV peak position has shifted from 380 to 389 nm. Fonoberov and Balandin [35] have theoretically reported two possible reasons for the red-shift of UV emission in ZnO NPs: excitons confined in the nanoparticles and excitons bound to an ionized impurity located at the nanoparticle surface. The red-shift of UV photoluminescence in our samples was due to the influence of the size effect on the energy level of the confined excitons because the average size of the nanoparticles became bigger with the increase of AT.

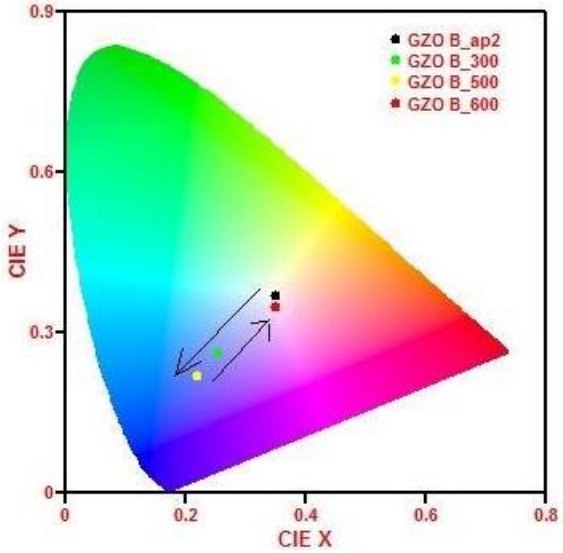

Figure 6.4: Chromaticity diagram depicting CIE colour co-ordinates for as prepared and differently annealed GZO NPs.

The Commission International de I'Eclairage (CIE) chromaticity diagram of GZO NPs before and after annealing is shown in Fig. 6.4. The x, y coordinates of a CIE diagram can be used to describe the color properties of a light source. The coordinates shifted from white toward the blue light emission after annealing. The blue shift of coordinates with the increase in AT sample is also supported by the PL spectra wavelength shifts.

6.3.4 Optical properties

The reflectance spectra of GZO NPs for different ATs in the UV and visible range are presented in Fig. 6.5(a). The reflectance of the NPs was measured in the wavelength range from 300 to 600 nm. All the samples showed absorption edges around 370 nm which corresponded to the optical band gap of ZnO. The absorption band edges moved towards the longer wavelength side with increasing AT due to the size effect of nanostructures [36]. The

red shift is also reported to correspond with the variation of the crystallite sizes attributed to the improvement in the crystalline quality of the NPs. It is important to notice that, the percentage reflectance (% R) in both the UV and visible region of the spectrum increased with the increase in AT, with the GZO NPs annealed at 300 °C showing the lowest % R in both cases.

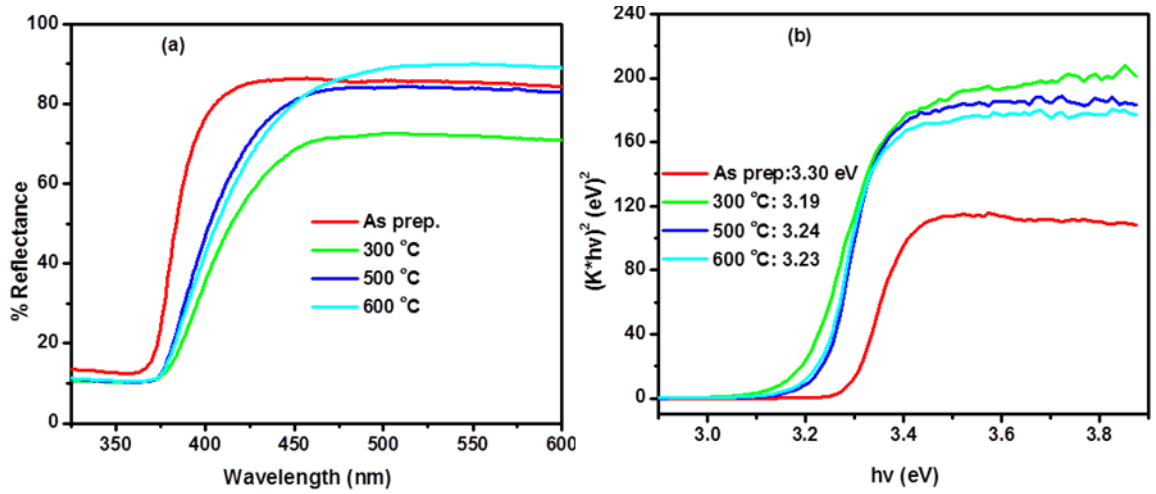

Figure 6.5: (a) Optical reflectance spectra (b) Plot of $(\alpha h\nu)^2$ versus hν for as prepared and differently annealed GZO NPs.

Fig. 6.5(b) shows the plot used to obtain the optical band gap of GZO NPs calculated using the common Kubelka Munk's equation. The plots for the graph of $(Khv)^2$ versus hv were obtained using the following equation [37]:

$$(Khv)^2 = A(hv - Eg)^2 \quad (6.2)$$

Where K is reflectance transformed according to Kubelka-Munk remission function [38],

$$K = \frac{(1-R)^2}{2R} \quad (6.3)$$

hv is the photon energy, E_g the optical band-gap energy between the valence band and the conduction band at n = 2 for direct transitions and A is a constant, depending on the electron–hole mobility, having a value between 10^5 and 10^6 cm^{-1} and R is reflectance (%). The point of the extrapolation of the linear part that meets the abscissa will give the value of the band gap energy (Eg) of the material.

The calculated band gap values are 3.30, 3.19, 3.24, and 3.23 eV for as prepared and treated samples at 300, 500 and 600 ºC, respectively. Clearly, the optical band gap of GZO NPs reduced appreciably with a change in nanoparticle size from 12 nm to 25 nm as caused by the increase in AT. The red-shift of the band-gap energy may be attributed to the increase in particle size with increasing AT as shown by XRD and SEM data. Another explanation for the observed decrease in the optical band gap with the increase in AT could be due to the

variation in lattice defects and stress [39]. Tensile stress is known to cause a red shift in the band gap. The annealing process improved the crystallinity, increased the average grain size and decreased defects, therefore band gap energy decreased [40].

Conclusions

Gallium-doped ZnO nanoparticles were successfully prepared using the precipitation reflux method at relatively low temperatures (70 ºC) and annealed at 300, 500 and 600 °C. The XRD patterns of the as-prepared and annealed NPs showed a hexagonal wurtzite crystal structure confirming the synthesis process efficiency. The SEM study revealed the formation of an agglomerated and enlarged particles as the AT increased in contrast to tiny hexagonal shaped particles observed for as prepared GZO NPs. The high purity of the GZO NPs shown by XRD spectra was confirmed by the EDS results which indicated that the collected powder was composed of only diffraction peaks of ZnO without any trace of other diffraction peaks and the route has pure ZnO phases. The PL spectra showed that GZO NPs annealed at 300 ºC showed the maximum UV emission among the annealed samples and this was consistent with the least % reflectance in the UV and visible regions as seen on the reflectance curve. The red shift in the exciton peak emission with increasing crystallite sizes closely followed the red shift in the band edge emission. The observed red shift in the position of the band edge emission could be due to band gap narrowing as a result of the increase in crystallite size due to annealing. The results of this work show that Ga-doped ZnO NPs annealed at 300 °C is most suitable to make thin films with fairly good material properties for the use as a photoanode in dye sensitized solar cells. At the annealing temperature of 300 ºC we were able to produce better quality GZO NPs with high crystallinity, lowest crystallite size, minimum lattice stress, lowest % reflectance and strongest PL UV emission (among the annealed samples).

References

[1] A. Janotti, C. G. Van de Walle, Reports on Progress in Physics 72, (2009) 126501–126529.

[2] F. Z. Bedia, A. Bedia, N. Maloufi, M. Aillerie, F. Genty, B. Benyoucef, Journal of Alloys and Compounds 616, (2014) 312–318.

[3] E. Fortunato, A. Goncalves, A. Pimentel, P. Barquinha, G. Goncalves, L. Pereira, I. Ferreira, R. Martins, Applied Physics A: Materials Science & Processing 96, (2009) 197–205.

[4] V. Bhosle, A. Tiwari, J. Narayan, Applied Physics Letters 88, (2006) 32106.

[5] J. M. Camacho, R. Castro-Rodr´ıguez, A. Iribarren, E. Chan y D´ıaz, A. Duarte-Moller, P. S. Santiago, International Journal of Physical Sciences 6 (2011) 6660-6663.

[6] B. E. Sernelius, K. F. Berggren, Z. C. Jin, I. Hamberg, C. G. Granqvist, Physical Review B 37, (1988) 10244-10248.

[7] B. H. Fujiwara, M. Kondo, Physical Review B 71, (2005) 075109.

[8] M. Ohyama, H. Kozuka, T. Yoko, Journal of the American Ceramic Society 81, (1998) 1622-1632.

[9] K. Y. Cheong, N. Muti, S. R. Ramanan, Thin Solid Films 410, (2002) 142-146.

[10] J. H. Lee, B. O. Park, Thin Solid Films 426, (2003) 94-99.

[11] K. Yim, H.W. Kim, C. Lee Materials Science and Technology 23, (2007) 108-112.

[12] P. K. Nayak, J. Yang, J. Kim, S. Chung, J. Jeong, C. Lee, Y. J. Hong, Journal of Physics D: Applied Physics 42, (2009) 035102.

[13] K. Yoshino, T. Hata, T. Kakeno, H. Komaki, M. Yoneta, Y. Akaki, T. Ikari, Physica Status Solidi (c) 0, (2003) 626-630.

[14] Li Yuan-Qing, Yong Kang, Xiao Hong-Mei, Ma Wang-Jing, Zhang Guang-Lei, Fu Shao-Yun Materials Letters 64, (2010) 1735–1737.

[15] J. K. Sheu, K. W. Shu, M. L. Lee, C. J. Tun, G. C. Chi, Journal of the Electrochemical Society 154 6, (2007) H521-H524.

[16] Chen Tao-Hsing, Chen Ting-You, Nanomaterials 5, (2015) 1831-1839.

[17] L. El Mir, Z. Ben Ayadi, M. Saadoun, K. Djessas, H. J. vonBardeleben, S. Alaya Applied Surface Science Journal 254, (2007) 570.

[18] J. El Ghoul, C. Barthou, M. Saadoun and L. El Mir Journal of Physics B 405, (2010) 597-601.

[19] Z. Z. Zhi, Y. C. Liu, B. S. Li, X. T. Zhang, Y. M. Lu, D. Z. Shen, X. W. Fan, Journal of Physics D: Applied Physics 36, (2003) 719.

[20] V. Gupta, A. J. Mansingh, Journal of Applied Physics 80, (1996) 1063.

[21] V. Kumar, Singh Neetu, R. M. Mehra, A. Kapoor, L.P. Purohit, H. C. Swart, Thin Solid Films 539, (2013) 161-165.

[22] H. Kim, C. M. Gilmore, A. Pique, J. S. Horwitz, H. Mat toussi, H. Murata, Z. H. Kafafi, D. B. Chrisey, Journal of Applied Physics 86, (1999) 6451-6461.

[23] T. H Flemban, M. C. Sequeira, Z. Zhang, S. Venkatesh, E. Alves, K. Lorenz, S. Iman Roqan, Journal of Applied Physics 119, (2016) 065301.
[24] J. P. Mathew, G. Varghese, Jacob Mathew, Chinese Physics B 21, (2012) 078104.
[25] M. S. Kim, K. G. Yim, J. Y. Leem et al., Journal of the Korean Physical Society 59 3, (2011) 2343–2348.
[26] B. D. Cullity, Elements of X-ray Diffraction, second ed., 1978, Addison Wesley MA, United States, (1956) 285-284.
[27] Kumar Vinod, Vijay Kumar, S. Som, A. Yousif, N. Singh, O.M. Ntwaeaborwa, A. Kapoor, H. C. Swart, Journal of Colloid and Interface Science 428, (2014) 8–15.
[28] J. Ungula, B. F. Dejene, Physica B 480, (2016) 26–30.
[29] J. Yang, M. Gao, Y. Zhang, L.Yang, J. Lang, D. Wang, H. Liu, Y. Liu, Y. Wang, H. Fan Superlattices and Microstructures 44, (2008) 137-142.
[30] K. Prabakar, C. Kim, C. Lee, Crystal Research and Technology 40, (2005) 1150-1154.
[31] Vijay Kumar, M. Gohain, S. Som, Vinod Kumar, B. C. B, Bezuindenhoudt, H. C. Swart, Physica B 480, (2016) 36-41.
[32] X. Q. Wei, B. Y. Man, M. Liu, C. S. Xue, H. Z. Zhuang, C. Yang, Physica B: Condensed Matter 388, (2007) 145-152.
[33] H. S. Kang, J. S. Kang, J. W. Kim, S. Y. Lee, Journal of Applied Physics 95, (2004) 1246.
[34] T. K. Gupta, W.D. Straub, Journal of Applied Physics 68, (1990) 845.
[35] V. A. Fonoberov, A. A. Balandin, Journal of Physics: Condensed Matter 17, (2005) 1085.
[36] T. Prasada Rao, M.C. Santhosh Kumar, Journal of Crystallization Process and Technology 2, (2012) 72-79.
[37] P. K. Samanta, S. K. Patra, A. Ghosh, P. R. Chaudhuri, International Journal of Nanoscience and Nanotechnology1, (2009) 81 – 90.
[38] J. Tauc, R. Grigorovichi, A. Vancu, Physica Status Solidi 15, (1966) 627-637.
[39] P. Duran, F. Capel, J. Tartaj, C.Moure, Advanced Materials Interfaces 14, (2002) 137.
[40] G. Xiong, U. Pal, J. Garcia Serrano, Journal of Applied Physics 101, (2007) 024317.

Chapter 7

Effect of pH on the structural, optical and morphological properties of Ga-doped ZnO nanoparticles by reflux precipitation method

7.1 Introduction

Ga-doped ZnO (GZO) nanomaterials have received significant attention in the recent years as a kind of low resistivity n-type conductor used for transparent conductive oxide applications. Among the group (III) elements, Ga is the most preferred dopant used to improve the material properties of ZnO. For example, GZO has higher stability of oxidation due to its greater electronegativity in comparison with its main competitor Al. The ionic and covalent radii of Ga are nearly equal to that of Zn [1]. Thus, Ga^{3+} can be substituted for Zn^{2+} over a larger doping range. There is, however, a charge compensation needed when Ga^{3+} replaces Zn^{2+}. This is normally done by the formation of oxygen defects. In our previous experiment, we demonstrated the superior material property of Ga doping over Al doping or combined concentrations of Ga and Al.

Many reports indicate that the pH of the reacting solutions plays a vital role in influencing the properties of nanomaterials. A strong alkaline nature of the solutions is known to enhance the structural and optical properties of the nanostructures. For instance, Sagar et al. [2] reported that the acidic nature prevents the growth of high-quality ZnO nanostructures. Sivakumara et al [3], while studying the influence of pH on ZnO nanocrystalline thin films, showed how the surface morphology improved with an increase of pH values; they reported scanning electron microscopy (SEM) images that showed less homogenous size distribution of grains for the lower pH, but distinguished and enlarged spherical morphology with self-aligned prismatic nanoparticles at higher pH values. Alias et al. [4] showed that ZnO prepared from pH 8 to 11 had good optical properties with the band

gap energy (Eg) ranging from 3.14 to 3.25 eV and the particles agglomerated when synthesized at lower pH conditions.

The precipitation reflux method of synthesis was adopted in this study because it offers several advantages which include low growth temperatures, simple equipment and it is a low-cost method. In our earlier work [5] on the synthesis of GZO NPs by reflux precipitation method, we reported improved optical and structural properties at [Ga/Zn] 2 mol% Ga. In the present study, we report on the effect of pH on the Ga/Zn sol. with the aim for further improvement of the properties of GZO NPs. We were able to produce better quality GZO NPs with high crystallinity, improved morphology, highly enhanced photoluminescence and largest band gap at pH of 5. The powders would be used to make a photo electrode seed layer for a dye-sensitized solar cell based on thin films where the improvement of conductivity and the decrease of resistivity is the main issue. To the best of our knowledge, no work on the influence of the pH of the Ga/Zn sol. on the structural, luminescence and opto-electrical properties GZO NPs by reflux precipitation method has been reported.

7.2 Experimental procedure

The chemical reagents sodium hydroxide (NaOH), zinc nitrate hexahydrate ($Zn(NO_3)_2.6H_2O$) and gallium nitrate hexahydrate ($Ga(NO_3)_3.6H_2O$) were of analytical grade and required no further purification before use.

$Zn(NO_3)_2.6H_2O$ was mixed with $Ga(NO_3)_3.6H_2O$ and dissolved in ethanol solvent to form a Ga/Zn precursor sol. with a pH value of ~1. In order to dope Ga in ZnO, we used Ga/Zn 2 mol% Ga doping concentration. To investigate the effect of nature of Ga/Zn sol. pH on the quality of the reflux precipitation derived GZO NPs, the initial pH of 1 was adjusted to 3, 5, 7, and 8 pH, by an addition of aqueous ammonia in different proportions and measured by a Hanna 211 pH meter. In the three-neck glass flask, 0.2 M zinc nitrate-gallium nitrate solution was heated, under constant stirring, to 70 °C growth temperature. 0.8 M solution of NaOH was added slowly (dropped for 60 minutes) into the flask and refluxed under continuous stirring. The suspension formed with the dropping of sodium hydroxide was stirred for two hours at the same growth temperature and the final pH measured and found to be 4, 5, 7, 8 and 10 pH for corresponding Ga/Zn sol. pH values of 1, 3, 5, 7 and 8 respectively. The solution was then allowed to stand overnight, washed several

times with deionized water and filtered. The sample was dried at 60 °C in an oven and finally ground to a fine white powder.

The crystal structures of the prepared GZO NPs were analyzed with a Bruker D8 Advance, Germany, X-ray diffractometer (XRD) with a Cu Anode X-ray tube (with a K_α radiation wavelength of 1.5406 Å). The average crystallites sizes were calculated using Scherrer's formula from the broadening of the diffraction peaks. The study of surface morphology and compositional analysis of these films was done using a scanning electron microscope (SEM) (model JEOL JSM-7800F) equipped with Oxford Aztec EDS (Energy-dispersive X-ray spectroscopy) while optical emission studies were made by photoluminescence (PL) spectroscopy performed on a Cary Eclipse fluorescence spectrophotometer (model LS-55 with a built-in 150 W xenon lamp). An Ultraviolet–visible (UV–vis) spectroscopy (Perkin Elmer Lambda 950) was used to analyze the optical properties and band gap energies of GZO NPs.

7.3 Results and discussion

7.3.1 XRD analysis

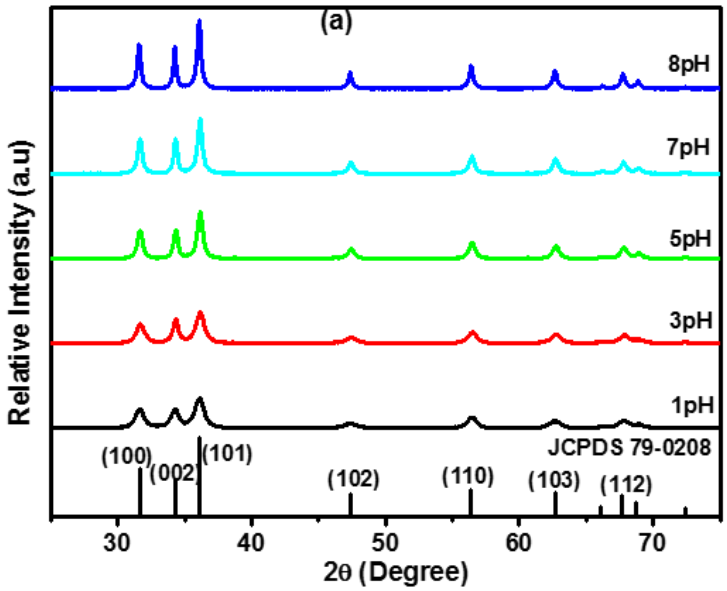

Figure 7.1: (a) X-ray diffraction patterns for GZO NPs prepared at different pH values of Ga/Zn sol.

Fig. 7.1(a) shows the XRD patterns of GZO NPs powders prepared at Ga/Zn sol. pH values of 1, 3, 5, 7 and 8. The diffraction peaks indicate the formation of a hexagonal wurtzite

structure in the ZnO powder. The wurtzite structure fitted well with the JCPDS card number 79-0208 and the precursors were decomposed completely since no peaks from impurity phases or complex products were formed. Fig. 7.1(b) shows that the diffraction peak intensities of GZO NPs increased and became narrower with an increase in pH values of the precursor solution, an indication of improved crystallinity. Since ethanol solvent itself yields a stable and clear solution to synthesize samples with fairly good material properties, the addition of aqueous ammonia to change the acidic nature of the Ga/Zn sol was certainly the reason for improved crystalline quality of GZO NPs. It was reported that Ammonia improves the stability and homogeneity of the solution by preventing uncontrolled hydrolysis. An increased basic pH releases more OH- ions into solution to provide a favorable environment to accelerate hydrolysis and nucleation so that large ZnO grains grow quickly. As such, the highest diffraction peak intensity exhibited by 8 pH sample could be as a result of the sufficient amount of OH^- available to form ZnO medium. Similarly, Znaidi et al. [6] described the significance of higher alkaline nature of solutions in enhancing the growth of ZnO crystallites through hydrolysis of salts of a weak acid in a strong base medium. Likewise, Koao et al. [7] reported that the increase in crystallite sizes with the increase in pH could be due to increased solubility of $Zn(OH)_2$ which are the primary precursor for nucleation and growth of ZnO nanoparticles. The lower pH samples (pH 1 and 3) showed the smallest peak intensity arguably as a result of high concentration of H^+ ions which could restrain grain growth.

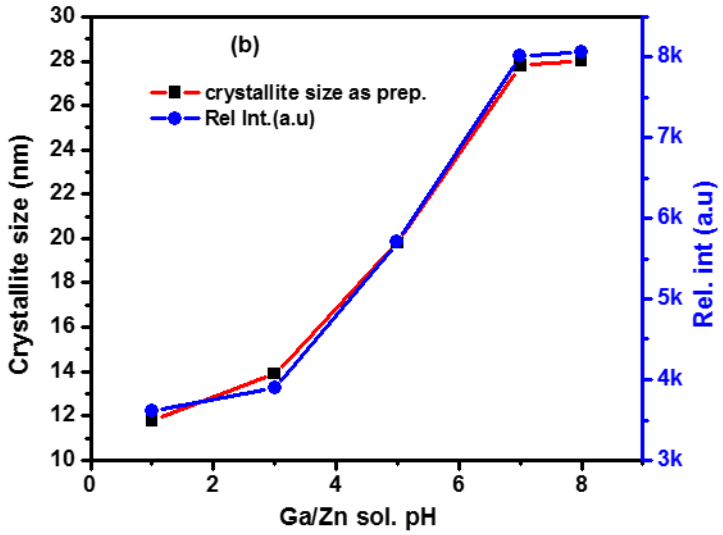

Figure 7.1: (b) Graph of the crystallite size and average relative intensities of diffraction peaks of Ga-doped ZnO NPs against different Ga/Zn sol. pH.

The average crystallite size of the GZO NPs at different Ga/Zn sol. pH conditions was calculated using the [100], [002], [101], [102], [110], [103] and [112] diffraction planes of XRD spectra by Scherrer's formula [8]. The results obtained were 12, 14, 20, 27 and 28 nm for 1, 3, 5, 7 and 8 pH respectively. From Fig. 7.1(b), it is seen that the crystallite sizes increased with the increase in pH values in the same way as the intensities of the diffraction peaks of GZO NPs. The growth sol pH of 5 is preferred due to its relatively good crystallinity and moderately small crystallite size.

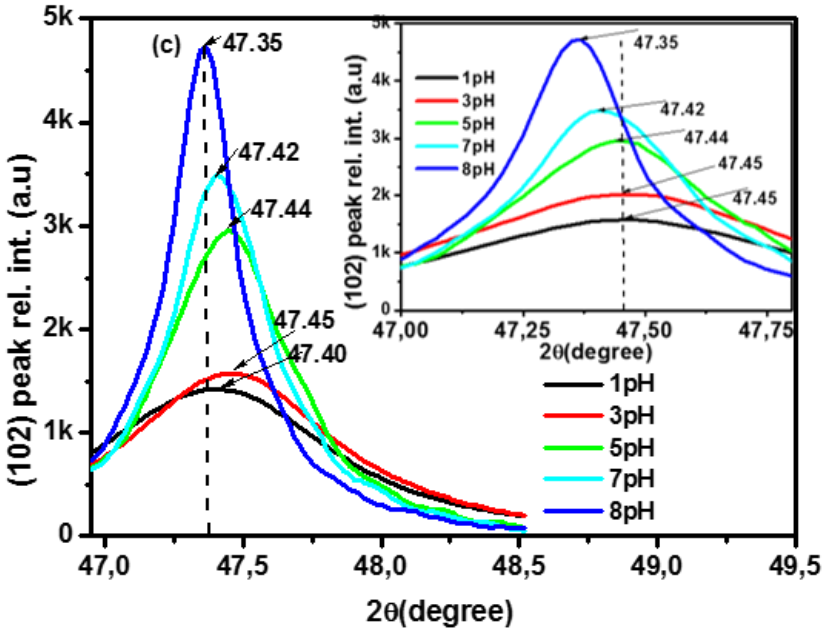

Figure 7.1: (c) Relative intensity and position shift of (102) diffraction peak of lattice planes for the GZO NPs at different pH values (inset: spectra for annealed samples).

Fig. 7.1(c) displays an enlarged XRD spectra for the diffraction plane [102] of GZO NPs at different Ga/Zn sol. pH. From this spectra, a general trend in peak position shift towards lower angles and a reduction in full-width at half-maximum (FWHM) of the peaks with the increase in pH values of the samples were observed. The shift indicates the presence of an increasing lattice strains in the GZO NPs with the increase in alkalinity of Ga/Zn sol.[9]. Fig. 7.1(c) inset, shows the spectra of (102) diffraction peaks for the samples annealed at 300 ℃ which displays a clear shift of peak position from 47.45 to 47.35° with the increase in Ga/Zn pH sol.

The numerical values of the lattice parameters for the GZO NPs were calculated from the prominent diffraction peaks of the XRD spectra according to relation in ref. [10] and displayed in Fig. 7.1(d). It was observed that the average lattice parameters 'a' and 'c' of GZO NPs diffraction planes increased continuously with increasing pH values. The changes

in lattice parameters is mainly attributed to impurities, lattice defects or vacancies introduced during preparation procedure. In our case, the increase in the strain is apparently due to the structural defects in the lattice with increased pH of the solution as shown by PL results. It could also be noted that the growth of the particles are more prominent in the 'c' direction as suggested by a larger change in 'c' lattice parameter when compared with 'a' lattice parameter.

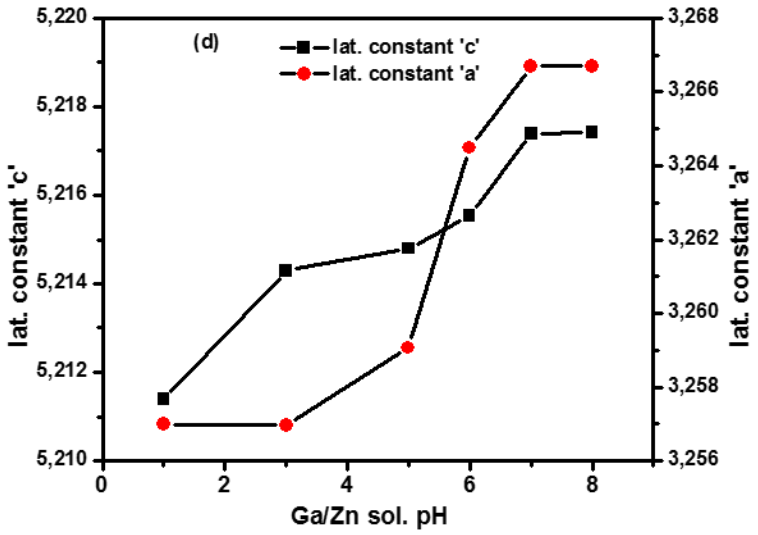

Figure 7.1: (d) Average lattice constants 'a' and 'c' Ga-doped ZnO NPs at different pH values of Ga/Zn sol.

7.3.2 SEM and EDS analysis

Fig. 7.2 shows SEM micrographs of the surfaces of GZO NPs at 3, 5 and 8 pH values of Ga/Zn sol. The SEM images showed agglomerated tiny rods that formed on big slabs of nanorods in the acidic condition (3 pH), whereas enlarged and relatively dispersed nanospherical particles could be seen at a pH of 5. At the pH of 8 even bigger and well dispersed nanospherical particles consisting of agglomerated nanocrystallites were observed as shown by the particles in the encircled area. Instances of strong agglomeration of the nano-grains could be seen at pH 8 as shown by the nanospherical balls. Agglomerated GZO NPs with less surface roughness and with a good homogeneous nanostructure were envisioned as the pH was increased to alkaline conditions (pH 8). The improvement in grain size is a clear indication of how the NPs are strongly affected by the pH of the precursor solution. Jeon et al. [11] also reported the formation of NPs with an ideal spherical morphology, at increased pH, which is more advantageous at increasing packing densities than irregularly shaped particles formed at lower pH conditions.

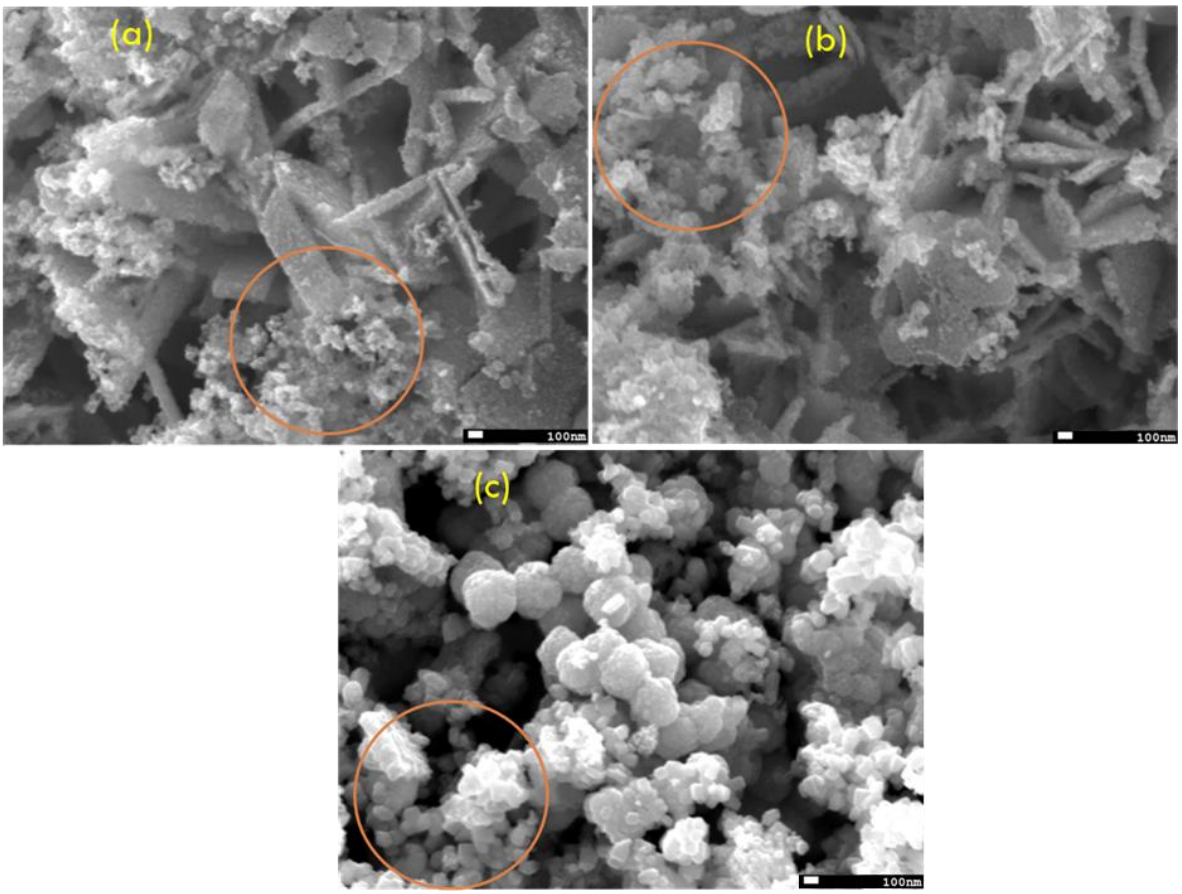

Figure 7.2: SEM micrographs of the Ga-doped ZnO NPs at (a) 3 pH (b) 5pH and (c) 8 pH values of Ga/Zn sol.

The chemical composition of the GZO NPs powders synthesized at 3, 5 and 8 pHs (Fig. 7..3) was verified using EDS analysis to ascertain the phase purity of the samples as depicted by XRD results. The only peaks present were those corresponding to Zn, Ga, and O in all the samples. Moreover, the weight % ratio of Zn/O and Zn/Ga were observed to increase from 3.2 to 3.9 and 6.7 to 15.8 respectively, with increasing pH values of Ga/Zn sol. This linear relation of Zn/O and Zn/Ga ratio suggests the great convenience to achieve control of the compositions of the GZO samples as desired for the intended application.

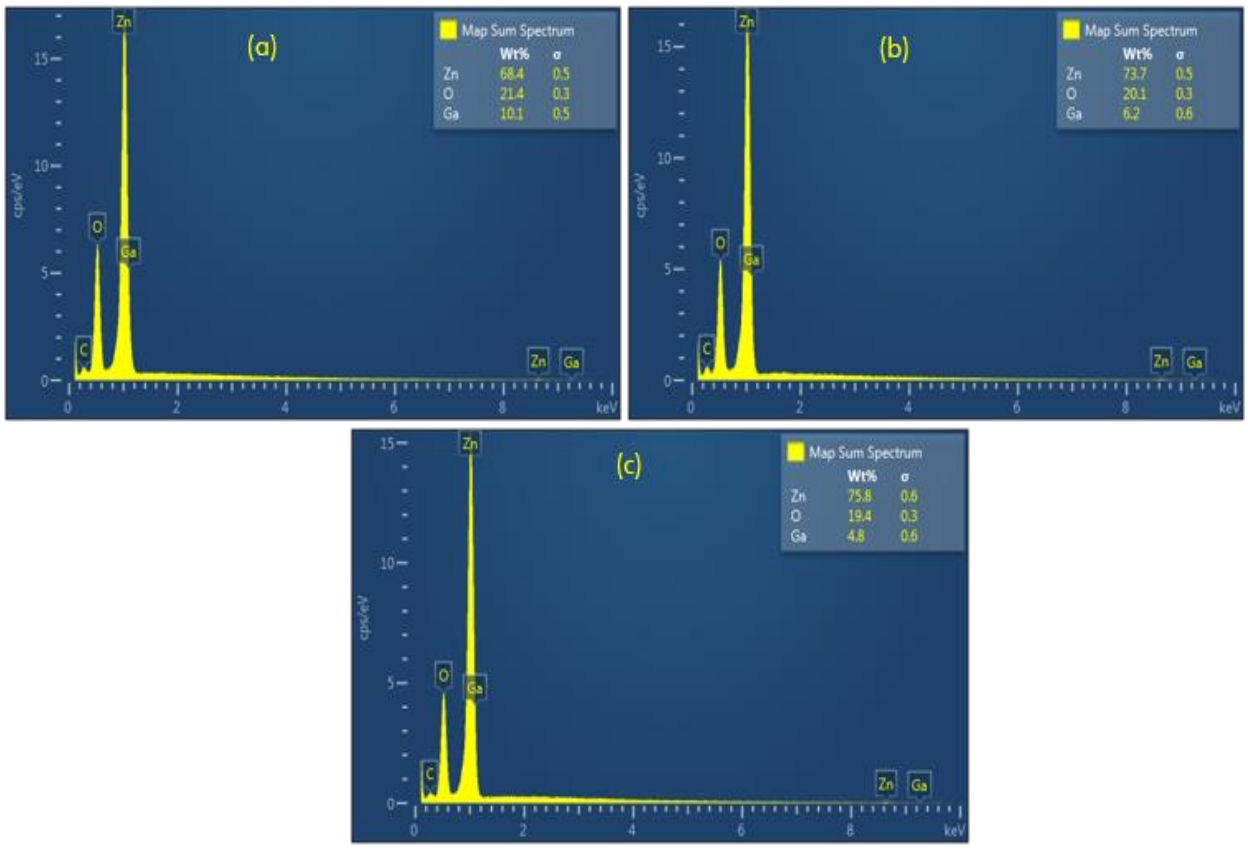

Figure 7.3: EDS spectra of GZO NPs synthesized at (a) 3 pH (b) 5 pH and (c) 8 pH values of Ga/Zn sol.

7.3.3 Photoluminescence and catholuminescence analysis

Fig. 7.4(a) shows the room temperature PL emission spectra of the GZO NPs prepared using Ga/Zn sol. at pH values of 1, 3, 5, 7 and 8. The sharp and strong UV NBE, corresponding to band-edge emission, that formed between 380 and 390 nm originated from the free exciton recombination of GZO NPs. While the visible emission peaks around 550 nm are assigned to deep level defects (DLE) emissions associated with the presence of defect centers such as oxygen vacancies and zinc interstitials which act as donor levels located below conduction band edge [12]. The PL spectra display an increase in exciton peak emission to a maximum at 5 pH and then decrease at the higher pH condition with the increase in pH values as illustrated by Fig. 7.4(b). This presence of enhanced peak intensity, sharp and well-defined UV emission peak clearly indicates the superior quality of GZO NPs at 5 pH of Ga/Zn sol. The decrease in exciton peak intensities after 5 pH could be due to the depletion of the grains with the increase in pH behavior, which played a major role in increasing defect

densities [13, 14] as shown in Fig. 7.4(a) by a prevalent and increasing DLE emission peak intensity at higher pH levels. The increase in particle size with the increase in pH values discussed earlier is understood to increase the volume ratio of bulk to depletion region and cause the intensity of non-radioactive recombination to increase.

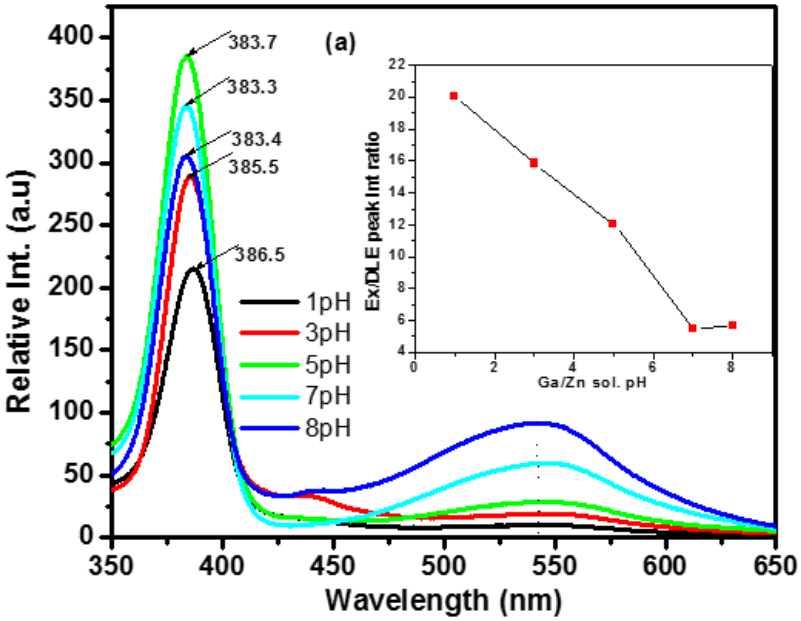

Figure 7.4: (a) PL emission spectra and Inset: Exc. /DLE peak intensity ratios for of GZO NPs at different pH values of Ga/Zn sol.

Fig. 7.4(b) also demonstrates the blue shift of the exciton peak positions with the increase in Ga/Zn sol. pH albeit very minimal changes in the shift after 5 pH. It is not clear, the exact cause of the blue shift of the PL emission peaks with increasing pH, yet the crystallite sizes increase. However, it could indicate that the Ga species in the ZnO lattice should have acidic sites relevant to the blue emission because the PL emissions is quenched at higher pH levels as the Ga content reduces in the lattice. Minor peaks at around 440 nm could also be seen in some samples in the spectra Fig. 7.4(a). The blue emission is thought to originate from the defect emission of oxygen vacancies [15].

The concentration of structural defects and quality of GZO NPs were determined from the ratio of PL UV emission (I_{UV}) to deep-level emission intensity (I_{DLE}). From the inset Fig 7.4(a), the relative I_{UV}/I_{DLE} ratio of our samples was found to gradually decrease with the increase in corresponding pH values of Ga/Zn sol. This gradual decrease in the ratio can be attributed to increased concentration of structural defects like oxygen vacancies and zinc interstitial or stress that lead to the diffusion of GZO NPs at higher pH conditions. As such,

the pH 5 sample has a relatively higher peak intensity ratio and therefore better optical properties due to higher crystal quality and low defects than 8 pH sample.

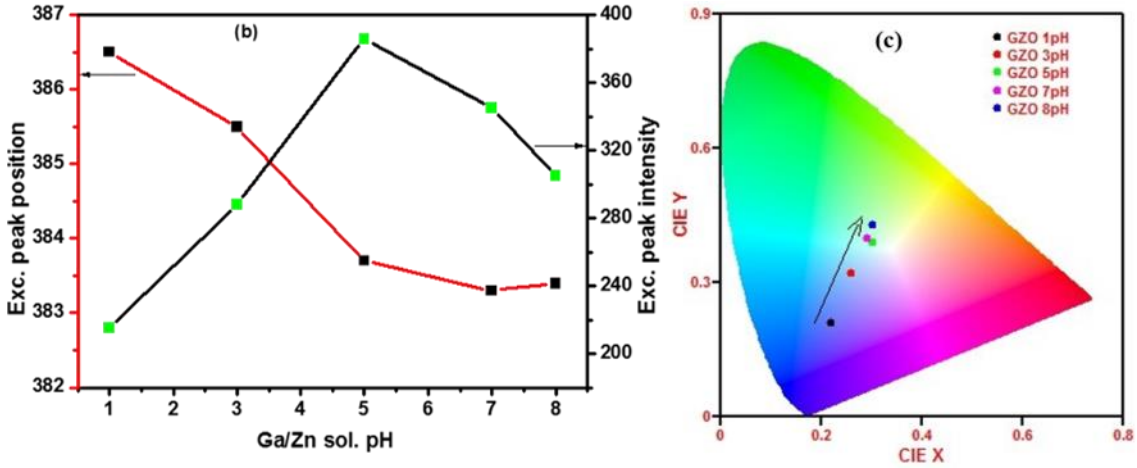

Figure 7.4: (b) Graph of change in peak position and intensity of PL exciton emission (c) CIE spectra of GZO NPs at different pH values of Ga/Zn sol.

The CIE chromaticity of PL spectra (Fig. 7.4c) of GZO NPs depicts a linear shift of the co-ordinates from deep blue to light blue of the CIE map, with the increase in pH values. The shift of the co-ordinates, indicated by the arrow, was also supported by the PL emission spectra wavelength shifts.

Fig. 7.5(a) shows the room temperature cathodoluminescence (CL) spectra of GZO NPs at 3, 5 and 8 pH values of Ga/Zn sol. The figure exhibits an increase in counts/s of CL emissions and shifts to smaller wavelength in peak positions with the increase in pH values in close agreement with the PL emission results. Fig. 7.5(b) also demonstrates the decrease in peak full width at half maximum (FWHM) with increased pH.

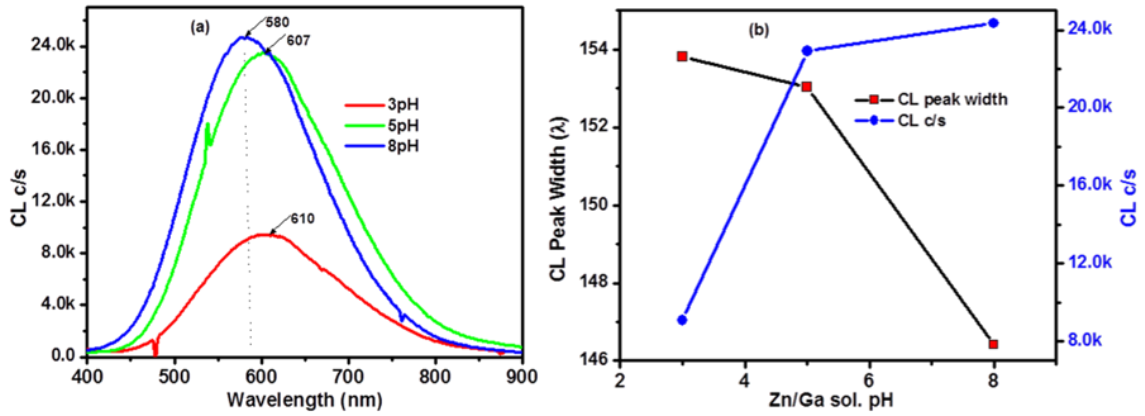

Figure 7.5: (a) CL spectra of GZO NPs at 3, 5 and 8 pH values of Ga/Zn sol and (b) illustration of changes in CL intensities(c/s) and FWHM with the increase in pH values.

7.3.4 Optical properties

Fig. 7.6(a) shows the optical reflectance spectra of GZO NPs prepared at different Zn/Ga sol. pH. The % R was observed to increase with the increase in pH values. This can be ascribed to a slight decrease in surface roughness and the formation of larger particles on the surface of GZO NPs with the increase of pH values which causes scattering of light. The blue shift of the absorption edge of the GZO NPs with the increase in pH values follows the blue-shift in PL emission attributed to the crystal field due to the changes in the structure of the samples as the pH condition of solutions change.

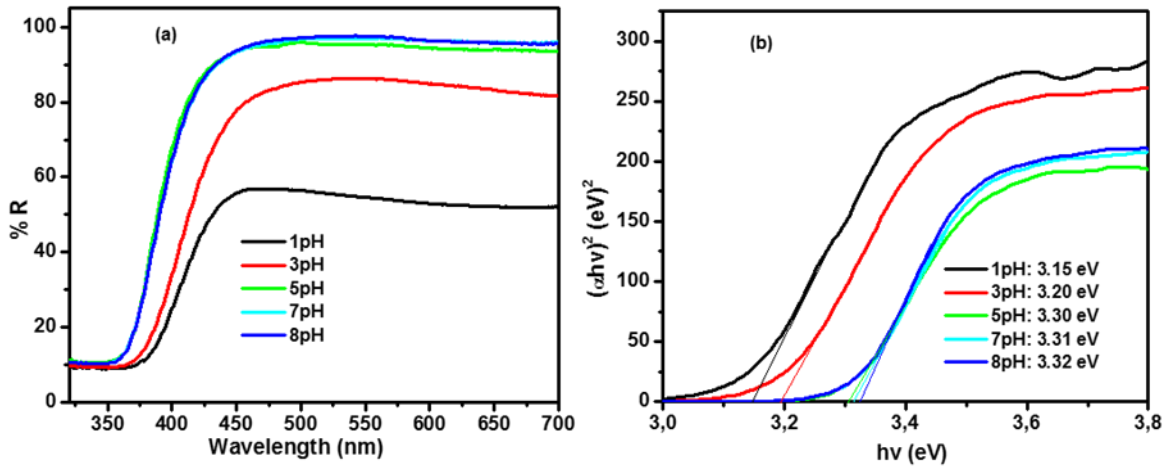

Figure 7.6: (a) UV-Vis % reflectance spectra and (b) Band gap energy plot of GZO NPs at 1, 3, 5, 7 and 8 pH values of Ga/Zn sol.

Fig. 7.6(b) shows the optical band gap of GZO NPs calculated using the common Kubelka Munk's equation. The optical band gap energies (Eg) (eV) of GZO NPs were estimated from the x-axis intercept of the extrapolated linear portion of $(\alpha h\nu)^2$ versus $h\nu$ plot. For the allowed direct transition, the variation in α with photon energy ($h\nu$) obeys Tauc's plot method, according to the following equation [16].

$$(\alpha h\nu)^2 = A(h\nu - Eg) \tag{7.1}$$

where A is a constant, Eg is optical band gap, h is plank constant and α is the absorption coefficient. It can be seen from the graph that plot of $(\alpha h\nu)^2$ versus $h\nu$ yields a reasonably good straight line fit to the absorption edge of GZO NPs and the extrapolation $h\nu$ at which

$\alpha^2 = 0$. The band gap of GZO NPs increased significantly from 3.15 to 3.30 eV for the increase in pH from 1 to 5 pH. However, further increase in Ga/Zn sol. pH to 8 yielded no appreciable change in band gap in agreement with the % R results which showed a very minimal blue shift in absorption edge after 5 pH. This marginal difference in band gap energy for pH 5, 7 and 8 pH could be attributed to lack of substantial structural modification of GZO NPs which may occur over this range of pH.

The blue shift in band gap with the increase of pH values is a clear signature of nanostructure formation and may be attributed to the quantum size effect [17] which could be as a result of the changes in particle sizes which influence the ability of GZO NPs to absorb or reflect UV light. The trend was confirmed by the corresponding blue shift of PL emission peaks which also shows a marginal change in peak positions after 5 pH. This kind of behavior of the increase in band gap with the increase in particle size or vice versa was also observed in some of our previous experiments [18], even though, it is generally accepted that the semiconductor nanoparticle energy gap decreases with increasing crystallite size [19]. Nevertheless, the band gap energy red-shifted with the increase in particle sizes when GZO NPs samples were annealed at 300 ºC. The observed increase in band gap with increased particle size may be as a result of hydrated GZO nanoparticles. From the first principle it is inferred that when a ligand such as water chelates to a metal center like Zn it results to splitting of d orbitals and subsequent increase in the band gap between combined molecular orbitals. The larger the surface area of the crystallites, the more water molecules would be adsorbed on to the surface and so the greater the orbital splitting and the extent of the blue-shift. Consequently, the band gap energy of the NPs was observed to decrease with the increase in crystallite sizes when annealed at 300 ºC. Since annealing process removes the hydration of the NPs. Another possible explanation for the increase in band gap with an increased in particle size is due to the higher concentration of the oxygen vacancies in the small crystallite size compared to the ones with the large crystallite size. Generally, the samples prepared at the lower pH of Ga/Zn sol. exhibited higher blue PL emissions peaks, Fig. 7.4a, which originate from the defect emission of oxygen vacancies. However, further experiments are needed in order to provide a more precise explanation for this anomaly. This tunable band gap property of GZO NPs makes it an appropriate material for solar cell applications. The most appropriate parameter for the application of GZO NPs to optoelectronics is the large Eg, which varies from 3.0 to 3.4 eV at room temperature [20]. For example, ZnO with Eg value 3.2 eV have been used as

working electrode for DSSC and recognized as a potential material to substitute TiO_2 based DSSC working electrode [21, 22].

Conclusions

Gallium-doped ZnO nanoparticles have been successfully synthesized by the reflux precipitation technique at Zn/Ga sol. pH values of 1, 3, 5, 7 and 8. All of the samples have good structural, morphological and optical properties. The XRD patterns showed crystalline NPs with hexagonal structure. The diffraction peaks intensities and crystallite sizes of GZO NPs increased with increasing pH values. The increase in pH value (acidic to alkaline) of the sols resulted in the growth of GZO NPs with improved crystallinity, smooth microstructure and large grain size. All the samples exhibited relatively high reflectance (86%) in the visible region of the solar spectrum. The influence of nanocrystallinity can be seen in the band gap enhancement of the nanoparticles where the values increased from 3.15 to 3.32 eV with increasing pH values. The sample prepared at Ga/Zn sol. value of 5 pH proved most suitable to make thin films with fairly good material properties for use as a photo anode in DSSCs. Because, the 5 pH sample presented a high crystallinity, less tensile strain, most intense PL exciton emission, relatively larger I_{UV}/I_{DLE} PL ratio, the moderately small crystallite size of 17 nm and an adequately enhanced band gap of 3.3 eV.

References

[1] P. K. Nayak, J. Yang, J. Kim, S. Chung, J. Jeong, C. Lee, Y. Hong, J. Phys. D: Appl. Phys. 42, (2009) 035102

[2] P. Sagar, P. K. Shishodia, R. M. Mehra, Applied surface science 253, 12 (2007) 5419-5424.

[3] K. Sivakumar, V. S. Kumar, N. Muthukumarasamy, M. Thambidurai, T. S. Senthil, Bulletin of Materials Science 35, 3 (2012) 327-331.

[4] S. S. Alias, A. B. Ismail, A. A. Mohamad, Journal of Alloys and Compounds 499, 2 (2010) 231-237.

[5] J. Ungula, B. F. Dejene, H. C. Swart, Results in Physics, (2017) 2022–2027.

[6] L. Znaidi, GJAA Soler Illia, S. Benyahia, C. Sanchez, A. V. Kanaev, Thin Solid Films 428, 1 (2003) 257-262.

[7] L. F. Koao, F. B. Dejene, H. C. Swart, SA Institute of Physics proceedings ISBN: 978-0-620-70714-5

[8] J. P. Mathew, G. Varghese, J. Mathew, Chinese Physics B 21, 7 (2012) 078104.

[9] G. G. Rusu, A. P. Rambu, V. E. Buta, M. Dobromir, D. Luca, M. Rusu, Materials Chemistry and Physics 123, 1 (2010) 314-321.

[10] V. Kumari, Vinod Kumar, B. P. Malik, R. M. Mehra, Devendra Mohan. Optics Communications 285, 8 (2012) 2182-2188.

[11] B. S. Jeon, G. Y. Hong, Y. K. Yoo, J. S. Yoo, Journal of the Electrochemical Society 148, 9 (2001) 128-131.

[12] D. M. Bagnall, Y. F. Chen, Z. Zhu, T. Yao, M. Y. Shen, T. Goto, Applied Physics Letters 73, 8 (1998) 1038-1040.

[13] H. S. Kang, J. S. Kang, J. W. Kim, S. Y. Lee, Journal of Applied Physics 95, 3 (2004) 1246-1250.

[14] T. K. Gupta, W. D. Straub, Journal of applied physics 68, 2 (1990) 845-850.

[15] X. Q. Wei, B. Y. Man, M. Liu, C. S. Xue, H. Z. Zhuang, C. Yang, Physica B: Condensed Matter 388, 1 (2007) 145-152.

[16] J. Tauc, R. Grigorovichi, A. Vancu, Phys. Status Solidi 15, (1966) 627-637.

[17] Vij, Ankush, S. Gautam, R. Kumar, A. K. Chawla, R. Chandra, N. Singh, K. H. Chae, Journal of Alloys and Compounds 527, (2012) 1-4.

[18] J. Ungula, B. F. Dejene, Physica B: Condensed Matter 480, (2016) 26-30.

[19] S. U. Shaikh, D. J. Desale, F. Y. Siddiqui, A. Ghosh, R. B. Birajadar A.V. Ghule, R. Sharma, Materials Research Bulletin 47, (2012) 3440–3444.

[20] S. J. Pearton, D. P. Norton, K. Ip, Y. W. Heo, T. Steiner, Progress in materials science 50, 3 (2005) 293-340.

[21] G. Boschloo, T. Edvinsson, A. Hagfeldt, Dye-sensitized nanostructured ZnO electrodes for solar cell applications. Elsevier BV: Amsterdam, The Netherlands, 2006.

[22] Vinod Kumar, S. K. Swami, Anuj Kumar, O.M. Ntwaeaborwa, V. Dutta and H.C. Swart, Journal of Colloid and Interface Science 484, (2016) 24–32.

Chapter 8

Structural, morphological and optical properties of ZnO nanorods grown on Ga-doped ZnO seeded thin film layer from aqueous solution: The role of CBD precursor concentration

8.1 Introduction

One of the recent major researches in nanotechnology focuses on the device application of one-dimensional (1D) ZnO nanostructures [1–3]. The ZnO nanostructures have attracted profound interest in academic and industrial applications for their ease of synthesis and promising building blocks for other structures [4, 5]. They have potential applications in polymer-based and dye sensitized solar cells (DSSCs) [6], light emitting diodes [7] and chemical sensors [8]. Among these applications, well-aligned ZnO nanorods (ZNRs) are suitable for use in DSSCs for two main reasons. Firstly, ZNRs provide larger surface areas than bulk ZnO and ZnO films [9] required to provide anchoring sites for dye. Secondly, ZNRs provide direct conduction pathway for charge transfer from the position of electron-hole pair generation to the collecting electrode [10].

Since various characteristics such as diameter, the length, and alignment of ZNRs are known to significantly affect the performance of DSSCs, many studies aim to control these parameters to engineer desired device properties [11]. To this end, ZNRs can be grown independently or grown on pre-seeded substrates. For instance, Vayssieres et al. [12] reported a successful growth of ZNRs on un-seeded substrates from the solution of $Zn(NO_3)_2$ and methenamine while Zhao et al. [13] described that no nanorods of ZnO were observed on bare glass or ITO slides in solution of $Zn(NO_3)_2$ and NaOH. Yang et al. [14] who conducted the comparisons between the ZNRs grown on the bare and the pre-treated substrate concluded that pre-treated substrate produced the as-prepared ZNRs with better alignment. Additionally, doping of ZNRs during growth [15, 16] has been used as a means to control the characteristics of ZNRs as well as to improve their optoelectrical properties

[17]. It is conveyed that the conductivity of ZnO nanostructures is significantly increased by doping with Group III elements due to their relatively low ionization energy [18]. In this regard, Ga-doped ZnO (GZO) is preferred for use as TCO seed layer for various reasons which include its stability with respect to oxidation in comparison with aluminium and closeness of the ionic and covalent radii of Ga to that of Zn [19]. However, controlling the ZNRs by doping into the seed layer has not been widely studied yet. Thus, we fabricated well-oriented crystalline ZNRs on a pre-seeded Ga-doped ZnO layer by a two-step process which involves the pretreatment of the substrates and growth of the NRs using the chemical bath deposition (CBD) technique. The CBD method is used in this study because of its cheapness, simplicity, scalability and can be done at low temperature (60–100 ℃). Besides, in the recent time, CBD method has yielded a fruitful approach in the growth of ZNRs arrays on the pre-treated substrate [20, 21]. In CBD, the crystal morphology and orientation of ZnO crystallites are strongly influenced by experimental conditions such as growth pH, growth concentration, and the level of supersaturation, the temperature and the nature of the substrate [22]. As such, the control of these parameters remains a necessity for the formation of high surface area nanomaterials for use in photovoltaic and optoelectronic devices.

Most research, report on the growth of ZNRs on ZnO seeded substrates under various CBD growth parameters, but the growth of ZNRs on GZO seeded substrates is rarely reported. Actually, the effect of different precursor concentration of $Zn(NO_3)_2$]/[$C_6H_{12}N_4$ on the material properties of ZNRs prepared by the CBD on glass substrates pre-seeded with an optimized layer of GZO is reported for the first time in this investigation. We believe the results of this study will advance the understanding of the properties of ZNRs grown on GZO transparent conductive films, which together would provide a promising combination for the fabrication of photoelectrode components of DSSC because of aforementioned benefits of ZNRs and the fact that GZO films do also act as transparent electrodes.

8.2 Experimental procedure

The chemical reagents used, sodium hydroxide (NaOH), zinc nitrate hexahydrate ($Zn(NO_3)_2$. $6H_2O$, 99.9% purity), methenamine ($C_6H_{12}N_4$, 99.9% purity) and gallium nitrate hexahydrate ($Ga(NO_3)_3.6H_2O$, 99.9% purity) were of analytical grade and thus required no further purification. Double distilled water was used to prepare all aqueous solutions. The details of synthesis process of nanorods using the two-step CBD growth method are described as follows.

Figure 8.1: Schematic diagram showing a two-step CBD growth of ZNR arrays on the GZO seeded glass substrate.

Fig. 8.1 is a schematic diagram showing the two-step chemical bath deposition method, i.e. deposition of GZO seed layer on a glass substrate by spin coating followed by growth of ZNRs on the seeded substrate by the CBD at different growth concentrations.

Firstly, GZO seed particles were deposited on a glass substrate using the spin coating technique. Prior to deposition, the glass substrates were cleaned for 30 minutes in a mixture of acetone and methanol in an ultrasonic cleaner and then for 5 minutes each in ethanol and distilled water and finally dried using high-pressure N_2 gas blowing. The coating solution was prepared from as-synthesized GZO nanopowders. The details of preparation and optimization of GZO nanopowders were described in Ref. [23]. The GZO powder was ground, dissolved in suitable solvent and mixed into a homogenous paste to form the spin coating solution. The solution was spin-coated onto the glass substrates using a SPEN 150 spin coater at the rate of 2000 rev/min for 30 s. The as-deposited films were immediately pre-annealed on a hot plate at 250 ℃ and for 10 min. To obtain an appropriate thickness and complete coverage of the GZO seed layer the deposition and preheating procedures were repeated 10 times. Thereafter, the GZO films were post-annealed in the air to 500 ℃ from RT, held at 500 ℃ for 120 min, and cooled in a furnace to RT. This was necessary to improve the adhesion of the seed layer to the substrate so as to achieve a well-aligned and vertical growth of ZNRs in the following processes.

In the second step, the ZNRs were grown from the GZO seeds by immersing the seed-coated substrates in the reaction bath of an aqueous precursor solution. The reaction bath solution was prepared as follows: An equimolar solutions of Zn $(NO_3)_2$). $6H_2O$ and hexamethylenetetramine (HMTA) were dissolved separately in 30 ml distilled water, mixed under continuous stirring for 2 hrs at room temperature and 10 ml of distilled water added to make a 70 ml solution in a100 ml beaker reaction vessel. The reaction vessel containing the reaction bath and the suspended glass substrate seeded with the GZO film was then placed in a water bath. For optimization of the growth concentration in the CBD set up, the precursor concentration was varied from 0.005-0.1 M. The GZO seeded thin film was kept

suspended in the aqueous solution at 90 ℃ in a thermostatically controlled bath for 90 min under continuous stirring in the sealed beaker reaction vessel. Finally, the thin film was removed from the solution, rinsed with double-distilled water to remove the residual salts and then dried in an oven at 70 ℃ for about 5 min.

The crystal structures of the ZNRs were analyzed using an X-ray diffraction (XRD) Model Philips Bruker D8 Advance, Germany, X-ray diffractometer (XRD) with a Cu Anode X-ray tube (with a Kα radiation wavelength of 1.5406 Å) over the 2θ range of 20-80 ℃ at a scan rate of 0.02 °/s. The surface morphology compositional analysis of the ZNRs was studied using scanning electron microscope (SEM) model JEOL JSM – 7800F equipped with Oxford Aztec EDS (Energy-dispersive X-ray spectroscopy). An atomic force microscopy (AFM) model Shimadzu SPM – 9600 was used to characterize the surface morphology of the samples. The root mean square (RMS) surface roughness was using the commercial software installed on the AFM system. The optical properties and band gap energies of GZO NPs were analyzed using Ultraviolet–visible (UV–vis) spectroscopy (Perkin Elmer Lambda 950) in the 300–600 nm wavelength range. The optical emission studies were made by photoluminescence (PL) spectroscopy performed on a Cary Eclipse fluorescence spectrophotometer; model LS-55 with a built-in 150 W xenon flash lamp as the excitation source and a grating to select a suitable excitation wavelength.

8.3 Results and discussion

8.3.1 XRD analysis

Fig. 8.2(a) shows the XRD spectra of the ZNRs grown on the GZO NPs seeds prepared at 0.005, 0.01, 0.03, 0.05, 0.07 and 0.1M growth concentrations when the growth time was 90 min. The observed diffraction peaks can be indexed to the hexagonal wurtzite structure (JCPDS card No. 75-1526, a = 3.220 nm, and c = 5.200 nm) of ZnO, corresponding to the [100], [002], [101], [102], [110], [103] and [112] planes. Not any characteristic peaks of other new phase or impurities was detected, which indicates that all the ZnO nanostructures are single hexagonal wurtzite ZnO phase and have a high degree of crystallization.

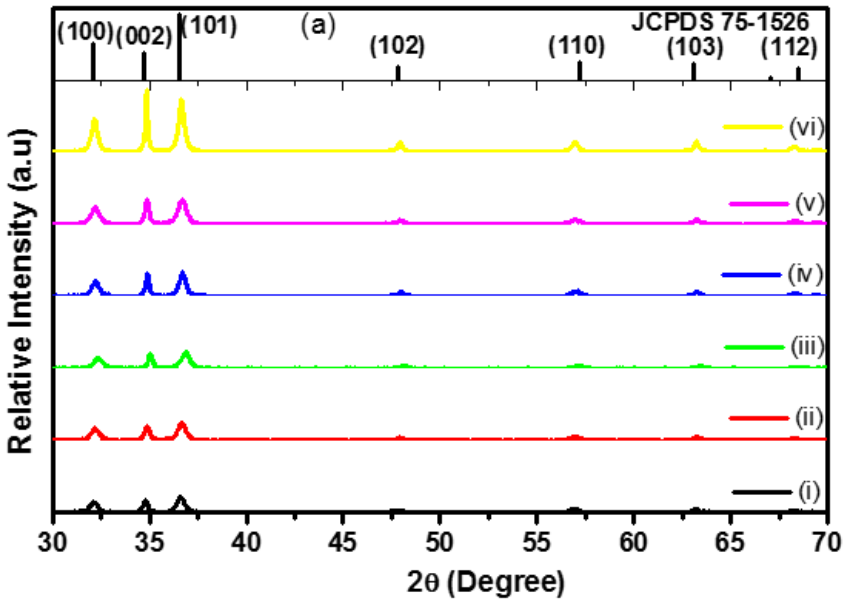

Figure 8.2: (a) XRD patterns of ZNRs on GZO seeded glass substrate in an equimolar precursor solution at different molar concentrations (i) 0.005 (ii) 0.01 (iii) 0.03 (iv) 0.05 (v) 0.07 (vi) 0.1 M.

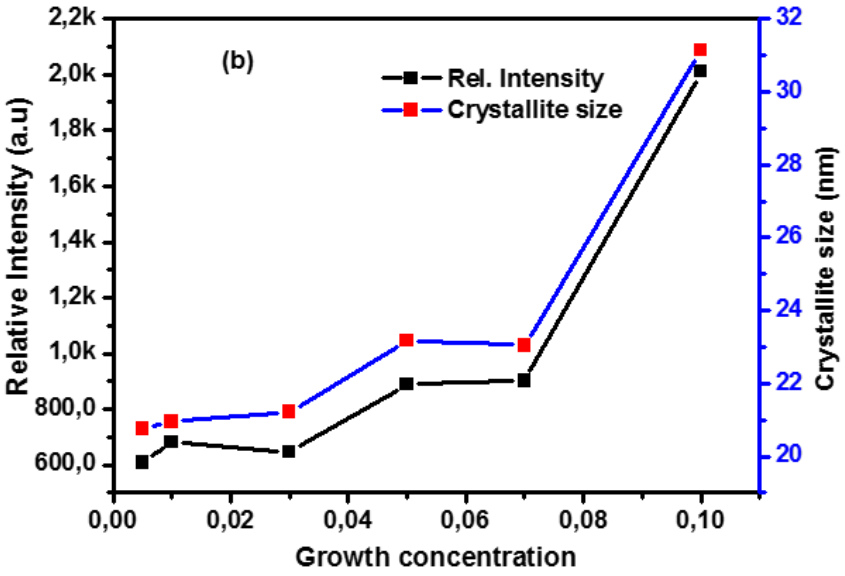

Figure 8.2: (b) Graph of the crystallite size and average relative intensities of diffraction peaks of ZNRs against different growth concentrations.

Fig. 8.2(b) shows that the diffraction peak reflection intensity of the ZNRs increased consistently with the formation of ZNRs crystallites as the growth concentration increased, an indication of improved crystallinity. However, as expected, the full-width at half-maximum (FWHM) of the diffraction peaks were observed to get smaller with the increase in concentration. The crystallite sizes of the ZNRs were determined by Scherrer's formula [24], using the FWHM values of the prominent peaks. The crystallite size values were 20.7, 20.9, 21.2, 23.2, 23.1 and 31.1 nm for 0.005, 0.01, 0.03, 0.05, 0.07 and 0.1 M growth concentrations respectively.

Importantly, the [002] intensity was greatly enhanced with the increase in growth concentrations relative to the [100] and the usual [101] maximum reflection in the standard pattern of the ZnO, which demonstrates that the ZNRs prefer to grow along the c-axis of the wurtzite structure as usually observed for ZNRs [25-26]. When the growth starts, the [101] surface face grows the fastest, as the growth progresses, the [002] surface grows faster at the expense of the [101] surface due to higher rates of deposition and growth along the c plane resulting to reduced growth along the [101] orientation and corresponding increase in the [002] orientation [27]. Yang et al. [28], explained that the suitable growth of nanorod would be along the c-axis direction on the basis of competition and optimization rules because when it grows along a different direction it will easily be obstructed by other nanorods due to the higher density during the growth process.

The relative intensity ratio between the [002] and [101] planes are commonly used to characterize the orientation of the ZNRs. Thus, the degree of c-orientation described by the relative texture coefficient was calculated using the expression [29].

$$TC_{(002)} = I_{002}/(I_{(100)} + I_{(002)} + I_{(101)} + I_{(102)} + I_{(102)} + I_{(102)} + I_{(102)}) \quad (8.1)$$

$$TC_{(101)} = I_{101}/(I_{(100)} + I_{(002)} + I_{(101)} + I_{(102)} + I_{(102)} + I_{(102)} + I_{(102)}) \quad (8.2)$$

Where $TC_{(002)}$ is the relative texture coefficient for the [002] diffraction plane and $I_{(100)}$, $I_{(002)}$, $I_{(101)}$, $I_{(102)}$, $I_{(110)}$, $I_{(103)}$ and $I_{(112)}$ are the measured diffraction intensities due to [100], [002], [101], [102], [110], [103], and [112] planes respectively.

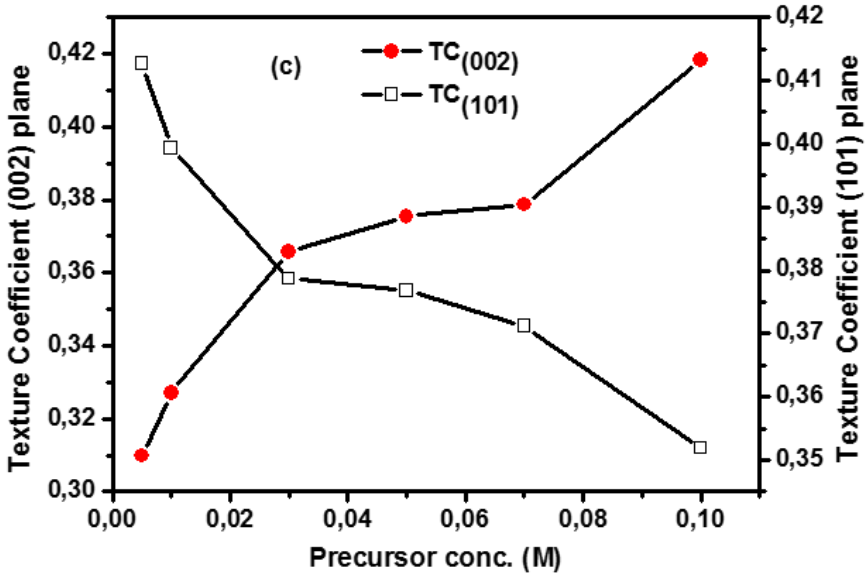

Figure 8.2: (c) Texture coefficients of [002] and [101] planes of ZNRs arrays as a function of precursor concentrations.

Hence, the calculated values of $TC_{(002)}$ are 0.309, 0.327, 0.366, 0.375, 0.379, and 0.418 for various growth concentrations ranging from 0.005 - 0.1 M as illustrated in Fig. 2(c). Similarly, the results of $TC_{(101)}$ are 0.413, 0.399, 0.379, 0.377, 0.371 and 0.352 for the concentrations from 0.005 - 0.1 M. This result indicates that the ZNRs growth was more along the [002] direction since the diffraction peaks [100] and [101] counterparts deteriorated with the increase in growth concentration in conformity with the PL DLE results. Additionally, the [002] preferred orientation and the crystallite sizes were found to have a strong correlation since both depicted an increasing trend with the increase in growth concentrations.

An appreciable peak shift to lower 2θ angle was observed in the [100], [002], [101], [102] ,[110], [103], and [112] diffraction planes of the ZNRs. For instance, from Fig. 2(d), with increasing growth concentration the [002] peak was shifted to a lower angle side toward the ideal 2θ value for the wurtzite bulk ZnO (2θ = 34.42°) implying that that the lattice constants increased with increasing the growth concentration.

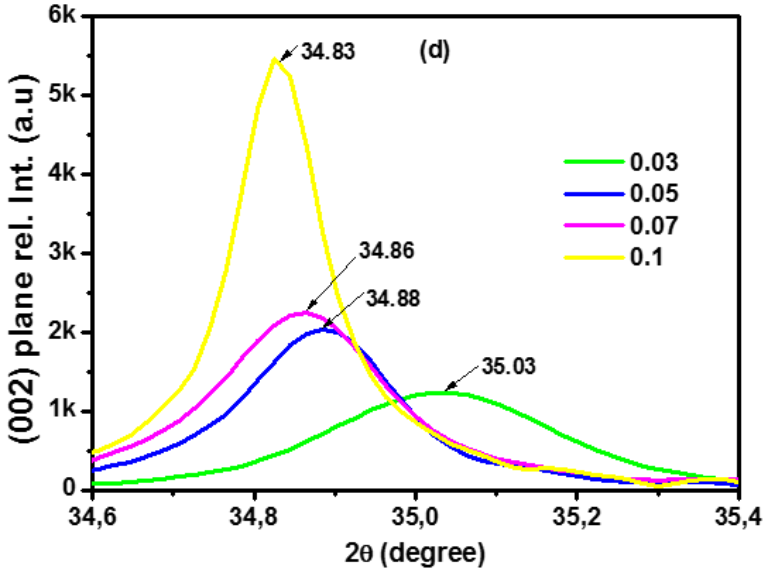

Figure 8.2: (d) Relative intensity and position shift of [002] diffraction peak of lattice planes for the ZNRs at different growth concentrations.

To verify the increase in lattice constants of the ZNRs, their numerical values were calculated from the prominent diffraction peaks of the XRD spectra according to the relation in ref [30]. For the [002] plane, the lattice constants (a, c) were found to be (3.192, 5.1197), (3.2069, 5.1408), (3.2083, 5.1441) and (3.2119, 5.1481) for the varied growth concentrations of 0.03, 0.05, 0.07 and 0.1 M respectively. As could be seen, the lattice

constants increased continuously with the increase in growth concentration. The higher value of c reveals that the unit cell of the ZNRs was elongated along the growth direction. Similarly, it can also be deduced that since the lattice constant values of the ZNRs are lower in comparison to the ideal c value of bulk ZnO (c_{bulk} = 5.204 Å) the crystallites may be under some strain [31].

Therefore, the microstrain value (ε) within the structure of ZNRs was calculated using the following relation [32]:

$$\varepsilon = \frac{\beta \cos\theta}{4} \tag{8.3}$$

Where, θ is the diffraction angle and β is the full width at half maximum. The calculated values of strain were found to be inversely related to the lattice constant a and c as shown in Fig. 8.2(e).

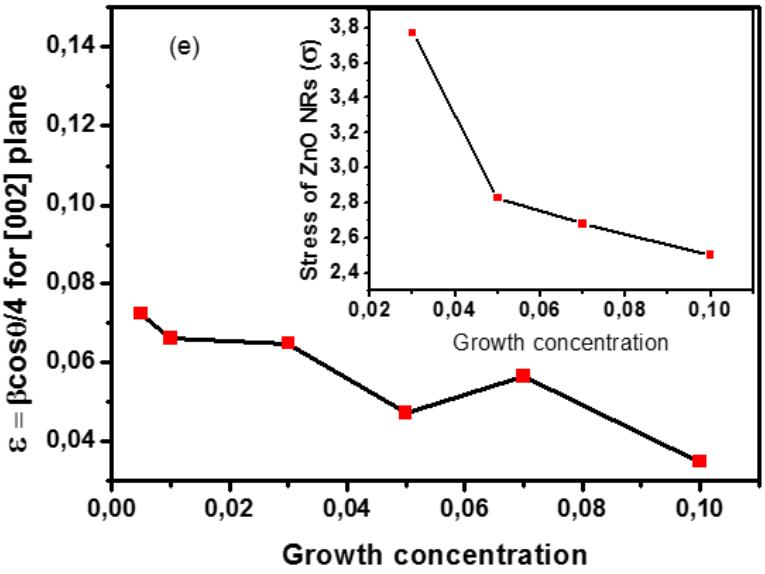

Figure 8.2: (e) Graph of microstrain (ε) and the inset: residual stress (σ) within the microstructure of the ZNRs.

The other structural parameter calculated was the residual stress within the microstructure of the ZNRs, which is also linked to the lattice parameters. It is understood that the stress in the NRs or the films could be due to impurities and defects in the crystal or as a result of lattice mismatch, growth conditions and mismatch in the thermal expansion coefficient of the film and substrate [33]. The residual stress of the samples was calculated using the following equation adapted from the formula [34]:

$$\sigma = -232.81 \times \frac{c_{calc.} - c_{bulk}}{c_{bulk}} \tag{8.4}$$

Where σ denotes the residual stress, c_{bulk} is the lattice constant for the bulk and $c_{calc.}$ is the calculated lattice constant of ZNRs. The stress values were found to be 3,77086, 2,82736, 2,68152, and 2,50078 GPa for 0.03, 0.05, 0.07 and 0.1 M respectively as displayed in Fig. 8.2(e) inset. The results are shown to decrease with the increase in growth concentration just like the microstrain values. The ZNRs grown at 0.1 M growth concentration yielded the lowest residual stress among the samples. In this work, the observed residual stress could be due to growth conditions, intrinsic stress as a result of lattice mismatch between the GZO seed layer film and the glass substrate or the thermal expansion coefficient of the film and glass substrate and not due to microstructure/defect related internal stresses or impurities and defects in the microstructure of ZNRs. Because the PL result shows an increasing defect with increasing growth concentrations.

8.3.2 SEM and AFM analysis

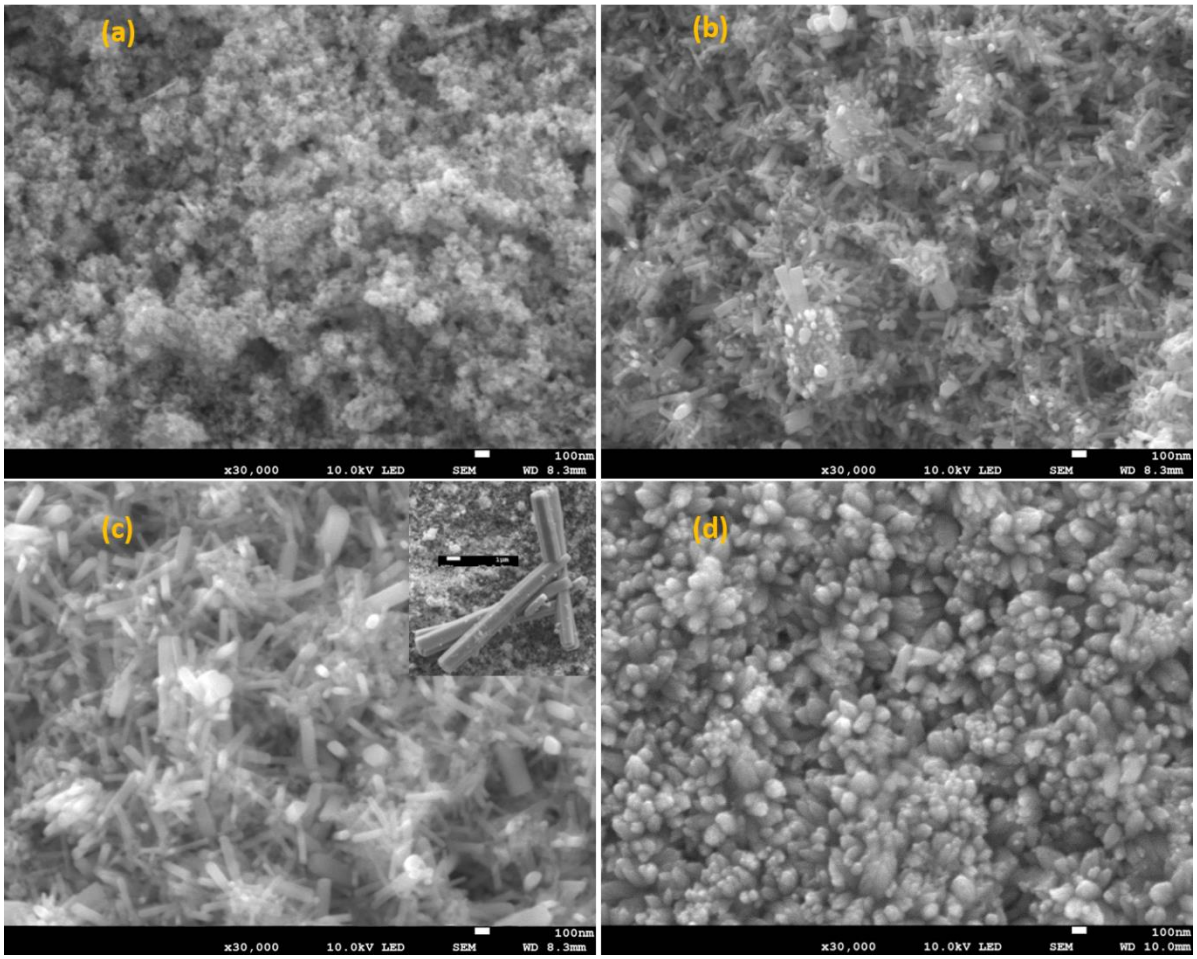

Figure 8.3: SEM images of ZNRs prepared from diverse growth concentrations: (a) 0.005, (b) 0.03, (c) 0.05 M and (d) 0.1 M. Fig. 3 (inset): hexagonally shaped ZNRs arrays at 0.05 M observed at micrometric level.

The SEM images, Fig. 8.3(a-d), reveal varying morphologies of the ZNRs arrays that were grown at different concentrations of the precursor solutions. In Fig. 8.3(a), the ZNRs were made of tiny, agglomerated and irregular nanorods. Fig. 8.3(b) shows hexagonal nanorods with improved morphology at 0.03 M concentration. With the increase of concentration to 0.05 M, Fig. 8.3(c), more regular and orderly nanorods with enhanced morphology could be observed. The inset Fig. 8.3(c) illustrates a distinguishable hexagonal nanorods, image at a micrometric level, of ZnO observed for the 0.05 M concentration material. The increase of growth concentration resulted in the formation of ZNRs with improved uniformity and alignment in addition to an increase in length and diameter. Apparently, at higher concentrations, there are favorable nucleation sites on which ZNR arrays can grow in a highly aligned fashion [35]. However, with a further increase in concentration, the morphologies of the nanorods began to evolve from hexagonal rods to "nanoflower"-like structures. It can, thus, be concluded that 0.05 M is the optimal concentration in this experiment. The fact that the crystallites produced at the 0.05 M concentration of the growth solution are less densely packed, makes it suitable for applications that require post-deposition processing such as infiltration of dye molecules onto the rods [22]. In agreement with the report by [28] et al, the SEM results show hexagonal nanorods, which are aligned vertically on the substrate, grow along the c-axis direction.

In addition to SEM, the AFM measurement was employed to study the topographic features and the evolution of surface properties of the ZNR films deposited at different growth concentrations. The 3-D images of the ZNRs covering 500 x 500 nm^2 are shown in Fig. 8.4(a-c). The AFM image in Fig. 8.4(a) shows that the nanorods are merged into 2D ZnO bridges at the surfaces. However, the head parts of the nanorods could still be observed. Fig. 8.4(b) shows a more-defined grain growth of the ZNRs, with a uniform size distribution and bud shaped surface morphology which is comparable with previous studies [36, 37]. The density of the nanorods was almost constant over the whole area and they mostly stood independently without touching one another. On the other hand, the film deposited at 0.1 M concentration, Fig. 8.4(c), showed agglomeration and coalescence of the nanorods. Clearly, the grain sizes of the NRs as depicted by the AFM were found to be in good agreement with the SEM results and are correlated to the crystallite sizes obtained from the XRD analysis which showed an increase in size with the increase in concentrations. The RMS surface roughness of the films was 3.36, 6.07 and 11.24 nm. An increase in the values of the RMS observed upon increase in concentration is expected, since the film surface becomes rougher owing to the formation of more nanorod arrays.

Moreover, from this AFM image, it can be estimated that the height of the ZnO NRs on the seed layer film is about 20, 40 and 90 nm for the 0.005, 0.05 and 0.1 M growth concentrations respectively. Thus it can be deduced from these results that the ZNRs film prepared at 0.05 M concentration yields a well-defined morphology, relatively longer, well-aligned and smoother nanorods.

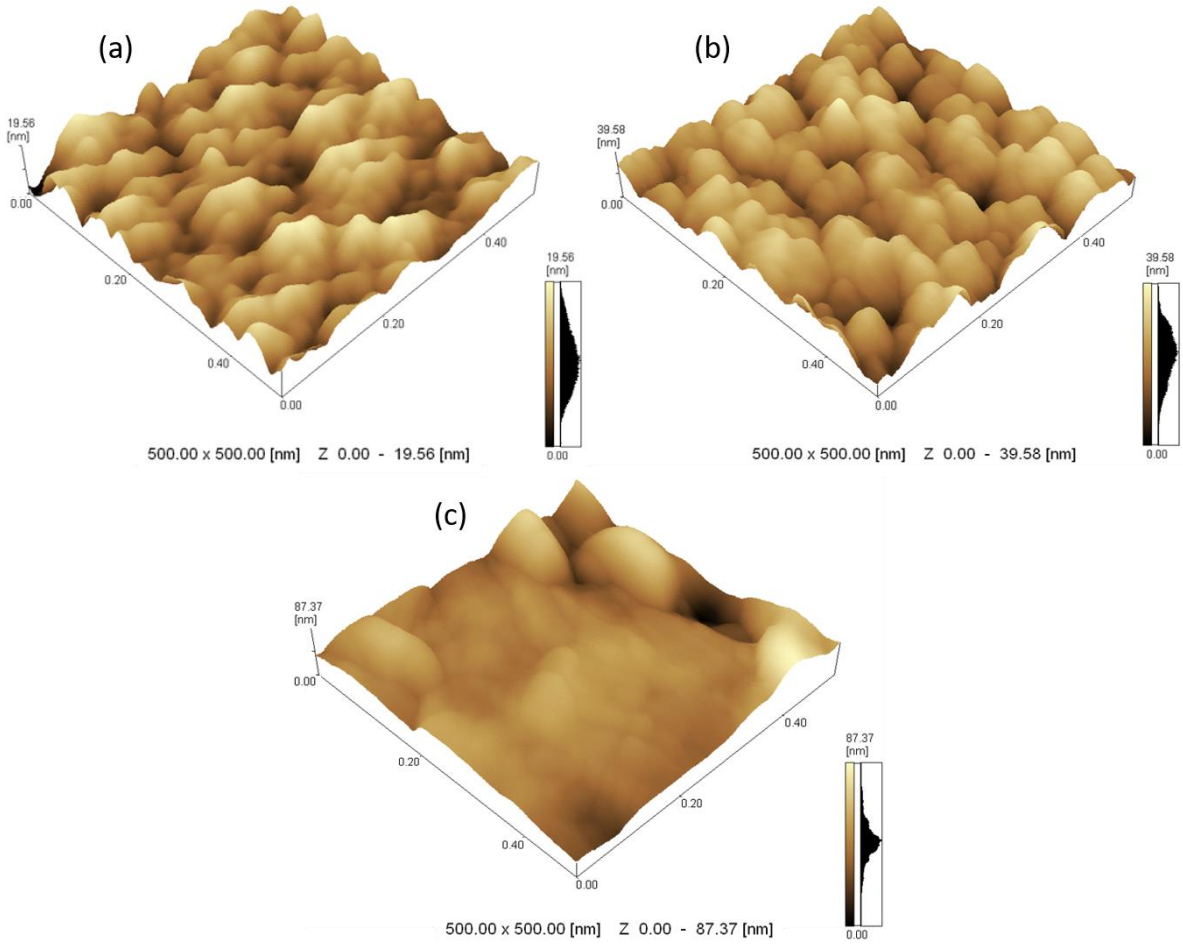

Figure 8.4: AFM images (500×500 nm^2) of ZnO nanorods grown at (a) 0.005, (b) 0.05 and (c) 0.1 M concentrations of the growth solution.

The differences in morphology, density, orientation and alignment of ZNRs as observed in SEM and AFM measurements can be explained in view of the formation mechanism that governs CBD method where a solid phase is formed on a substrate from an aqueous solution through nucleation and growth processes [13] via hydrolysis and/or condensation reactions of metal ions and/or complexes from aqueous bath solution [38]. Urgessa et al. [39] reported that the nucleation phase involved a rapid decomposition of the clusters of molecules formed and the combination of particles to grow up to a certain thickness of the film on the substrate surface. In this investigation, Zn $(NO_3)_2 \cdot 6H_2O$ was used as the source of zinc while $C_6H_{12}N_4$ provided the hydroxide ions (OH^-). Precipitation of $Zn(OH)_2$ was realized

when precursor solutions were reacted at the growth temperature of 90 ℃. This was followed by formation of ZnO nuclei from the precipitate deposited on the GZO glass substrate, which formed the bases for the growth of the ZNRs. As the growth time progressed, the dimensions of the nanorods increased but stopped after some period of time and erosion process will begin [40]. The set of equations [41-43] listed below is suggested to be the formation mechanism of ZNRs from the reaction between $C_6H_{12}N_4$ and $Zn(NO_3)_2$ which, in general, involves the initial precipitation of $Zn(OH)_2$ in a basic solution followed by its dissolution.

$$C_6H_{12}N_4 + 6H_2O \leftrightarrow 6CH_2O + 4NH_3 \quad (8.5)$$

$$NH_3 + H_2O \rightarrow NH_4^+ + OH^- \quad (8.6)$$

$$Zn(NO_3)_2 \rightarrow Zn^{2+} + 2NO_3^- \quad (8.7)$$

$$Zn^{2+} + 4NH_3 \rightarrow Zn(NH_3)_4^{2+} \quad (8.8)$$

$$Zn^{2+} + 4OH \rightarrow Zn(OH)_4^{2-} \quad (8.9)$$

$$Zn(NH_3)_4^{2+} + 2OH^- \rightarrow ZnO + 4NH_3 + H_2O \quad (8.10)$$

$$Zn(OH)_4^{2-} \rightarrow ZnO + H_2O + 2OH \quad (8.11)$$

The culmination of the reaction is where the two complexes ($Zn(NH_3)_4^{2+}$ and $Zn(OH)_4^{2-}$) were generated in the solution to become the precursors of ZNRs [44] as illustrated in the equations.

8.3.3 Photoluminescence analysis

Fig. 8.5(a) shows the PL emission spectra of the ZNRs prepared at different growth concentrations. Normally, ZnO exhibits two types of emission; the UV or exciton emission which is associated with a near band-edge transition of ZnO as a result of the recombination of the free excitons and the defect level emission (DLE) due to the deep level defects [45–47]. In this result, we found a strong and dominant band to band excitonic emission as well as minor peaks of DLE. The prominent excitonic peak in the spectra indicated that the obtained ZNRs have good crystallization and low density of the deep level defects.

Fig. 8.5(a) inset elucidates the excitonic emission peak shifts of ZNRs towards higher wavelengths (from 386-388 nm) with the increase in growth concentrations. The cause of red shift could be due to commonly known Ostwald ripening process [48]. Kiprotich et al. [49] reported that the shift of emission wavelengths during Ostwald ripening process occurs when the smaller particles dissolve owing to their higher surface energy and larger particles

grow as more and more material adds to the existing nuclei forcing a reduction in total number of particles.

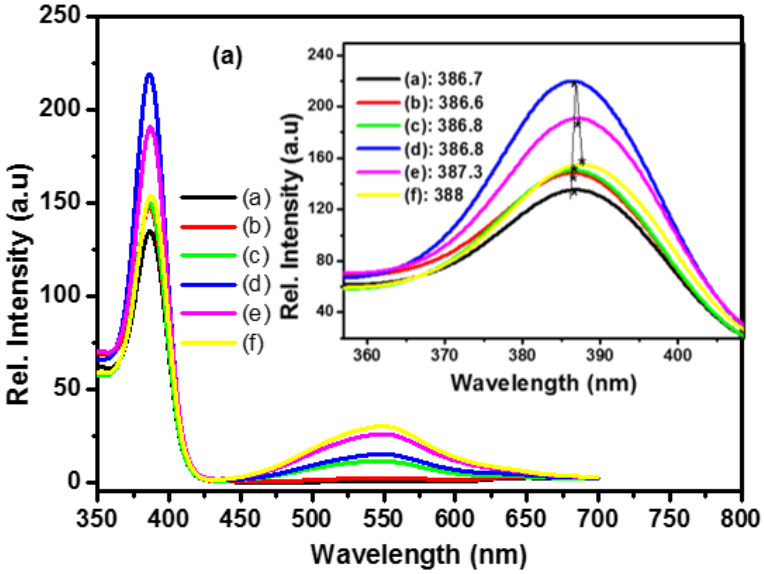

Figure 8.5: (a) Room-temperature PL spectra and Inset: enlarged excitonic peak emission spectra for ZNRs grown at (a) 0.005 (b) 0.01 (c) 0.03 (d) 0.05 (e) 0.07 (f) 0.1 M growth concentrations.

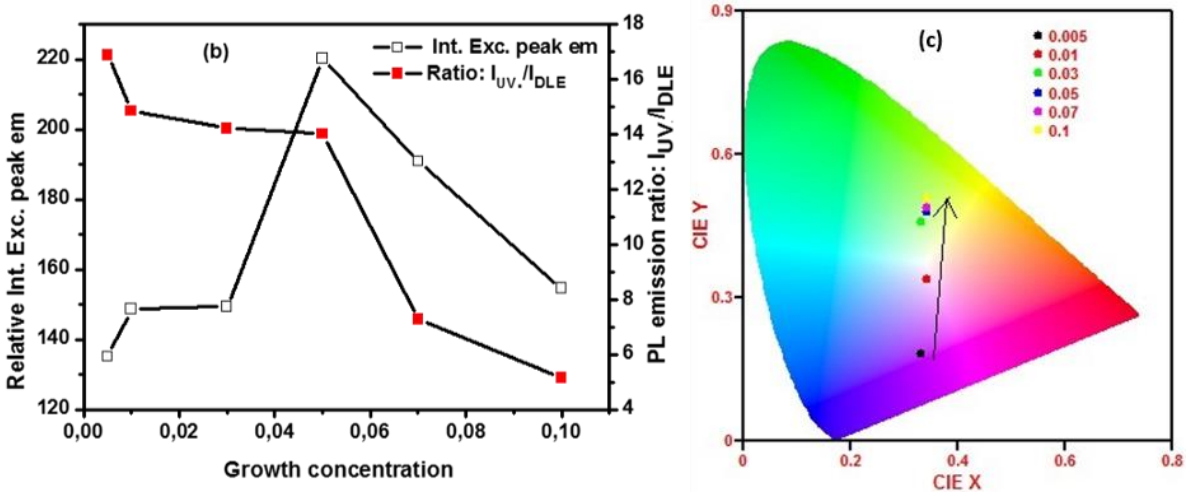

Figure 8.5: (b) The Exc. /DLE peak intensity ratios and relative intensity of excitonic peak emission (c) CIE spectra for ZNRs grown at 0.005, 0.01, 0.03, 0.05, 0.07 and 0.1 M growth concentrations.

Fig. 8.5(b) shows the variation in the relative intensity of the exciton peak emission of the ZNRs with the increase in concentration from 0.005 - 0.1 M. It was observed that the emission increased up to 0.05 M growth concentration but decreased in intensity with further increase in concentration. This decrease could be due to an increase in concentration of defects [50] such as Zn and O vacancies in the structures of the NRs as evidenced by the linear increase of the DLE emissions with the increase in the growth concentration as could

be seen in Fig. 8.5(a). The intensity ratio of the UV emission (I_{UV}) to deep level emission (I_{DLE}) was calculated from the PL emission result in order to establish the correlation between the optical properties and the morphology of the ZNRs [51]. Generally, the intensity ratio I_{UV}/I_{DLE} is regarded as an indicator of the crystallinity of ZnO materials since the highest peak intensity ratio reflects better optical properties owing to higher crystal quality and lower concentration of structural defects [52]. The results of this study is in agreement with the report that the I_{UV}/I_{DLE} ratio decrease as the size of the ZNRs increases [4], following the increase in growth concentration as shown in Fig. 8.5(b).

The Commission International de I'Eclairage (CIE) chromaticity diagram of the ZNRs and are presented in Fig. 8.5(c). The x, y coordinates of the CIE, which is used to describe the color properties of the source of light, depicts a linear shift of the co-ordinates from the Indigo to the yellow region of the CIE map, with the increase in concentration. The shift of the co-ordinates, indicated by the arrow, was also supported by the PL emission spectra wavelength shifts.

8.3.4 Optical properties

Fig. 8.6(a) displays the % optical transmittance (% T) of the as-synthesized ZNRs on the GZO seeded glass substrates that were grown in different growth concentrations. The visible light % T for ZnO NRs was observed to decrease with the increase in the concentration, as the films get denser with an increasing diameter and number of ZNRs. It is also reported that improved % T at lower growth concentrations could be due to the surface morphology and crystallinity of the thin film [53]. The large particles formed at higher concentrations of the growth solution would also contribute to scattering of the light which could result in a decrease in the % T.

The red shift of the absorption edge of the ZNRs with the increase in concentration values follows the red-shift in PL emission attributed to the crystal field due to the changes in the structure of the samples as the growth condition of solutions changes. The absorption coefficient (α), is calculated from % T data using the Beer-Lambert law:

$$\alpha = \frac{1}{d}\ln\left[\frac{1}{T}\right] \tag{8.12}$$

Where d is the thickness of the films. The relation between α and the incident photon energy ($h\nu$) can be found in the Tauc's theory. For the direct allowed transitions occurring in the direct band gap of ZnO, α near the band edge approximates to:

$$\alpha hv = A\sqrt{hv - Eg} \tag{8.13}$$

Where, A is a constant and Eg is the band gap of the materials. The band gap energy, Eg of ZNRs can be now estimated by extrapolating the straight line portion of $(\alpha hv)^2$ to $(\alpha hv)^2 = 0$ of Tauc's plot shown in Fig. 8.6(b).

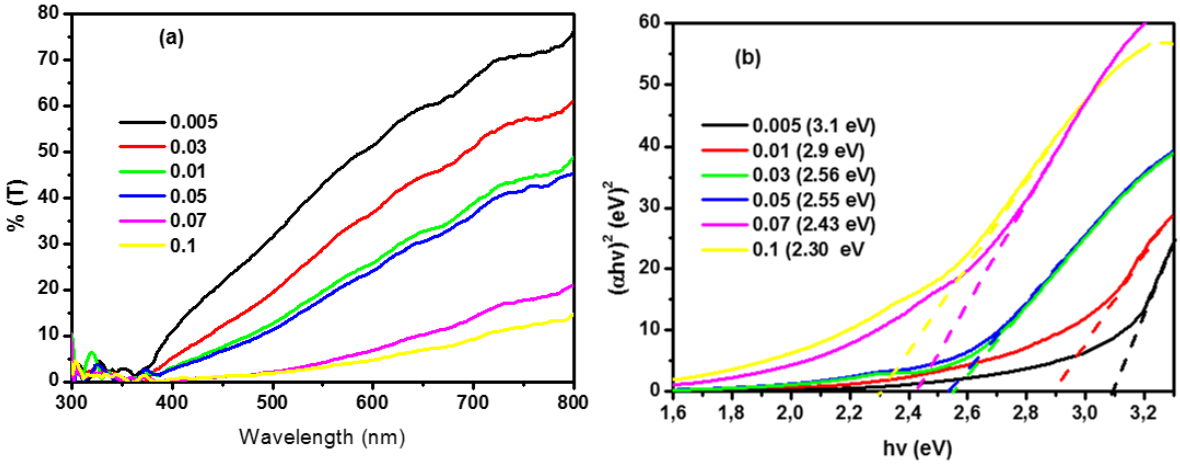

Figure 8.6: (a) UV–Vis % transmittance spectra and (b) Band gap energy plot of ZNRs at varied growth concentrations from 0.005-0.1 M.

The band gap energy decreases from 3.1-2.30 eV with the increase in growth concentration from 0.005-0.1M. The observed decrease in optical band gap caused by the shift in the band edge could be due to the enhanced crystalline structure of the ZNRs as a result of the increase in growth concentration or could also, be attributed to an increasing tensile strain which influences inter-atomic spacing. This linear variation of the band gap with the change in growth concentration provides a lot of control in selecting a particular spectral sensitivity for a specific application.

Conclusions

ZNRs structures were successfully grown by using the CBD method on GZO seeded glass substrates. The ZNRs were prepared using different concentration of an equimolar solution of Zn $(NO_3)_2$ and HMTA, ranging from 0.005 - 0.1 M, at a constant growth temperature and time of 90 ℃ and 90 min. respectively. The XRD results showed the increased crystallinity of the ZNRs with the increasing growth concentration. Also, the [002] intensity and c-axis orientation was greatly enhanced with the increase in growth concentrations indicative of a preferential growth direction of the ZNRs. The SEM images depicted an optimal concentration at 0.05 M since ZNRs with improved uniformity and alignment in addition to increase in length and diameter were formed. The PL spectra showed that the exciton peak

emission increased in intensity with increase in concentration from 0.005 - 0.05 M. But, a decline in exciton peak intensity was noted after 0.05 M concentration which was due to increased concentration of defects such as Zn and O vacancies as evidenced by the linear increase of DLE emissions with the increase in concentration. The band gap energy of the samples decreases from 3.1-2.30 eV as precursor conc. increases from 0.005 - 0.1 M. The results indicate that the change in reaction concentration of the experiment played a crucial role in the improvement of the morphology and optical properties of the ZNRs. The ZNRs that were grown on GZO transparent conductive film, at 0.05 M possessed fairly structural and optical properties required for the fabrication of a photo anode in DSSCs.

References

[1] M. J. Zheng, L. D. Zhang, G. H. Li, W. Z. Shen, Chem. Phys. Lett. 363, (2002) 123–128.

[2] C. H. Liu, J. A. Zapien, Y. Yao, X. M. Meng, C. S. Lee, S. S. Fan, Y. Lifshitz, S. T. Lee, Adv. Mater. 15, (2003) 838–841.

[3] P. X. Gao, Z. L. Wang, J. Phys. Chem. B 108, (2004) 7534–7537.

[4] B. Weintraub, Z. Zhou, Y. Li, Y. Deng, Nanoscale 2, 9 (2010) 1573–1587.

[5] Y. Zhang, M. K. Ram, E. K. Stefanakos, D. Y Goswami, Journal of Nanomaterials 2012, (2012) 20.

[6] P. S. Kumar, S. M. Maniam, J. Sundaramurthy, J. Arokiaraj, D. Mangalaraj, D. Rajarathnam, L. K. Jian, Materials Chemistry and Physics, 133(1), (2012) 126-134.

[7] H. Guo, J. Zhou, Z. Lin, Electrochem. Commun. 10, (2008) 146.

[8] Z. Fan, J. G. Lu, Appl. Phys. Lett. 86, (2005) 123510.

[9] X. Liu, L. Ye, S. Liu, Y. Li, X. Ji, Scientific reports 6, (2016) 38474.

[10] O. Lupan, V. M. Guérin, I. M. Tiginyanu, V. V. Ursaki, L. Chow, H. Heinrich, Th Pauporté, Journal of Photochemistry and Photobiology A: Chemistry 211(1), (2010) 65-73.

[11] Y. Tong, L. Dong, Y. Liu, D. Zhao, J. Zhang, Y. Lu, D. Shen, X. Fan, Mater. Lett. 61, (2007) 3578.

[12] L. Vayssieres, K. Keis, A. Hagfeldt, S.E. Lindquist, Chem. Mater. 13, (2001) 4395.

[13] J. Zhao, Z. G. Jin, X. X. Liu, Z. F. Liu, Journal of the European Ceramic Society 26(16), (2006) 3745-3752.

[14] L. Yang, Q. X. Zhao, M. Willander, Journal of alloys and compounds 469, (2009) 623-629.

[15] S. Kim, G. Nam, H. Park, H. Yoon, S. Lee, J.S. Kim, Bulletin of the Korean Chemical Society 34, (2013) 1205–1211.

[16] T. H. Fang, S. H. Kang, Current Applied Physics 10, (2010) 1076–1086].

[17] S. Kim, H. Park, G. Nam, H. Yoon, B. Kim, I. Ji, J. Y. Leem, Electronic Materials Letters 10(1), (2014) 81-87.

[18] K. Ellmer, J. Phys. D: Appl. Phys. 34(21), (2001) 3097.

[19] J. Ungula, B. F. Dejene, H. C. Swart, Journal of Luminescence 195, (2018) 54–60

[20] R. B. Peterson, C. L. Fields, B. A. Gregg, Langmuir 20, (2004) 5114–5118.

[21] C. H. Hung, W. T. Whang, J. Cryst. Growth, 268, (2004) 242–248.

[22] K. Govender, D. S. Boyle, P. B. Kenway, P. O'Brien, Journal of Materials Chemistry14 (16), (2004) 2575-2591.

[23] J. Ungula, B. F. Dejene, H. C. Swart, Physica B: Condensed Matter 535, (2018), 251-257

[24] B. D. Cullity, S. R. Stock, ‘‘Elements of X-Ray Diffraction’’; pp. 388–90 in Chapter 14-3 Crystallite Size, Prentice- Hall Inc, Englewood Cliffs, NJ, 2001.

[25] G. eC. Yi, C. Wang, W. IL Park, Semicond. Sci. Technol. 20, (2005) S22.

[26] International Center for Diffraction Data, 2011, File 00-001-1136.

[27] W. Y. Wu, C. C. Yeh, J. M. Ting, Journal of the American Ceramic Society 92(11), (2009) 2718-2723.

[28] J. Yang, J. Lang, L. Yang, Y. Zhang, D. Wang, H. Fan, M. Gao, Journal of Alloys and Compounds 450(1), (2008) 521-524.

[29] D. I. Rusu, G. G. Rusu, D. Luca, Acta Physica Polonica A 6, (2011) 119.

[30] V. Kumari, Vinod Kumar, B.P. Malik, R.M. Mehra, Devendra Mohan, Opt. Commun. 285 (8), (2012) 2182–2188.

[31] C. Rajashree, A. R. Balu, V. S. Nagarethinam, Int. J. Chem. Tech. Res. 6, (2014) 347-360.

[32] M. R. A. Bhuiyan, M. A. A. Azad, S. M. F. Hasan, J. pure Appl. Phys. 49, (2011) 180-185.

[33] V. Kumar, N. Singh, R.M. Mehra, A. Kapoor, L.P. Purohit, H.C. Swart, Thin Solid Films 539, (2013) 161–165.

[34] R. Hong, J. Huang, H. He, Z. Fan, J. Shao, Appl. Surf. Sci. 242, (2005) 346.

[35] S. F. Wang, T. Y. Tseng, Y. R. Wang, C. Y. Wang, H. C. Lu, W. L. Shih, International Journal of Applied Ceramic Technology 5(5), (2008) 419-429.

[36] S. H. Park, S. H. Kim, S. W. Han, Nanotechnology 18, (2007) 055608.

[37] E. Hasabeldaim, O. M. Ntwaeaborwa, R. E. Kroon, V. Craciun, E. Coetsee, H. C. Swart, Applied Surface Science 424, (2017) 412-420.

[38] P. O'Brien, J. McAleese, Journal of Materials Chemistry 8(11), (1998) 2309-2314.

[39] Z. N. Urgessa, K. Talla, S. R. Dobson, O. S. Oluwafemi, E. J. Olivier, J. H. Neethling, J. R. Botha, Materials Letters 108, (2013) 280-284.

[40] J. Yang, J. Lang, L. Yang, Y. Zhang, D. Wang, H. Fan, M. Gao, Journal of Alloys and Compounds 450(1), (2008) 521-524.

[41] Q. C. Li, V. Kumar, Y. Li, H.T. Zhang, T.J. Mark, R. P. H. Chang, Chem. Mater. 17, (2005) 1001–1006.

[42] X. D. Gao, X. M. Li, W. D. Yu, J. Phys. Chem. B 109, (2005) 1155–1161.

[43] L. Yu, G.M. Zhang, S.Q. Li, Z.H. Xi, D.Z. Guo, J. Cryst. Growth 299, (2007) 184–188.

[44] L. Yang, Q. X. Zhao, M Willander, Journal of alloys and compounds 469(1), (2009) 623-629.

[45] V. Kumar, H. C. Swart, M. Gohain, V. kumar, S. Som, B. C. Bezuindenhoudt, O. M. Ntwaeaborwa, Ultrason. Sonochem. 21, (2014) 1549–1556.

[46] Vinod Kumar, H. C. Swart, O. M. Ntwaeaborwa, R. E. Kroon, J. J. Terblans, S. K. K. Shaat, A. Yousif, M. M. Duvenhage, Mater. Lett. 101, (2013) 57–60.

[47] H. Zeng, G. Duan, Y. Li, S. Yang, X. Xu, W. Cai, Adv. Funct. Mater. 20, (2010) 561–572.

[48] F. Jiang, A. J. Muscat, Langmuir 28, (2012) 12931–12940.

[49] S. Kiprotich, F. B. Dejene, J. Ungula, M. O. Onani, Physica B: Condensed Matter 480, (2016) 125-130.

[50] V. Kumar, V. Kumar, S. Som, A. Yousif, N. Singh, O. M. Ntwaeaborwa, H. C. Swart, Journal of colloid and interface science 428, (2014) 8-15.

[51] J. Yang, J. Song, S. Baek, S. Lim, Physica B: Condensed Matter 403(18), (2008) 3034-3039.

[52] J. Ungula, B. F. Dejene, Physica B: Condensed Matter 480, (2016) 26-30.

[53] S. Salari, M. Ahmadi, K. Mirabbaszadeh, Electron. Mater. Lett. 10(1), (2014) 13.

Chapter 9

Study on the role of deposition growth time on structural and optical properties of ZnO nanorods grown on GZO seeded thin film layer from aqueous solution

9.1 Introduction

The studies on one-dimensional (1D) ZnO nanostructures such as nanowires, nanotubes, nanorods, nanoribbons, nanobelts and nanocables [1-5] have taken centre stage, for some time now, and inspired a lot of scientific research interest because of their good electrical and photonic properties which are displayed in their usage in devices like UV optical detectors, ultraviolet (UV) laser diodes, dye-sensitized solar cells (DSSCs), optical switches, dimensionally stable anodes, bio- and gas-sensors and hydrogen storage devices [6].

Many reports have described ZnO nanorods (ZNRs) prepared by a one-step aqueous method, vapor-phase transport [7-9], pulsed laser deposition [10], chemical vapor deposition [11, 12] and electrochemical deposition [13]. However, complicated procedures, high temperatures, and sophisticated equipment are reported to have been used in the mentioned methods of ZNRs synthesis. The chemical bath deposition (CBD) method, on the other hand, is quite a facile and inexpensive process which requires simple apparatus and most importantly, the nanorods can be grown at low temperatures [14, 15]. In addition, the shape and size of the ZNRs can easily be controlled using the CBD technique by fine-tuning the growth parameters such as stoichiometric ratios of the reagents, the concentration of the solution, growth temperature, growth time and the solution pH [16 - 18].

Also, a lot of research has demonstrated successful growth of the ZNRs on seeded substrates. For instance, Govender et al [19] reported that pre-seeding of the substrates with a ZnO layer can facilitate nucleation at lower levels of supersaturation because heterogeneous nucleation onto a foreign surface is believed to occur more easily as

compared to the homogeneous nucleation [20]. More so, as far as the CBD technique is concerned, controlling the size and morphology of the nanorods has proven to be challenging that is why most researchers use a two-step process which involves pretreatment of the substrates and chemical bath deposition process [21, 22], For example, in their study of effective way to control the size of well-aligned ZNR arrays with two-step chemical bath deposition, Yang et al. [23] reported that the ZNRs grown on Si substrate through CBD method displayed poor results and difficulty in reproducibility. It is, thus, commonly agreed that ZnO seeding is essential for easy and convenient growth of a well-aligned ZNRs perpendicular to the substrates [24, 25]. The pretreatment is done using different methods which include; thermal deposition [26], radio frequency magnetron-sputtering [27] and spin coating [28] to prepare a seeded substrate.

Ga-doped ZnO (GZO) is preferred, in this study, for use as a TCO seed layer because of its many advantages which include; stability with respect to oxidation in comparison with aluminium and closeness of the ionic and covalent radii of Ga to that of Zn [29]. We believe, controlling the characteristics of the ZNRs by doping into the seed layer has been rarely reported in the literature. In fact, the influence of deposition growth time on the structural, morphological and optical properties of the ZNRs thin films prepared through a two-step aqueous solution process on glass substrate seeded with an optimized GZO layer is reported for the first time in this investigation. It is expected that the results of this study will advance the understanding of the properties of ZNRs that were grown on the GZO films which would together provide a promising combination for use as photoelectrode in dye-sensitized solar cells application. Indeed, the ZnO NRs showed distinct morphologies in different deposition growth times with well-aligned rods obtained at 90 min of growth time.

9.2 Experimental procedure

The chemical reagents used are sodium hydroxide (NaOH), zinc nitrate hexahydrate ($Zn(NO_3)_2.6H_2O$, 99.9% purity), methenamine ($C_6H_{12}N_4$, 99.9% purity) and gallium nitrate hexahydrate ($Ga(NO_3)_3.6H_2O$, 99.9% purity). All the chemicals used were of analytical grade and thus used without further purification. Double distilled water was used to prepare all aqueous solutions. The details of synthesis process of ZNRs using the two-step CBD growth method are described as follows. The schematic diagram showing the two-step procedure followed in the preparation of ZNRs on the GZO seeded glass substrate is shown in Fig. 8.1. The procedure of this study is similar to the one followed in Chapter 8. In this

section, the deposition growth time was studied with all other optimized conditions put into consideration.

Firstly, as prepared and optimized GZO seed particles were deposited on a glass substrate using spin coating technique. The GZO nanopowders were prepared as described in Ref [30]. The GZO powder was ground, dissolved in suitable solvent and mixed into a homogenous paste to form the spin coating solution. The solution was spin-coated onto glass substrates using a SPEN 150 spin coater at the rate of 2000 rpm for 30 s. The as-deposited films were immediately pre-annealed on a hot plate at 250 ^{o}C and for 10 min. To obtain an appropriate thickness and complete coverage of GZO seed layer the deposition and preheating procedures were repeated 10 times. Thereafter, the GZO films were post-annealed in the air to 500 ^{o}C from RT, held at 500 ^{o}C for 120 min, and cooled in a furnace to RT.

Secondly, the ZNRs were grown from the GZO seeds by immersing seed-coated substrates in the reaction bath of aqueous precursor solutions. The reaction bath solution was prepared by dissolving equimolar (0.05 M) solutions of Zn $(NO_3)_2$). $6H_2O$ and HMTA separately in 30 ml distilled water and then mixed under continuous stirring for 2 hrs at room temperature and 10 ml of distilled water added to make a 70 ml solution in a100 ml beaker reaction vessel. The reaction vessel containing the reaction bath and the suspended glass substrate seeded with GZO film was then placed in a thermostatically controlled water bath. To monitor the growth process in CBD set up, the deposition growth time was varied from 30-150 min. The thin film was finally removed from the solution, rinsed with double-distilled water then dried in an oven at 70 ^{o}C for about 5 min.

The crystal structures of ZNRs were analyzed using X-ray diffraction (XRD) Model Philips Bruker D8 Advance, Germany, X-ray diffractometer (XRD) with a Cu Anode X-ray tube (with a Kα radiation wavelength of 1.5406 Å) over a 2θ range from 20-80 ^{o} at a scan rate of 0.02 ^{o}/s. The surface topography and compositional analysis of the ZNRs were studied using scanning electron microscope (SEM) model JEOL JSM-7800F equipped with Oxford Aztec EDS (Energy-dispersive X-ray spectroscopy) and atomic force microscopy (AFM) model Shimadzu SPM – 9600. The optical properties and band gap energies of ZNRs were analyzed using Ultraviolet–visible (UV–vis) spectroscopy (Perkin Elmer Lambda 950) in the 250–600 nm wavelength range while the photoluminescence (PL) spectroscopy studies were conducted using a Cary Eclipse fluorescence spectrophotometer; model LS-55 with a built-in 150W xenon flash lamp as the excitation source and a grating to select a suitable excitation wavelength.

9.3 Results and discussion

9.3.1 XRD analysis

Fig. 9.1(a) displays the XRD patterns of the ZnO NRs thin films grown on GZO seeded glass substrate for different deposition growth times. All the XRD patterns of the ZNRs thin films prepared at various deposition growth times (30 - 150 min) reveal the distinct diffraction peaks which are characteristic of the hexagonal crystal structure well indexed to the JCPDS card No. 75-1526, a = 3.220 nm, and c = 5.200 nm of ZnO, corresponding to the [100], [002], [101], [102], [110], [103] and [112] planes.

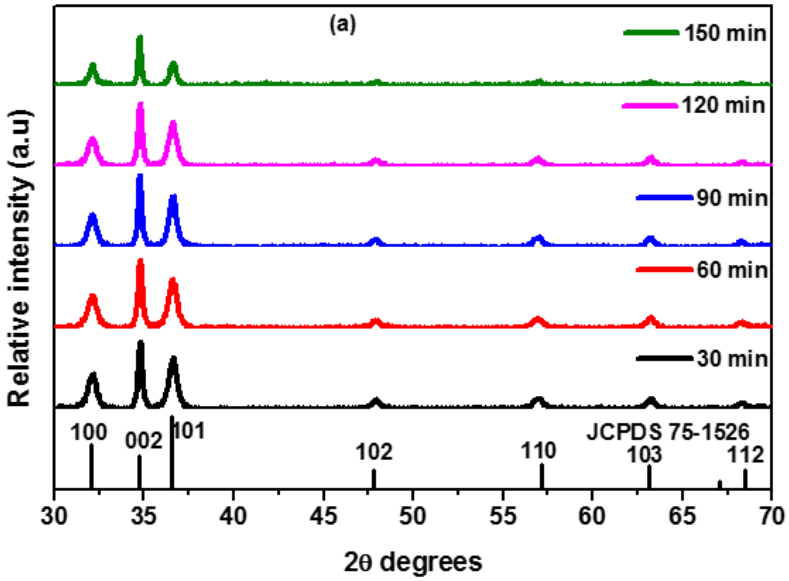

Figure 9.1: (a) XRD patterns of ZNRs on GZO seeded glass substrate in an equimolar precursor solution at different deposition growth times.

The XRD spectra of the ZNRs showed general enhancement of peak intensities indicative of an improvement in crystallinity of the samples. The diffraction peak intensity increased to a maximum at 90 min and decreased for longer deposition time. No other characteristic peaks from the XRD pattern could be identified which confirmed that all the ZnO nanostructures formed were single hexagonal wurtzite ZnO phase and had the high degree of crystallization.

Clearly, as could be seen in Fig. 9.1 (a), the intensity of [002] plane was the most enhanced as compared to the usual [101] most intense reflection in the standard pattern of ZnO. This observed phenomenon indicate a preferred growth of the ZNRs along the c-axis of the wurtzite structure as usually observed for the ZnO NRs [31, 32]. More often, to characterize the orientation of the ZNRs, the relative intensity ratio between (002) and (101) diffraction planes is used because it is [002] plane only which can give any further

information and evidence on the preferred c-axis orientation of the ZNRs. Thus, the degree of c-orientation described by the relative texture coefficient (TC) was calculated using the expression [33]. The calculated values of TC for (002) and (101) diffraction peaks denoted as $TC_{(002)}$ and $TC_{(101)}$ respectively for different deposition growth times were presented in Fig. 9.1(b).

Fig. 9.1(b) showed that the TC values of the (002) planes were greater than that of the (101) planes confirming the preferential growth of the ZNRs along the c-axis as mentioned earlier. The growth along this direction was favored because any growth deviating c-axis direction of the substrate were very difficult to grow under such higher density since the more they deviate from c-axis, the more they get obstructed [34].

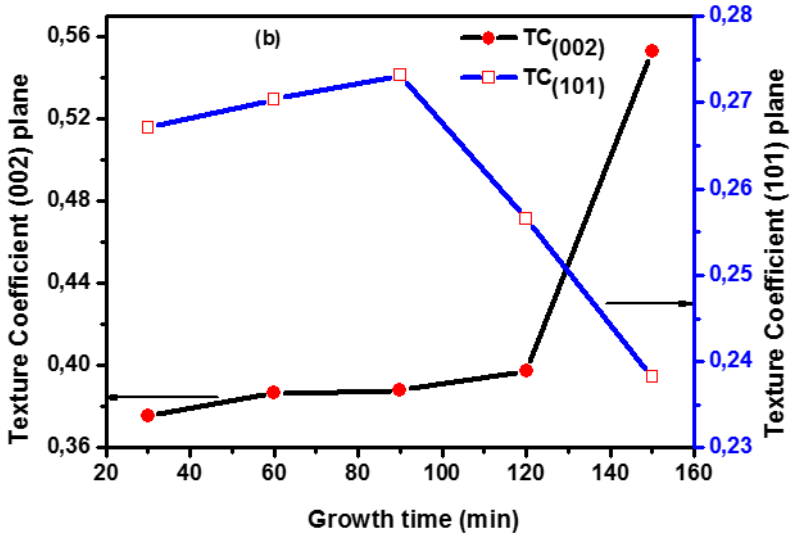

Figure 9.1: (b) Texture coefficients of [002] and [101] planes of ZNRs arrays as a function of growth time.

The ZnO NRs, therefore, are pertinent to grow along the c-axis when competition and optimization of rules are put into consideration. Studies have shown that the [101] surface face grows the fastest in nanopowders, as the growth progresses. However, the [002] plane in NRs thin films grows faster and increase in orientation at the expense of the [101] plane due to higher rates of deposition and growth along the c-axis resulting in reduced growth along the [101] orientation [35]. It is also important to note that the TC values of (002) plane increases with the increase in growth time. Similarly, the TC values of (101) plane increased, albeit, up to 90 min of deposition time and declined thereafter. The full width at half maximum (FWHM) of the as-prepared ZNRs thin films was obtained from all the diffraction peaks. It was found that FWHM values decreased with increase in deposition growth time as displayed in Fig. 9.1(c).

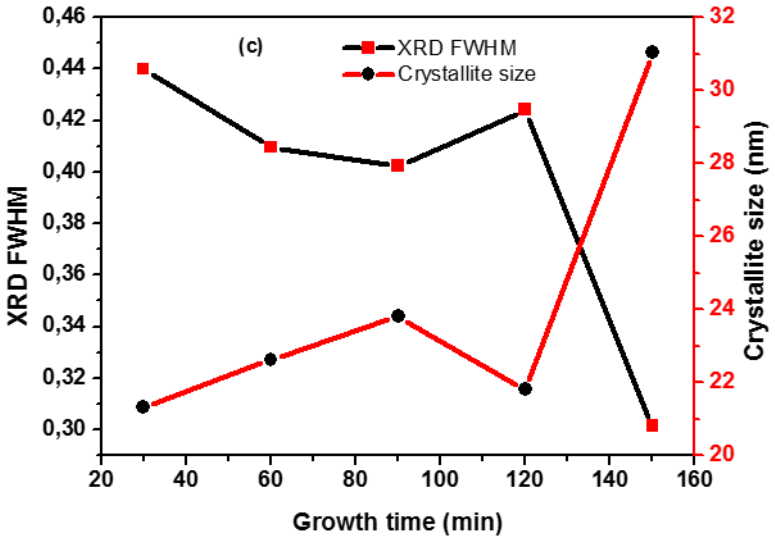

Figure 9.1: (c) Graph of the crystallite size and variation of FWHM values of ZNRs diffraction peaks against deposition growth time.

These FWHM values were then used to calculate the crystallite sizes of the characterized samples using the well known Debye Scherrer formula [36].The sizes of the crystallites were found to increase with an increase in the deposition growth time (30 - 150 min) a s shown in Fig. 9.1(c). The estimated crystallite sizes were 21.31, 22.62, 23.81, 21.81 and 31.04 nm for 30, 60, 90, 120 and 150 min of deposition growth time respectively.

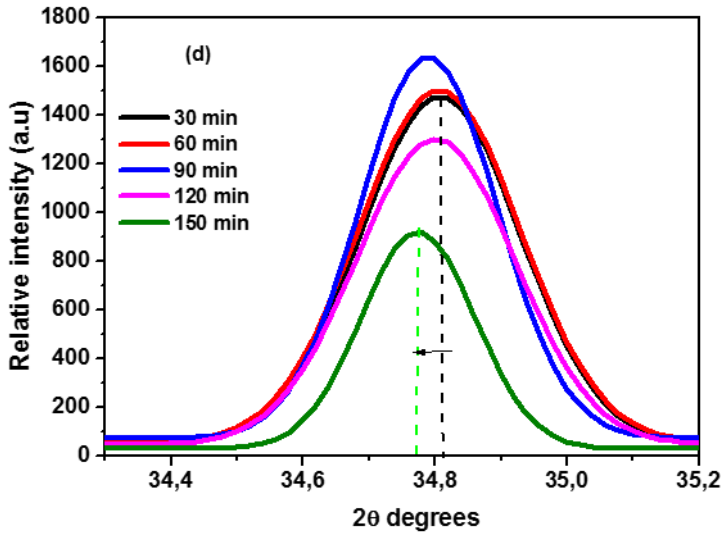

Figure 9.1: (d) Magnified XRD pattern of [002]diffraction peak displaying peak position shift and changes in peak intensity for the ZNRs at different deposition growth time.

With an increase in deposition growth time, peaks shift to lower 2θ angle was observed in the diffraction planes of ZNRs (Fig. 9.1d). This shift to lower diffraction angle, attributed to lattice expansion, is a further confirmation of an increase in the crystallite size with

increase in deposition growth time. To verify the expansion of lattice parameters of ZNRs, their values were calculated from the most dominant diffraction peaks of the XRD spectra according to the relation in ref [37] and tabulated in table 9.1. In comparison to the value of bulk ZnO (c = 5.204 Å), the calculated values are slightly lower indicating that the characterized samples may be under some strain.

The internal strain (ε) values of ZNRs were also determined using the Williamson-Smallman equation [38] and results captured in Table 9.1.

$$\varepsilon = \frac{\beta}{4\tan\theta} \tag{9.1}$$

Where, θ is the diffraction angle and β is the full width at half maximum.

Similarly, the lengths of the dislodgment streaks per unit volume, commonly known as the dislocation density (δ), were calculated using the following equation [39];

$$\delta = \frac{1}{D^2} \tag{9.2}$$

Where D is the size of the crystal obtained from the XRD pattern as explained earlier.

Table 9.1: A table displaying the lattice constant, the AFM RMS values and particle sizes, crystallite size, [002] plane peak position, strain and dislocation density of ZNRs at the different cell at varied deposition growth time.

Growth time (min)	Lat. Constants (Å)			AFM analysis		Crystallite size (nm)	Peak [002]	Strain (ε)	D/density δ (M^{-2})
	a	c	c/a ratio	R.M.S (nm)	Size (nm)				
30	3.2140	5.19819	1.6174	4.9	33.3	21.31	34.81	0.000606	0.0022
60	3.2141	5.20129	1.6183	-	-	22.62	34.8	0.000553	0.00195
90	3.2144	5.20215	1.6184	6.1	39.6	23.81	34.79	0.000543	0.00176
120	3.2140	5.16915	1.6083	-	-	21.81	34.8	0.000573	0.0021
150	3.2149	5.20115	1.6178	9.5	95.0	31.04	34.78	0.000407	0.001

It could be deduced from Table 9.1, that both the values of the strain and the dislocation density were inversely related to the deposition growth time. Since this dislocation density is an indicator of the dislocation network in the particle structure, the decrease with increase in deposition growth time designates improved crystallinity.

9.3.2 SEM analysis

The SEM micrograph images of ZNRs thin films deposited at different growth times are presented in Fig. 9.2. As shown, remarkable morphological transformations and improvements have been observed on the as-prepared ZNRs thin films as the growth time increases. For the shorter duration of deposition, tiny and agglomerated mixtures of nanorods and nanospheres could be seen which changed into well-aligned and uniformly

distributed ZNRs at 90 min. The film deposited at longer growth time, however, showed an enlarged morphology of flower-like structures of ZNRs. Apparently, at shorter deposition growth time nucleation takes place where the growth mechanism processes (diffusion and aggregation) occur as explained in ref [40]. Furthermore, the differences in morphology, density, orientation and alignment of ZNRs can be further explained in view of the formation mechanism that governs CBD method where solid phase is formed on a substrate from an aqueous solution through nucleation and growth processes [41]. As the growth time progressed, the dimensions of the nanorods increased but stopped after some period of time and erosion process began resulting to change in morphology of the ZNRs [42].

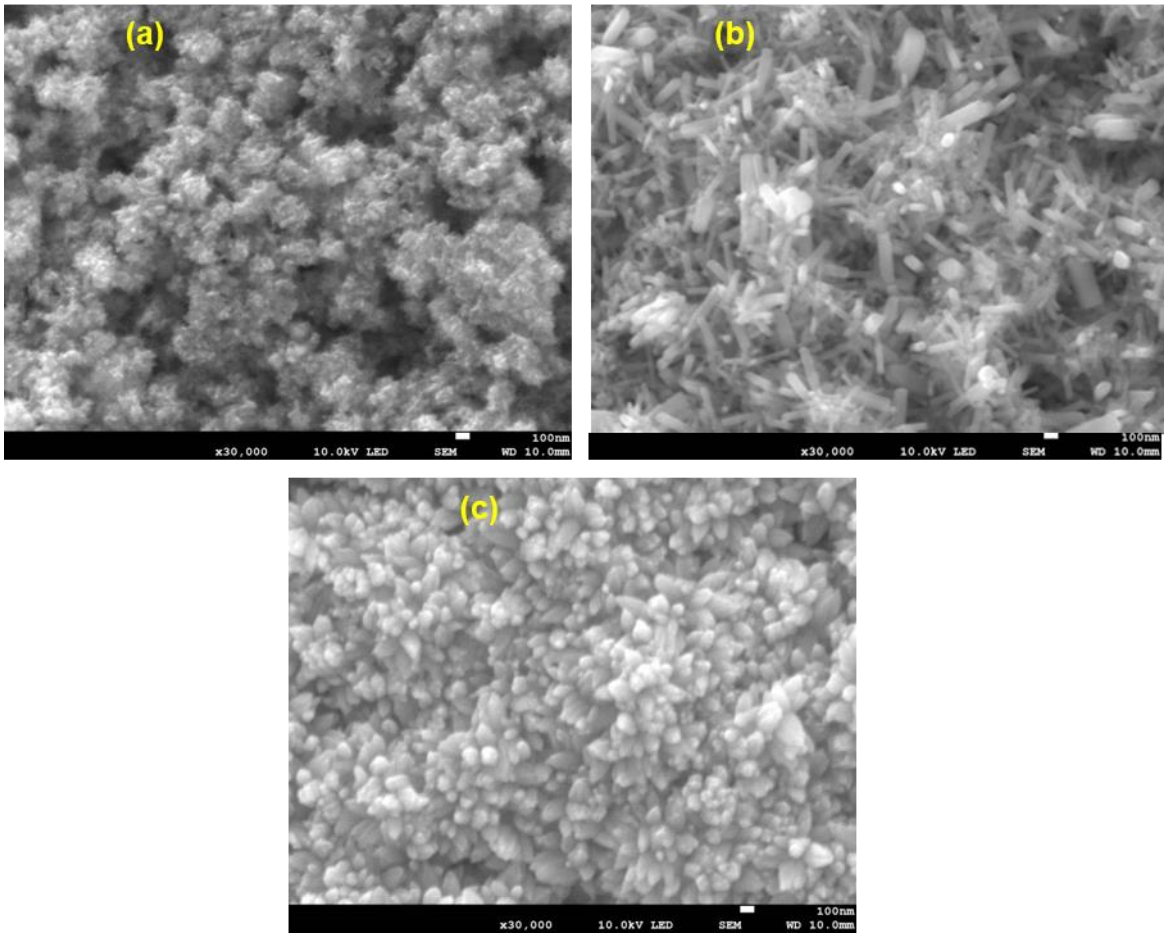

Figure 9.2: SEM images of ZNRs prepared at various deposition growth times(a, b,c for 30, 90 and 150 min respectively).

9.3.3 AFM analysis

In order to further the study of the surface topography of the ZNRs thin films prepared on GZO seeded glass substrate, AFM technique was used. The AFM probes the optical and electrical properties of a material by studying the evolution of the surface at a high atomic-scale resolution. Figs. 9.3(a-c) display 3-D AFM images of ZNRs covering 500 x 500 nm^2

prepared at different deposition growth times. They show clear changes in surface topography as the deposition time is increased which further confirms the observation made in the SEM images. The ZNRs thin films prepared at 90 min showed more defined, well-aligned and uniformly distributed nanorods over the entire surface of the substrate. The root mean square (RMS) roughness of the ZNRs were 4.86, 6.07 and 9.46 nm for the deposition time of 30, 90 and 150 min respectively. The increase in the roughness of the films with the increase in growth time could be due to the increase in the grain size (33.34, 39.58 and 95.03 nm for 30, 90 and 150 min of growth time). Kumar et. al. [43] and Hasabeldaim et.al [44] also reported that the surface roughness of the samples increased with the size of the particles.

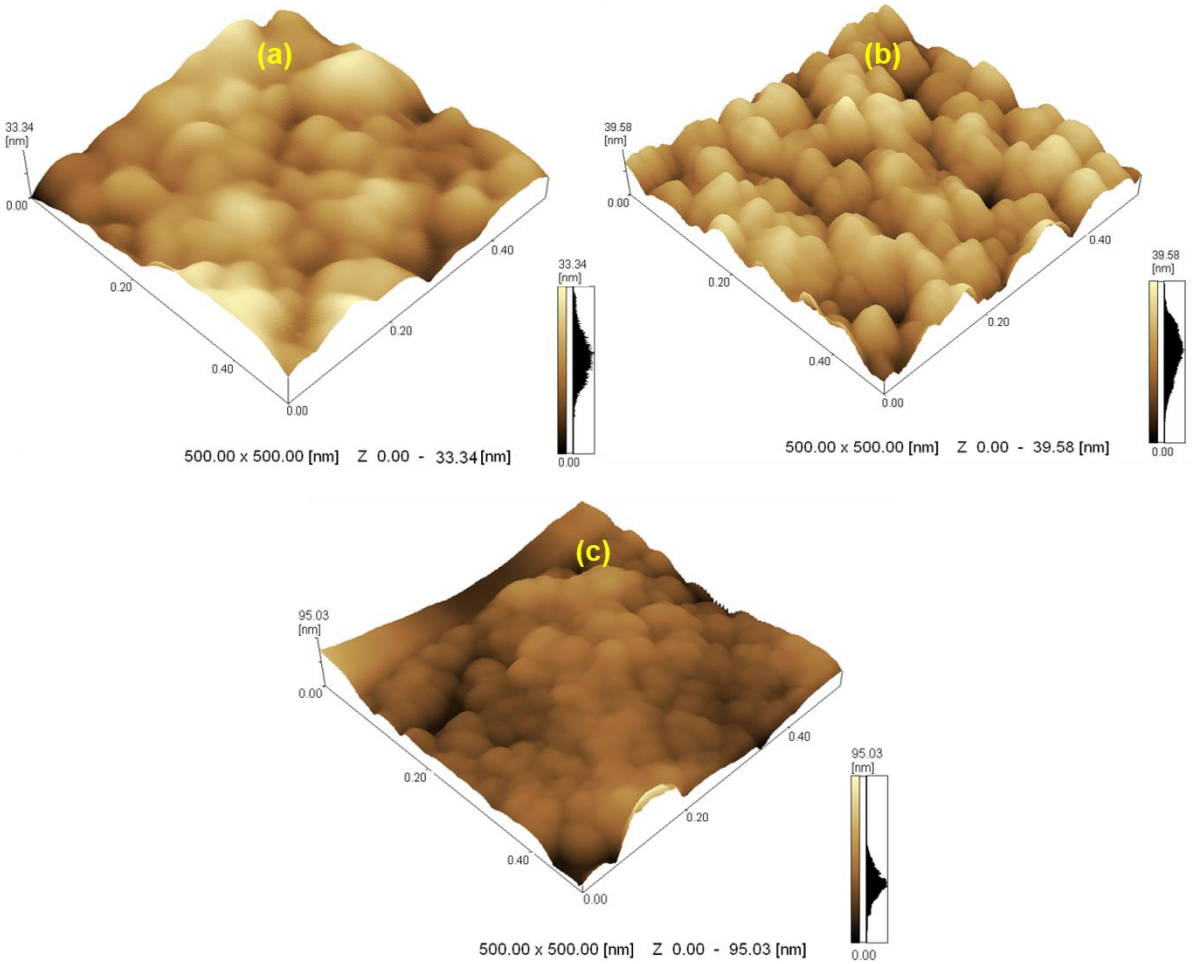

Figure 9.3: AFM 3-D images of ZNRs prepared at various deposition growth times (a, b,c for 30, 90 and 150 min respectively).

9.3.4 Photoluminescence analysis

The PL spectra of the ZNRs thin films at different growth times were displayed in Fig. 9.4(a). There were two PL emissions observed; one around 385 nm and the second one

around 550 nm. The blue emission peaks also called excitonic peak emission (around 385 nm) is known to be associated to a near band-edge transition of ZnO, precisely, the recombination of the free excitons. Whereas, the PL emission peaks around ~550 nm is attributed to defects such as O and Zn vacancies [45-48]. The enhancement of the excitonic peak emission was observed when deposition growth time is increased and reaches a maximum at 90 min but decreases thereafter, as illustrated in Fig. 9.4(b). The decrease in excitonic emission could be due to increase in concentration of deep level defects [49] in the structures of the NRs as evidenced by the linear increase of DLE emissions with the increase in the deposition growth time. This indicates that the best crystallinity can be obtained at 90 min of deposition growth time which is in agreement with the XRD observation.

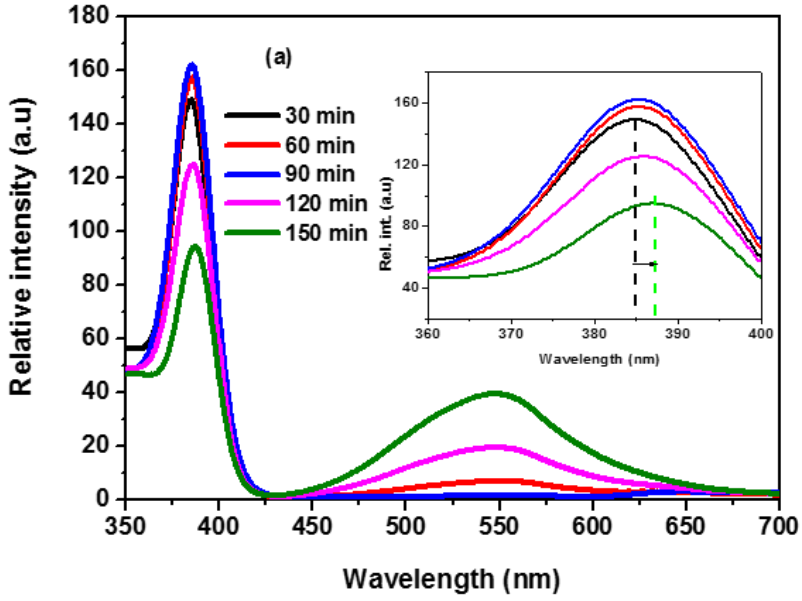

Figure 9.4: (a) Room-temperature PL spectra and Inset: enlarged excitonic peak emission spectra for ZNRs grown at various deposition times.

From the PL spectra, Fig. 9.4(a) inset, it could be noted that the excitonic peak emission of the ZNRs shifts towards higher wavelengths (385 - 387 nm) with the increase in deposition growth time (30 - 150 min). The observed redshift could be due to an increase in the particle size as explained by Ostwald ripening process [40, 50] where the larger particles grow at the expense of the smaller ones.

The Commission International de I'Eclairage (CIE) chromaticity image of the as-prepared ZNRs was drawn and presented in Fig. 9.4(c). The x, y coordinates of the CIE is used to describe the emission color of the ZNRs prepared in this study. The CIE diagram confirms the findings from the PL which indicate a red shift in emission when the deposition growth time progressed from 30-90 min.

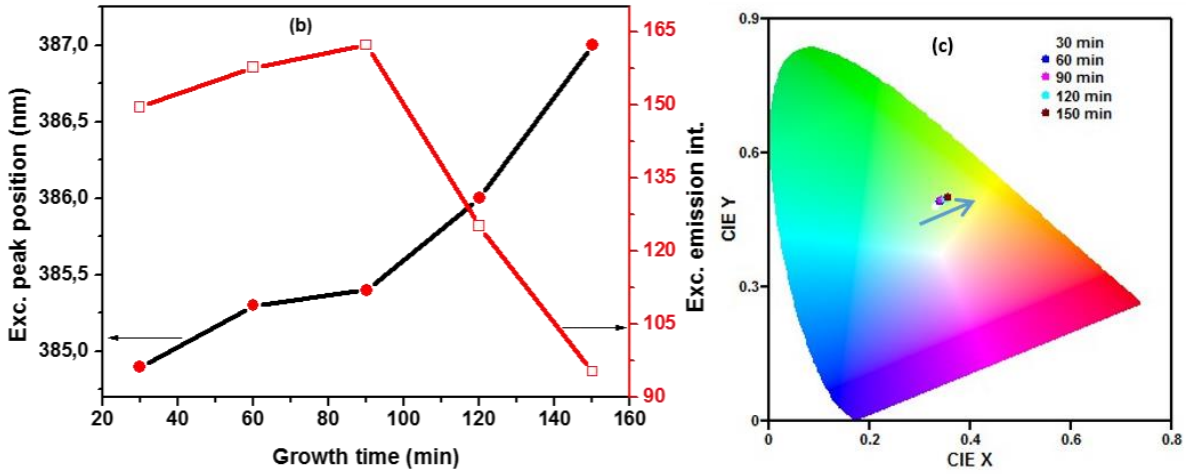

Figure 9.4: (b) Variation in the excitonic peak position and peak intensities with and (c) CIE image displaying colour changes with deposition growth time.

9.3.5 Optical properties

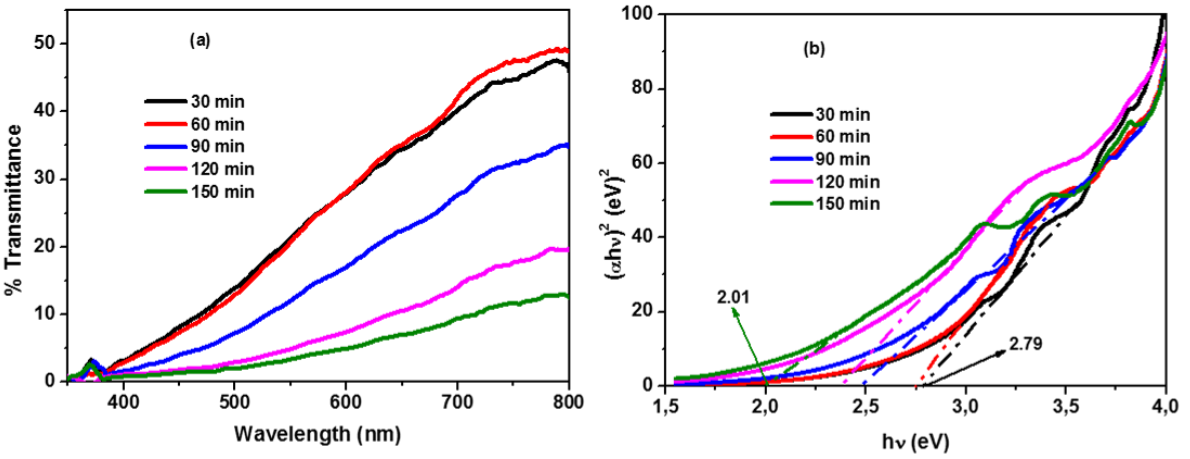

Figure 9.5: (a) UV–Vis % transmittance spectra and (b) Band gap energy plot of ZNRs at different deposition growth times.

The fraction of an incident light of a specific wavelength which passes through a sample is what is referred to as transmittance. The transmittance spectra of ZnO thin film grown at different deposition growth times were depicted in Fig. 9.5(a). The spectra displayed a high transparency in the wavelength range 500 - 800 nm for all the prepared samples. The ZnO transparency property in the visible region is thought to be due to the possession of wide band gap energy [51]. The variation of transmittance with deposition growth time was observed. It was noted that the films revealed a decline in transmittance at a prolonged duration of deposition. High transmittance displayed at a shorter duration of growth could be attributed to a thin layer of the film formed. As the growth progressed to longer

deposition time, the film became dense as larger and longer NRs were formed and hence reducing the percentage transmittance (% T). Furthermore, a red shift in absorption edges was observed as deposition growth time increased from 30 - 150 min as depicted in Fig. 9.5 (a). The shift to a longer wavelength at a prolonged duration of growth could be due to increase in the size of the grains formed.

The absorption coefficient (α) is calculated from % T data using the Beer-Lambert law eq. (9.3):

$$\alpha = \frac{1}{d}\ln\left[\frac{1}{T}\right] \tag{9.3}$$

Where d is the thickness of the films. The α and the incident photon energy ($h\nu$) is related by the Tauc's formula. For the direct allowed transitions occurring in the direct band gap of ZnO, near the band edge, α approximates to eq. (9.4).

$$\alpha h\nu = A\sqrt{h\nu - Eg} \tag{9.4}$$

where A is a constant and Eg is the band gap energy of the material. The nature of the band gap transition is said to be direct as could be explained by the linear nature of the plot. In order to determine the band gap, the linear portion of the graph was extrapolated to the energy axis at $h\nu = 0$. The band gap energy values were estimated and found to decrease with increase in deposition growth time from 2.79 to 2.01 eV for the ZNRs thin films. This phenomenon can be explained to be caused by the increase in the size of the crystallites/grain sizes and alteration of grain borderline arrangements during growth as confirmed by XRD results. The values of band gap energies obtained in this study were in close agreement with the values reported in ref [52]. Variation in the values of band gap energy of the ZNRs thin films with deposition growth time offers an easy way to engineer both the structural and optical properties to suit a specific application.

Conclusions

ZNRs thin films were successfully synthesized on GZO seeded glass substrate by the two-step CBD method at different growth deposition times while keeping growth temperature and precursor concentrations constant. XRD analysis displayed a wurtzite structure with a preferred [002] plane orientation with the NRs growing along the c-axis. Increase in crystallite sizes calculated from the Scherrer's formula with an increase in deposition growth time was observed. SEM and AFM images showed a variation of surface morphologies with deposition growth time with well aligned NRs obtained at 90 min of

growth time. The optical analysis displayed a red shift in the PL emission and absorption edges with an increase in deposition growth time. The PL excitonic peak intensity was found to increase to a maximum at 90 min and decreases thereafter for a longer duration of growth due to increase in defects in the samples. The ZNRs sample obtained at 90 min was confirmed, by the analysis techniques, to possess the best structural and optical properties hence the recommended deposition growth time for the preparation of the nanorods by CBD method on GZO seeded glass substrate.

References

[1] S. Iijima, Nature 354, (1991) 56-58.

[2] M. H. Huang, S. Mao, H. Feick, H. Yan, Y. Wu, H. Kind, E. Weber, R. Russo, P. Yang. Science 292, (2001) 1897-1899.

[3] J. Y. Li, X. L. Chen, H. Li, M. He, Z. Y. Qiao, Journal of crystal growth 233, (2001) 5-7.

[4] Z. W. Pan, Z. R. Dai, Z.L. Wang, Science 291, (2001) 1947-1949.

[5] J. Wu, S. Liu, C. Wu, K. Chen, L. Chen, Applied Physics Letters 81, (2002) 1312-1314.

[6] J. X. Wang, X. W. Sun, Y. Yang, H. Huang, Y. C. Lee, O. K. Tan, L. Vayssieres, Nanotechnology 17, (2006) 4995–4998.

[7] A. Wei, X. W. Sun, J.X. Wang, Y. Lei, X. P. Cai, C. M. Li, Z. L. Dong, W. Huang, Appl. Phys. Lett. 89, (2006) 123902.

[8] J. Lee, K. Park, M. Kang, I. Park, S. W. Kim, W.K. Cho, H. S. Han, S. Kim, Journal of Crystal Growth 254, (2003) 423-431.

[9] Q. X. Zhao, P. Klason, M. Willander., Applied Physics A: Materials Science & Processing 88, (2007) 27-30.

[10] M. H. Huang, Y. Wu, H. Feick, N. Tran, E. Weber, P. Yang, Advanced Materials 13, (2001) 113-116.

[11] Y. Sun, G. M. Fuge, M. N. R. Ashfold, Chemical Physics Letters 396, (2004) 21-26.

[12] J. Wu, S. Liu, Advanced materials 14, (2002) 215.

[13] W. Park, D. Hl Kim, S.W. Jung, G.C. Yi, Applied Physics Letters 80, (2002) 4232-4234.

[14] H. Yu, Z. Zhang, M. Han, X. Hao, F. Zhu, Journal of the American Chemical Society 127, (2005) 2378-2379.

[15] L. Vayssieres, K. Keis, S.E. Lindquist, A. Hagfeldt, Journal of Physical Chemistry B 105, (2001) 3350-3352.

[16] D. Vernardou, G. Kenanakis, S. Couris, E. Koudoumas, E. Kymakis, N. Katsarakis, Thin Solid Films 515, (2007) 8764-8767

[17] H. Zhang, D. Yang, S. Li, X. Ma, Y. Ji, J. Xu, D. Que, Materials Letters 59, (2005) 1696-1700.

[18] Z. Zhaochun, H. Baibiao, Y. Yongqin, C. Deliang, Materials Science and Engineering: B 86, (2001) 109-112.

[19] K. Govender, D. S. Boyle, P. B. Kenway, P. O'Brien, Journal of Materials Chemistry 14 (16), (2004) 2575-2591

[20] Y. Tong, L. Dong, Y. Liu, D. Zhao, J. Zhang, Y. Lu, D. Shen, X. Fan, Mater. Lett. 61, (2007) 3578.

[21] L. Vayssieres, Advanced Materials 15, (2003) 464-466.

[22] R. B. Peterson, C. L. Fields, B. A. Gregg, Langmuir 20, (2004) 5114-5118.

[23] L. L. Yang, Synthesis and Characterization of ZnO Nanostructures. Linköping University, Norrköping, 2010.

[24] S. F. Wang, T. Y. Tseng, Y. R. Wang, C. Y. Wang, H. C. Lu, Ceramics International 35(3), (2009) 1255-1260.

[25] J. B. Cui, C.P. Daghlian, U. J. Gibson, R. Pusche, P. Geithner, L. Ley, J. Appl. Phys. 97, (2005) 044315.

[26] Y. Tak, K. Yong, Journal of physical chemistry B 109, (2005) 19263-19269.

[27] C. H. Hung, W. T. Whang, Journal of crystal growth 268, (2004) 242-248

[28] X. Feng, L. Feng, M. Jin, J. Zhai, L. Jiang, D. Zhu, Journal of the American Chemical Society 126, (2004) 62-63.

[29] J. Ungula, B. F. Dejene, H.C. Swart, Journal of Luminescence 195 (2018) 54–60.

[30] J. Ungula, B. F. Dejene, H. C. Swart, Physica B: Condensed Matter (2017), ISSN: 0921-4526 (In press).

[31] G. C. Yi, C. Wang, W. Park, Semiconductor Science and Technology 20, (2005) S22.

[32] International Center for Diffraction Data, 2011. File 00-001-1136.

[33] D. I. Rusu, G. G. Rusu, D. Luca, Acta Physica Polonica A 6, (2011) 119.

[34] W. Y. Wu, C.C. Yeh, J. M. Ting, Journal of the American Ceramic Society 92, (2009) 2718-2723.

[35] J. Yang, J. Lang, L. Yang, Y. Zhang, D. Wang, H. Fan, H. Liu, Y. Wang, M. Gao, Journal of Alloys and Compounds 450, (2008) 521-524.

[36] B. D. Cullity, S. R. Stock, pp. 388-90 in Chapter 14-3 Crystallite Size, Prentice- Hall Inc, Englewood Cliffs, NJ, 2001.

[37] V. Kumari, V. Kumar, B.P. Malik, R.M. Mehra, D. Mohan, Optics Communications 285, (2012) 2182-2188.

[38] S. Lalitha, R. Sathyamoorthy, S. Senthilarasu, A. Subbarayan, K. Natarajan, Sol. Energy Mater. Sol. Cells 82, (2004) 187-199.

[39] A. Purohit, S. Chander, S.P. Nehra, M.S. Dhaka, Physica E 69, (2015) 342-348.

[40] S. Kiprotich, M.O. Onani, F.B. Dejene, Physica B: Condensed Matter 535, (2018), 202-210.

[41] J. Zhao, J. G. Jin, T. Li, X. X. Liu, J. Eur. Ceram. Soc. 26, (2006) 3745–3752.

[42] J. Yang, J. Lang, L. Yang, Y. Zhang, D. Wang, H. Fan, M. Gao, Journal of Alloys and Compounds 450, (2008) 521-524.

[43] V. Kumar, H.C. Swart, S. Som, Vijay Kumar, A. Yousif, A. Pandey, S.K.K. Shaat, O.M. Ntwaeaborwa, Laser Phys. 24, (2014) 105704-105714.

[44] E. Hasabeldaim, O. M. Ntwaeaborwa, R. E. Kroon, E. Coetsee, H. C. Swart, Optical Materials (2017), ISSN 0921-4526 (In press).

[45] V. Srikant, D. R. Clarke, Journal of Applied Physics 83, (1998) 5447-5451.

[46] T. M. Børseth, B. G. Svensson, A. Y. Kuznetsov, P. Klason, Q.X. Zhao, M. Willander, Applied Physics Letters 89, (2006) 262112.

[47] C. H. Tsai, W. C. Wang, F. L. Jenq, C. C. Liu, C. I. Hung, M. P. Houng, Journal of applied physics 104, (2008) 053521.

[48] Z. Lei, J. Lian, Y. Liu, Q. Jiang, Transactions of Nonferrous Metals Society of China 18, (2008) 145-149.

[49] J. Ungula, B. F. Dejene, Physica B: Condensed Matter 480, (2016) 26-30.

[50] F. Jiang, A.J. Muscat, Langmuir 28, (2012) 12931-12940.

[51] S. S. Lin, J. L. Huang, Surface and Coatings Technology 185, (2004) 222-227.

[52] A. E. Ajuba, S. C. Ezugwu, B. A. Ezekoye, F. I. Ezema, P. U. Asogwa, Journal of Optoelectronics and Biomedical Materials 2, (2010) 73-78.

Chapter 10

Thesis summary and suggestions for the future work

10.1 Summary

In this thesis, the growth and characterization of un-doped, Ga/or Al-doped ZnO NPs and ZNRs using cost-effective, simple and environmentally friendly synthesis techniques were discussed. The NPs were synthesized using the reflux-precipitation method while the ZNRs were successfully grown on glass substrates pre-seeded with a film of GZO NPs using a two-step CBD technique.

The GZO NPs prepared at Ga/Zn sol. pH of 5, 2 mol% Ga-doping and annealed at 300 ℃ were found to have superior structural, luminescence and optical properties compared to their counterparts. The properties which include: high crystallinity, moderately small crystallite size, minimum lattice stress, lowest % reflectance and strongest PL UV-emission, relatively larger I_{UV}/I_{DLE} PL ratio, adequately enhanced band gap, were deemed suitable and thus useful to make the GZO seed layer film upon which ZnO NRs were grown. On the other hand, the growth concentration of 0.05 M and deposition time of 90 min. were found to provide an optimum structural and optical properties required to fabricate ZnO NRs with fairly good material properties.

The combination of the optimized ZNRs semiconductor and GZO films would provide a promising photoelectrode for the DSSCs application where the improvement of conductivity and the decrease of resistivity is the main issue. Because while the former provide larger surface areas required to provide anchoring sites for dye and therefore direct conduction pathway for charge transfer from the position of electron-hole pair generation to the collecting electrode, the later act as the transparent conducting film.

10.2 Future work

In line with the outcome of the present study, firstly, there is a need to achieve the best energy conversion efficiency of the DSSCs made from the as-fabricated GZO/ZnO NRs photoelectrode by further optimizations of its properties. These include, decreasing the diameter; enhancing density of the array, crystallinity and optical quality of ZNRs as well as increasing their aspect ratio and enhancing the morphology and electrical properties through careful control and optimization of the parameters which affect the device performance. It is also important to study the electrical parameters such as sheet resistance, electrical resistivity and the figure of merit of the photoelectrode. Likewise, there is a need to investigate the electron transport properties using suitable methods like electrochemical impedance spectroscopy (EIS) and measure the photocurrent density–voltage (J–V) curves using appropriate tools like the Keithley 2611 digital source meter. The next phase comprises device assembly of DSSCs, where different components of the cells are integrated. This involves sensitization of the hybrid structure of ZnO NRs /GZO with light-harvesting dye molecules, fabrication of the photo electrochemical cells using electrolytes and fabrication of the counter electrode starting from a glass covered with a film of GZO or any other conductive oxide. Finally, the plan is to conduct the device evaluation and explore the GZO/ZNRs films hybrid structure for solar cell applications. The photovoltaic performance of the DSSCs is determined by evaluating parameters such as open circuit photovoltage, short circuit photocurrent, fill factor, and energy conversion efficiency.

10.3 Publications

Publications by the authors **J. Ungula**, B. F. Dejene and H. C. Swart

1. **J. Ungula,** B.F. Dejene, H.C. Swart, "Band gap engineering and enhanced morphology and photoluminescence of un-doped, Ga and/or Al-doped ZnO nanoparticles by reflux precipitation method", in Journal of Luminescence 195, (2018) 54–60, ISSN 0022-2313, https://doi.org/10.1016/j.jlumin.2017.11.007.
2. **J. Ungula**, B.F. Dejene, H.C. Swart, "Effect of pH on the structural, optical and morphological properties of Ga-doped ZnO nanoparticles by reflux precipitation method," In Physica B: Condensed Matter 535, (2018) 251-257, ISSN 0921-4526, https://doi.org/10.1016/j.physb.2017.07.052.
3. **J. Ungula**, B.F. Dejene, H.C. Swart, "Effect of annealing on the structural, morphological and optical properties of Ga-doped ZnO nanoparticles by reflux

precipitation method," In Results in Physics 7, (2017) 2022-2027, ISSN 2211-3797, https://doi.org/10.1016/j.rinp.2017.06.019.

4. **J. Ungula,** B.F. Dejene, H.C. Swart, "Effects of different Ga doping concentration on structural and optical properties of Ga–doped ZnO nanoparticles by precipitation reflux method," in the Proceedings of the SAIP2016, the 61st Annual Conference of the South African Institute of Physics, edited by Dr. Steve Peterson and Dr. Sahal Yacoob (UCT/2016), pp. 82 - 87. ISBN: 978-0-620-77094-1. Available online at http://events.saip.org.za
5. **J. Ungula,** B.F. Dejene, H.C. Swart, "Structural, morphological and optical properties of ZnO nanorods grown on Ga-doped ZnO seeded thin film layer from aqueous solution: The role of CBD precursor concentration," (**Ready for submission).**
6. **J. Ungula,** B.F. Dejene, H.C. Swart, "Study on the role of deposition growth time on structural and optical properties of ZnO nanorods grown on GZO seeded thin film layer from aqueous solution," (**Ready for submission**).
7. **Ungula, J.,** and B. F. Dejene. "Effect of solvent medium on the structural, morphological and optical properties of ZnO nanoparticles synthesized by the sol–gel method." Physica B: Condensed Matter 480, (2016) 26-30, http://www.elsevier.com/locate/physb
8. Kiprotich, S., Dejene, F. B., **Ungula, J**., & Onani, M. O. (2016). The influence of reaction times on structural, optical and luminescence properties of cadmium telluride nanoparticles prepared by wet-chemical process. Physica B: Condensed Matter 480, (2016) 125-130, http://www.elsevier.com/locate/physb
9. **Ungula, J.,** and B. F. Dejene, "Effect of annealing on un-doped and Ce, Dy, Eu, Ni-doped ZnO properties synthesized by sol-gel method," in the Proceedings of the SAIP2013, the 58th Annual Conference of the South African Institute of Physics, edited by Dr. Roef Botha and Dr. Thuli Jili, hosted by University of Zululand-Richards Bay Campus, pp. 187 - 189. ISBN: 978-0-620-62819-8, Available online at http://www.saip.org.za

10.4 Presentations at conferences

- **The 58th Annual Conference of South African Institute of Physics (SAIP 2013),** University of Zululand-Richards Bay Campus, (RSA) 8th-12th July 2013 (Presentation on: Effect of annealing on un-doped and Ce, Dy, Eu, Ni-doped ZnO properties synthesized by sol-gel method).
- **The 59th Annual Conference of South African Institute of Physics (SAIP 2014),** University of Johannesburg (RSA) 7th-11th July 2014, Effect of growth temperature on structural and luminescence properties of ZnO nanoparticles by Sol-Gel method,
- **The 60th Annual Conference of the SA Institute of Physics (SAIP 2015), NMMU, South Africa** (Presentation on: Comparison of optical and luminescence properties of as prepared and annealed ZnO nanoparticles).
- **The 61st Annual Conference of the SA Institute of Physics (SAIP 2016),** University of the Cape Town, (Presentation on: Effects of different Ga doping concentration on structural and optical properties of Ga–doped ZnO nanoparticles by precipitation reflux method).
- **The 5th South African Conference on Photonic Materials (SACPM 2013),** Kariega Game Reserve, (RSA) 29th Apr.- 3rd May 2013, Comparison of ZnO nanoparticles properties synthesized at room temperature using water and ethanol as solvents.
- **The 6th South African Conference on Photonic Materials (SACPM 2015), May 2015,** Mabula Game Reserve, South Africa (Presentation on: Effect of solvent medium on the structural, morphological and optical properties of ZnO nanoparticles synthesized by sol-gel method).
- **The 7th South African Conference on Photonic Materials (SACPM 2017),** Amanzi Game Reserve (Presentation on**:** Effect of pH on the structural, optical and morphological properties of Ga-doped ZnO nanoparticles by reflux precipitation method).